Evolution of the One-Quadrupole Phonon $2^+_{1,\mathrm{ms}}$ Mixed-Symmetry State in ^{124,126,128,130,132}Xe

Zur Erlangung des Grades eines Doktors der Naturwissenschaften (Dr. rer. nat.)
genehmigte Dissertation von Dipl.-Phys. Laurent Coquard aus Saint-Germain en Laye (Frankreich)
Juni 2010 — Darmstadt — D 17

TECHNISCHE
UNIVERSITÄT
DARMSTADT

Fachbereich Physik
Institut für Kernphysik
Schlossgartenstr. 9
D-64289 Darmstadt

Evolution of the One-Quadrupole Phonon $2^+_{1,\mathrm{ms}}$ Mixed-Symmetry State in ^{124,126,128,130,132}Xe

Genehmigte Dissertation von Dipl.-Phys. Laurent Coquard aus Saint-Germain en Laye (Frankreich)

1. Gutachten: Prof. Dr. N. Pietralla
2. Gutachten: Prof. Dr. T. Kröll

Tag der Einreichung: 09. April 2010
Tag der Prüfung: 10. Mai 2010

Darmstadt — D 17

Erklärung zur Dissertation

Hiermit versichere ich die vorliegende Dissertation ohne Hilfe Dritter nur mit den angegebenen Quellen und Hilfsmitteln angefertigt zu haben. Alle Stellen, die aus Quellen entnommen wurden, sind als solche kenntlich gemacht. Diese Arbeit hat in gleicher oder ähnlicher Form noch keiner Prüfungsbehörde vorgelegen.

Darmstadt, den 24th June 2010

(L. Coquard)

“If the life is complex it is because there is a real part and an imaginary part.”
(Géraud Devos)

Abstract

Collective nuclei are characterized by rotational and vibrational states due to a common and therefore “collective” behavior of the two constituents of the nucleus: protons and neutrons. The evolution of the collectivity (spontaneous deformation) is governed by the proton-neutron interaction in the valence shell. Nuclear states that are particularly sensitive to the proton-neutron interaction in the valence shell are the so called mixed symmetry states (MSSs). In this work we trace the evolution of the fundamental MSS, *i.e* the one-quadrupole phonon $2^+_{1,\mathrm{ms}}$ state, in a transitional region from vibrational nuclei (^{134}Xe) to γ-soft nuclei reflecting the O(6)-like structure of the IBM-2 (^{124,126}Xe). Projectile-Coulomb excitation of Xe isotopes has been performed at Argonne National Laboratory (ANL) using the Gammasphere array for the detection of γ-rays.

First, our data on more than 50 absolute $E2$ transition rates between off-yrast low-spin states of ^{124,126}Xe enable us to quantitatively test O(6) symmetry in these two nuclei. As a result we find that O(6) symmetry is more strongly broken in the $A = 130$ mass region than previously thought. Then, 19 absolute $E2$ transition strengths have been obtained in ^{128}Xe including the first measurement of the critical $B(E2)$ decays from the second and third $J^\pi = 0^+$ states. These data are compared with the theoretical predictions of the critical point symmetry E(5) and let us conclude that ^{128}Xe is not an E(5) nucleus as previously suggested, leaving ^{130}Xe as the most likely candidate amongst the xenon isotopes. Finally, the one-phonon $2^+_{1,\mathrm{ms}}$ states or at least a fragment of it have been identified in ^{128,130,132,134}Xe. This enables us to trace the evolution of the one-phonon $2^+_{1,\mathrm{ms}}$ states in the even-even stable xenon isotopic chain from the vibrators near $N = 82$ to the γ-soft nuclei towards mid-shell.

Zusammenfassung

Kollektive Kerne können durch Rotations- oder Vibrationsanregungen beschrieben werden, die von dem gemeinsamen Verhalten der zwei Bestandteile des Kerns, den Protonen und Neutronen, entstehen. Die Entwicklung der Kollektivität, etwa spontane Kerndeformation, wird durch die Proton-Neutron–Wechselwirkung im Valenzraum beeinflusst. Sogenannte gemischt-symmetrische Zustände sind besonders sensitiv auf die pn–Wechselwirkung im Valenzraum. Diese Arbeit untersucht die Entwicklung des pn-gemischt-symmetrischen $2^+_{1,\mathrm{ms}}$ Ein-Quadrupol-Phononzustands im Übergang von Vibratorstruktur (^{134}Xe) zur Struktur γ-weicher Kerne der O(6)-Symmetrie des Interacting Boson Model (IBM-2) (^{124,126}Xe). Die zu erforschenden Zustände sind mittels der Methode der Projektil-Coulomb-Anregung am amerikanischen Argonne National Labor (ANL) an Leichtionen-Targets bevölkert worden. Ihre γ-Zerfälle sind mit dem 4π-Halbleiter-Detektorfeld *Gammasphere* nachgewiesen.
Die experimentellen Daten mit mehr als 50 absoluten $E2$ Übergangsraten zwischen off-yrast tief liegenden Zustände in ^{124,126}Xe erlaubten es die O(6) Symmetrie in diesen zwei Kernen quantitativ zu untersuchen. Darüber hinaus liess sich festellen, dass die O(6) Symmetrie in der $A = 130$ Mass Region stärker gebrochen ist als es bisher bekannt war. Die 19 gemessenen absoluten $E2$ Übergangsraten in ^{128}Xe inklusive der ersten Messungen von den kritischen $B(E2)$ Zerfällen von dem zweiten und dritten $J^\pi = 0^+$ Zustand, ermöglicht die Schlussfolgerung, dass der Kern ^{128}Xe nicht an dem kritischen Punkt E(5) liegt. ^{130}Xe wird stattdessen als bester Kandidat unter den Xe Isotopen vorgeschlagen. Zudem ist der $2^+_{1,\mathrm{ms}}$ Ein-Quadrupol-Phononzustand oder ein Fragment davon in ^{128,130,132,134}Xe identifiziert worden. Dementsprechend konnten wir für zum ersten Mal die Entwicklung eines pn-gemischt-symmetrischen $2^+_{1,\mathrm{ms}}$ Ein-Quadrupol-Phononzustands beim Übergang von Vibratorstruktur zur Struktur γ-weicher Kernen der O(6)-Symmetrie verfolgen.

Contents

1 Introduction

What is nuclear physics?

Nuclear physics is the field of physics that studies the building blocks and interactions of atomic nuclei. This branch of science was born after the discovery of the atomic nucleus by Rutherford in 1911 and investigations from the properties of the nucleus have continued from Rutherford's time to the present day. In order to understand the properties of the nucleus, among which are mass, radius, decay modes, half-lives, reaction modes, cross sections, spin, magnetic dipole and electric quadrupole moments, excited states, transitions strengths..., experimental as well as theoretical studies have been carried out for almost one century and we understand an enormous amount. We have models: the shell model and collective models that provide a framework for our understanding. We have databases where experimental results are repertoried such as the Evaluated Nuclear Structure Data File in National Nuclear Data Center (NNDC) in Brookhaven, USA.

In the shell model one fills the shells with nucleons in order of increasing energy, consistent with the requirement of the Pauli principle, analogous to the filling of electron shells in atoms. Note that the shells exist for both protons and neutrons individually. The nucleus consists of an inert filled core of closed shells and some number of valence nucleons. Excited states were found that correspond to the excitation of a nucleon into an orbit of a higher lying shell. Such excitations are called single-particle excitations and usually lie above 1 MeV. However there exists other types of excitations which involve more than one single particle. Such excitations are called collective excitations and can be interpreted in the framework of collective models. Collective excitations can be vibrations or rotations of the nucleus and they are usually lying at lower energies (< 2 MeV).

What is the purpose of this work?

The evolution of nuclear collectivity depends critically on the proton-neutron interaction in the valence shell. This fact is obvious from the evolution of collective variables such as the $E2$ excitation strength of the 2_1^+ state of even-even nuclei with the product of valence nucleon numbers N_pN_n [1]. Despite its crucial role, measurements of the size of the proton-neutron interaction in the valence shell are scarce. This is the general purpose of this work to study the evolution of collectivity governed by the proton-neutron quadrupole interaction in the valence shell of even-even stable Xe isotopes.

Which observable is sensitive to the proton-neutron interaction in the valence shell?

Atomic nuclei are examples of mesoscopic two-fluid quantum systems. The physics of such systems is determined by three main properties: the many-body aspect, the quantum nature, and the two-fluid character. Nuclear phenomena that reflect these three properties are the collectivity, the shell structure and the isospin degree of freedom. Of particular importance for studying the mutual balance of these aspects are those excitations that are related to the collective two-fluid character of the nuclei and to their shell structure. Quadrupole-collective isovector valence-shell excitations, so-called Mixed-Symmetry States (MSSs), are the best studied examples of this class of phenomena. Proton-neutron MSSs are important sources of information on the effective proton-neutron interaction in collective nuclei. Their excitation energies are directly related to the proton-neutron interaction in the nuclear valence shell. This new class of collective states with mixed-symmetry character emerge in a natural way in the framework of the Interacting Boson Model-2 (IBM-2) [2]. Such states can be thought of as states in which the protons and neutrons oscillate out of phase with respect to one another. The fundamental MSS in collective two-fluid quantum systems is the one-quadrupole phonon $2^+_{1,\mathrm{ms}}$ state [2]. Despite its fundamental role in nuclear structure, the $2^+_{1,\mathrm{ms}}$ state has only recently been studied systematically, *e.g*, [3, 4, 5, 6, 7, 8]. The dominant fragments of the one-phonon $2^+_{1,\mathrm{ms}}$ state are observed at about 2 MeV excitation energy. Due to their isovector character, MSSs decay rapidly by dipole transitions and are very short lived, typically a few tens of femtoseconds. Large $M1$ matrix elements of $\approx 1\ \mu_N$ are in fact the unique safe signatures for mixed-symmetry character. A review article on the status of experimental information on MSS in vibrational nuclei has been published [9]. In deformed nuclei, the MSSs (or so-called scissors mode) have been exhaustively discussed and reviewed already [10, 11, 12]. The one-quadrupole phonon $2^+_{1,\mathrm{ms}}$ state which is sensitive to the proton-neutron interaction in the valence shell is thus the appealing object to look for in this quest through the Xe isotopes.

Why Xenon?

The Interacting Boson Model enables one to classify the nuclei according to the dynamical symmetries of the IBM Hamiltonian. Three symmetries are most relevant for the description of excited states of quadrupole-collective nuclei: U(5) for vibrational nuclei [13], SU(3) for axially deformed nuclei [14], and O(6) for deformed nuclei with soft triaxiallity [15]. In the $A = 130$ mass region, the xenon isotopes can exhibit excitation spectra close to the O(6) symmetry. After some theoretical investigations [16, 17, 18, 19, 20], it was concluded that the xenon isotopes should lie in a transitional region from U(5)- to an O(6)-like structure as the neutron number decreases from the closed shell $N = 82$. This was later supported by Casten and von Brentano [21] who presented evidence for an extensive region of nuclei near $A = 130$ resembling the O(6) symmetry. The evolution of the one-quadrupole phonon $2^+_{1,\mathrm{ms}}$ with F-spin value $F = F_{max} - 1$ in a U(5)-O(6) transition is still unknown. Thus Xe was a good candidate to explore this U(5)-O(6) transitional region.

Chapter 2 gives a short overview of the nuclear deformations with the two nuclear collective excitation modes: rotations and vibrations. Chapter 3 presents the general formalism of the Interacting Boson Model (IBM-1) followed by its proton-neutron version (IBM-2) and finally leading to the definition and characteristics of the MSSs. Chapter 4 deals with a theoretical model describing quite well a part of the U(5)-O(6) transitional region. Chapter 5 is devoted to the formalism of our experimental method: Coulomb excitation. Details about the experimental set up as well as the data analysis are given in Chapter 6. Finally the results are discussed in Chapter 7.

2 Nuclear Deformations

2.1 General nuclear deformation

The most simplified model of the description of the nucleus would consider that the distribution of nucleons is homogeneous and has no preferred direction in space. The nucleus is then spherical. However, in order to minimize its potential energy, the shape of the nucleus can deviate from its spherical shape and find a “new” equilibrium with a deformed shape. For the magic numbers (8, 20, 28, 50, 82, 126), the shape of a nucleus is in general spherical. Between these numbers most nuclei are deformed. The electrical potential V created by the distribution of charges in the nucleus at a distance R from the origin O (observer) can be expanded in multipoles

$$V(R) \propto \frac{1}{R}\int \rho(r)dr + \frac{1}{R^2}\int z\rho(r)dr + \frac{1}{R^3}\int (3z^2 - r^2)\rho(r)dr + ... \tag{2.1}$$

where r denotes the distance from one point in the nucleus to the origin of the axis O and $\rho(r)$ is the charge density. The first term corresponds to the total charge of the nucleus. The second and third terms are the dipole and quadrupole terms respectively. Most of the nuclei are ellipsoidal and therefore have an axial symmetry. In this case the dipole term is zero which leaves the deformed nucleus as a quadrupole distortion only. There can also be octupole and hexadecapole shapes. The shape of the nucleus can then be parametrized from a spherical shape corrected by the spherical harmonics $Y_{\lambda\mu}(\theta,\phi)$

$$R(\theta,\phi) = R_0\left[1 + \sum_{\lambda=0}\sum_{\mu=-\lambda}^{\lambda}\alpha_{\lambda\mu}Y_{\lambda\mu}(\theta,\phi)\right], \tag{2.2}$$

where R_0 is the radius of a sphere of the same volume. The term $\lambda = 0$ describe volume variations, $\lambda = 1$ the translation of the system. The term with $\lambda = 2$ corresponds to quadrupole deformation and $\lambda = 3$ to octupole deformation. Using the transformation from the laboratory frame to the intrinsic frame, the five $\alpha_{\lambda=2,\mu}$ parameters are reduced to three real parameters $\alpha_{2,0}$, $\alpha_{2,2} = \alpha_{2,-2}$ and $\alpha_{2,1} = \alpha_{2,-1} = 0$. These variables can be parametrized following the conventions of Hill and Wheeler [22]:

$$\alpha_{2,0} = \beta\cos\gamma, \tag{2.3}$$

$$\alpha_{2,2} = \alpha_{2,-2} = \frac{1}{\sqrt{2}}\beta\sin\gamma, \tag{2.4}$$

where β represents the extent of the quadrupole deformation, while γ gives the degree of axial asymmetry. Most nuclei are axially symmetric, or close to it, at least in their ground states. For an axially symmetric nucleus, the potential has a minimum at $\gamma = 0°$. A common convention (Lund convention) for the ranges of the β and γ variables is that $\beta > 0$, $\gamma = 0°$ for an axially symmetric prolate nucleus and that $\beta > 0$, $\gamma = 60°$ gives an axially symmetric oblate nucleus as it is shown in Fig. 2.1. Note that for $\beta < 0$, $\gamma = 0°$, the nucleus is oblate. If γ is not a multiple of 60°, one says that the nucleus is triaxial.

2.2 The vibrational model

Vibrations are one example of the collective behavior of the nucleons. In the vibrational model, the $\lambda = 2$ excitation (Eq. 2.2) is seen as a one phonon excitation (or quadrupole phonon) carrying two units of angular momentum (units $\hbar$). In even-even nuclei, adding a quadrupole phonon to the 0^+ ground state leads to the first excited 2^+_1 state. A two-phonon coupling results in three states with angular momenta: 0^+, 2^+, 4^+ while a three phonon excitation results in a quintuplet of states with angular momenta: 0^+, 2^+, 3^+, 4^+, 6^+. This is shown in Fig. 2.2. The pure harmonic vibrational model predicts that the two-phonon triplet states lies at twice the energy of the 2^+_1 state while the three-phonon quintuplet states at three times the energy of the 2^+_1 state. Consequently, one fingerprint of the vibrational model is the energy ratio $R_{4/2} = E(4^+_1)/E(2^+_1) = 2.0$. In realistic situations this ratio is typically 2-2.5. Such nuclei often called “vibrators” are situated near closed shells (or magic nuclei 8, 20, 28, 50, 82, 126). In the IBM-1 framework, they correspond to the U(5) dynamical symmetry (see section 3.2.4).

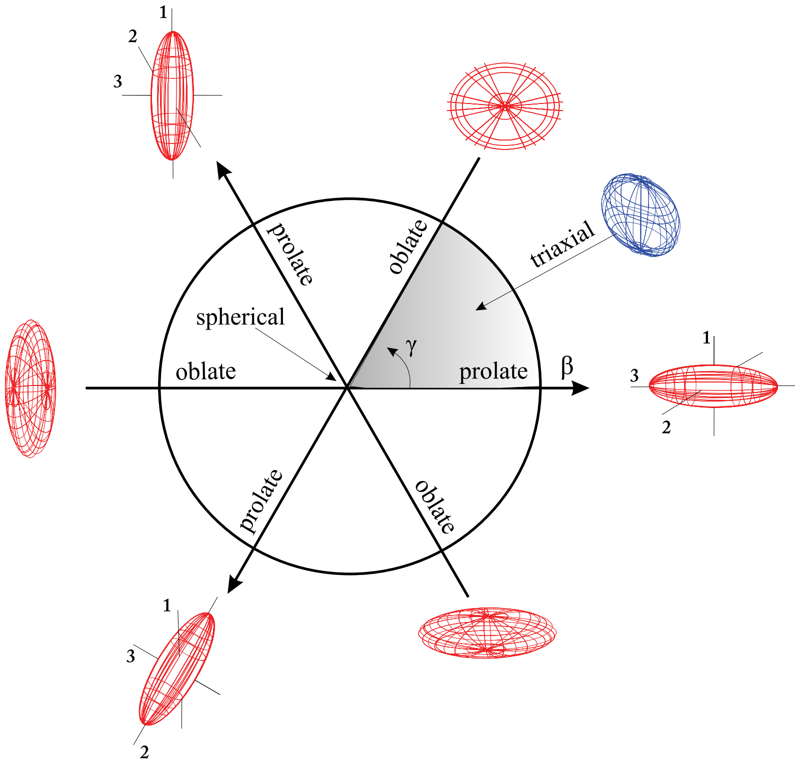

Figure 2.1: Nuclear deformation in the (β,γ) plane. The Lund conventions are used (see text). The four cases (γ=120°, 180°, 240°, 300°) correspond to the cases with γ=0° and 60° but with different orientations of their axis. The area 0°<γ<60° (in grey) is then sufficient to describe the nuclear deformation.

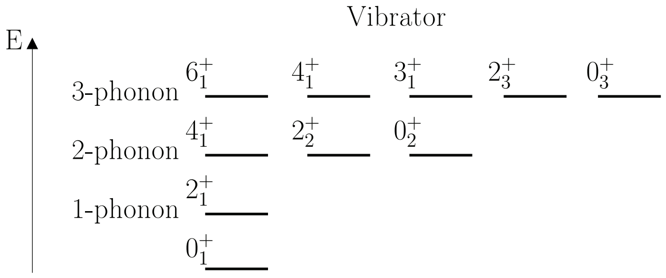

Figure 2.2: Low-lying levels in the pure harmonic vibrational model in even-even nuclei.

2.3 The rotational model

Another collective approach is to view the nucleus as an axially symmetric rigid rotating system along an axis perpendicular to the symmetry axis. Rotational motion can be observed only in nuclei with non spherical equilibrium shapes. These nuclei are often called *deformed* nuclei. The rotational energy of such a rotating system with total angular momentum $\overrightarrow{J}$ is given by

$$E_{rot}(J) = \frac{\hbar^2}{2I} J(J+1) \tag{2.5}$$

where I is the moment of inertia (here for a rigid object) and only even J are allowed in the ground state band. Increasing the quantum number J corresponds to adding rotational energy to the nucleus, and the nuclear states form a sequence known as a *rotational band*. Considering the low-lying excitation spectrum in even-even nuclei, the low lying rotational energy levels are labeled by J^π=0^+, 2^+, 4^+, 6^+,... and E(2_1^+)=$6\hbar^2/2I$, E(4_1^+)=$20\hbar^2/2I$,... . The structure of a rotational band is shown in Fig. 2.3. An important result here is the signature for rotational behavior with $R_{4/2} = E(4_1^+)/E(2_1^+) = 3.33$. Such nuclei are often called “rotors” and they are found in the mass ranges $150 < A < 190$ and

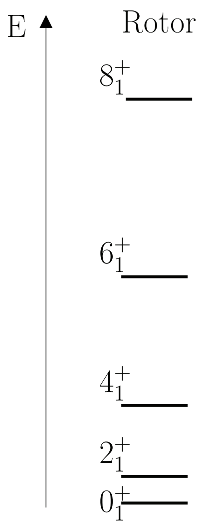

Figure 2.3: Low-lying levels in the rotational model in even-even nuclei.

$A > 220$ (rare earths and actinides). In the IBM-1 framework, they correspond to the SU(3) dynamical symmetry (see section 3.2.4).

3 The Interacting Boson Model (IBM)

Up until the mid-1970s, the two principal touchstones of the nuclear theory were the shell model and the geometrical model [23, 24] (sometimes also labeled as collective model). In 1974, a new model based on a third approach, that is group theoretical or algebraic, was proposed: the Interacting Boson model (or Interacting Boson Approximation) developed by Arima and Iachello [15]. The IBM tries to bridge the gap between the shell model and the collective models by exploring the symmetries of the quadrupole interaction. The model finds its origin from early ideas of Elliot [25], Feshbach and Iachello [26, 27], and from the work of Janssen, Jolos and Dönau [28]. The model in its original form (IBM-1 or sd-IBM-1) is a model to describe the quadrupole-collective behavior of low-lying quadrupole-collective states with positive parity in medium and heavy even-even nuclei. This IBM-1 model does not distinguish between protons and neutrons. For the last 30 years, the original IBM-1 framework has been extended to different versions: the IBM-2 which distinguishes between protons and neutrons, the IBM-3 and IBM-4 which can describe light nuclei, the IBFM (Interacting Boson Fermion Model) for the description of odd nuclei, the “sdf-IBM” for the description of levels with negative parity, the “sdg-IBM” to provide satisfactory description of other nuclear properties etc. In this work we will refer only to the IBM-1 and IBM-2 versions of the model. These two versions of the model are explained in details in [29].
The IBM is a model based on very simple assumptions, following the formalism of quantum mechanics (Hamiltonian, operators, basis, states or wave functions, second quantization) and supported by an algebraic mathematical framework. It is preferable to have a solid background in mathematics (group theory) in order to survive through the comprehension of the model. The book from Bonatsos ([30]) gives a short but clear overview of the algebraic structure of the IBM. In the following we will present the assumptions of the model, then the formalism of the sd-IBM-1 will be described followed by its extended version, the sd-IBM-2 leading to the existence of the Mixed-Symmetry States (MSS).

3.1 Assumptions of the IBM

In the simplest form of the IBM (IBM-1), it is assumed that:

- low-lying collective states in medium and heavy even-even nuclei away from closed shells are dominated by the excitations of the valence protons and the valence neutrons only, while the closed-shell core stays inert.
- the identical valence nucleons are coupled into pairs of angular momenta $J = 0$ (s-boson) or $J = 2$ (d-boson).
- the number of bosons is always half the number of valence nucleons (or holes) counted from the nearest closed-shell.
- no distinction is made between protons and neutrons.

3.2 sd-IBM-1

3.2.1 Bosonization

The IBM is using the language of second quantization. The boson creation operators are given by $s^\dagger$ and $d^\dagger_\mu$ and annihilation operators by s and d_μ where $\mu = -2, -1, 0, 1, 2$ corresponds to the 5 magnetic substates of the d boson. The s-boson has only one magnetic substate ($m = 0$).

Denoting the bosons by $b_{l,m}$ where l denotes the angular momentum and m denotes the magnetic substate, the creation and annihilation operators fulfill the commutation relations for bosons

$$[b_{l,m}, b^\dagger_{l',m'}] = \delta_{ll'}\delta_{mm'}, \tag{3.1}$$

$$[b_{l,m}, b_{l',m'}] = [b^\dagger_{l,m}, b^\dagger_{l',m'}] = 0. \tag{3.2}$$

If the boson creation operators $b^\dagger_\mu$ are defined as to transform as spherical tensors under rotations, then the boson annihilation operators b_μ do not. Therefore, it is more convenient to introduce the operator $\tilde{b}_{l,m}$ defined as

$$\tilde{b}_{l,m} = (-1)^{l+m} b_{l,-m}, \tag{3.3}$$

that then transforms also as spherical tensors under rotations. Thus, in the sd-IBM-1 one uses the creation and annihilation operators

$$\begin{aligned} &s^\dagger, d^\dagger_\mu \quad (\mu = 0, \pm 1, \pm 2), \\ \tilde{s} = s, &\tilde{d}_\mu = (-1)^\mu d_{-\mu} \quad (\mu = 0, \pm 1, \pm 2), \end{aligned} \tag{3.4}$$

which span a six dimensional space. With tensor operators one can form tensor products:

$$T^{(l)}_m = [T^{(l_1)} \times T^{(l_2)}] = \sum_{m_1, m_2} (l_1 m_1 l_2 m_2 | l m) T^{(l_1)}_{m_1} T^{(l_2)}_{m_2}, \tag{3.5}$$

where $(l_1 m_1 l_2 m_2 | l m)$ are the well known Clebsch-Gordan coefficients. One can also define the scalar product between two tensor operators of equal rank l:

$$(T^{(l)} \cdot U^{(l)}) = (-1)^l \sqrt{2l+1} [T^{(l)} \times U^{(l)}]^0_0 = \sum_m (-1)^m T^{(l)}_m U^{(l)}_{-m}. \tag{3.6}$$

3.2.2 The Lie algebra U(6)

After having defined the boson operators and the tensor product, one introduces now the transformation generators

$$\begin{aligned} G^{(0)}_0(s,s) &= [s^\dagger \times \tilde{s}]^0_0 \\ G^{(0)}_0(d,d) &= [d^\dagger \times \tilde{d}]^0_0 \\ G^{(1)}_\mu(d,d) &= [d^\dagger \times \tilde{d}]^1_\mu \\ G^{(2)}_\mu(d,d) &= [d^\dagger \times \tilde{d}]^2_\mu \\ G^{(3)}_\mu(d,d) &= [d^\dagger \times \tilde{d}]^3_\mu \\ G^{(4)}_\mu(d,d) &= [d^\dagger \times \tilde{d}]^4_\mu \\ G^{(2)}_\mu(d,s) &= [d^\dagger \times \tilde{s}]^2_\mu \\ G^{(2)}_\mu(s,d) &= [s^\dagger \times \tilde{d}]^2_\mu. \end{aligned} \tag{3.7}$$

The commutation relations of these operators among themselves are the same as the commutation relation of the Lie algebra of the group U(6) of unitary transformations in 6 dimensions (hence U(6)). Definitions of group, algebra, Lie algebra, unitary group, orthogonal group are given in [30]. These operators G (in total $36 = 6^2$) are thus identified as the generators of the algebra U(6). Thus one says that the Hamiltonian has the group structure of U(6). We will see later that one can decompose this "parent" group U(6) into "smaller" imbricated subgroups. This imbrication of groups is not always unique and reflects the symmetry of the Hamiltonian.

3.2.3 Hamiltonian and basis states

Once the algebraic structure of the problem has been identified, one can write the most general Hamiltonian describing a nucleus and assuming that the low-lying states of the nucleus would be described by one or two-body terms (which means only two-boson or four-boson terms in the Hamiltonian). The Hamilton operator is given by

$$H = E_0 + \sum_{\alpha,\beta} \epsilon_{\alpha\beta} b^\dagger_\alpha b_\beta + \sum_{\alpha,\beta,\delta,\gamma} \frac{1}{2} u_{\alpha,\beta,\delta,\gamma} b^\dagger_\alpha b^\dagger_\beta b_\delta b_\gamma. \tag{3.8}$$

Since the Hamiltonian must be a scalar and hermitian operator, it can be limited to the following form:

$$\begin{aligned}
H \quad = \quad & E_0 + \epsilon_s (s^\dagger \cdot s) + \epsilon_d (d^\dagger \cdot \tilde{d}) \\
& + \sum_{L=0,2,4} \frac{1}{2}\sqrt{2L+1} c_L [[d^\dagger \times d^\dagger]^L \times [\tilde{d} \times \tilde{d}]^L]^0_0 \\
& + \frac{1}{\sqrt{2}} v_2 [[d^\dagger \times d^\dagger]^2 \times [\tilde{d} \times s]^2 + [d^\dagger \times s^\dagger]^2 \times [\tilde{d} \times \tilde{d}]^2]^0_0 \\
& + \frac{1}{2} v_0 [[d^\dagger \times d^\dagger]^0 \times [s \times s]^0 + [s^\dagger \times s^\dagger]^0 \times [\tilde{d} \times \tilde{d}]^0]^0_0 \\
& + u_2 [[d^\dagger \times s^\dagger]^2 \times [\tilde{d} \times s]^2]^0_0 + \frac{1}{2} u_0 [[s^\dagger \times s^\dagger]^0 \times [s \times s]^0]^0_0 .
\end{aligned} \tag{3.9}$$

This most general Hamiltonian of the sd-IBM-1 contains 10 parameters: E_0, ϵ_s, ϵ_d, c_0, c_2, c_4, v_0, v_2, u_0, u_2. A very useful way to express the Hamiltonian is to use the multipole expansion:

$$H = E_0^{'} + \epsilon n_d + a_0 P^\dagger \cdot P + a_1 L \cdot L + a_2 Q^{-\frac{\sqrt{7}}{2}} \cdot Q^{-\frac{\sqrt{7}}{2}} + a_3 T^{(3)} \cdot T^{(3)} + a_4 T^{(4)} \cdot T^{(4)}, \tag{3.10}$$

where $E_0^{'}$ is a quadratic function of N ($E_0^{'} = E_{00} + E_{01}N + E_{02}N^2$). The quantity $E_0^{'}$ is the same for all states with a fixed N (a given nucleus). It does not contribute to the calculation of excitation energies. The multipole operators from Eq. 3.10 are given by

$$n_d = d^\dagger \cdot \tilde{d} \tag{3.11}$$

$$P = \frac{1}{2}(s \cdot s - \tilde{d} \cdot \tilde{d}) \tag{3.12}$$

$$L = \sqrt{10}[d^\dagger \times \tilde{d}]^{(1)} \tag{3.13}$$

$$Q^\chi = [s^\dagger \times \tilde{d} + d^\dagger \times s] + \chi [d^\dagger \times \tilde{d}]^{(2)} \tag{3.14}$$

$$T^{(3)} = [d^\dagger \times \tilde{d}]^{(3)} \tag{3.15}$$

$$T^{(4)} = [d^\dagger \times \tilde{d}]^{(4)}. \tag{3.16}$$

One can also rewrite the Hamiltonian from Eq. 3.10 without the pairing term ($P^\dagger \cdot P$) and with the parameter χ not fixed to the value $-\frac{\sqrt{7}}{2}$ by

$$H = E_0^{''} + \epsilon^{'} n_d + a_1^{'} L \cdot L + a_2^{'} Q^\chi \cdot Q^\chi + a_3^{'} T^{(3)} \cdot T^{(3)} + a_4^{'} T^{(4)} \cdot T^{(4)}. \tag{3.17}$$

3.2.4 The three dynamical symmetries: U(5), SU(3), O(6)

Now, one wishes to diagonalize the Hamiltonian. A clever way to do so, is to know the states, which have "good" quantum numbers. The technique used is to decompose the "parent" algebra U(6) into chain of subalgebras, each of them characterized by different quantum numbers. A subalgebra is generated by a subset of the generators of the full algebra U(6). For example, from the 36 generators G of U(6) (Eqn. 3.7), one considers only the generators using the d-bosons: $G^{(L)}_\mu(d,d)$ with L =0, 1, 2, 3, 4. This new set of generators happens to close under commutation (*i.e* the commutator of any two generators belonging to the subalgebra is expressible in terms of generators belonging to the same subalgebra only). These 25 operators happen to be the generators of the algebra U(5), the group of unitary transformation in 5 dimensions. It turns out that there are only three possible chains of subalgebra decomposing the "parent" algebra U(6) and containing the required O(3) subalgebra:

$$\begin{array}{ccccccccccccc}
U(6) & \supset & U(5) & \supset & & O(5) & \supset & & O(3) & \supset & O(2) & (I) & (3.18) \\
N & & n_d & & & v & & & L & & M & & \\
U(6) & & & \supset & SU(3) & & \supset & & O(3) & \supset & O(2) & (II) & (3.19) \\
N & & & & (\lambda,\mu) & K & & & L & & M & & \\
U(6) & \supset & O(6) & \supset & & O(5) & \supset & & O(3) & \supset & O(2) & (III) & (3.20) \\
N & & \sigma & & & \tau & & n_\Delta & L & & M & &
\end{array}$$

For each subalgebra, one can find operators which commute with all generators of this subalgebra. Such operators are called Casimir operators and are usually labeled by C. The general Hamiltonian from Eq. 3.10 can then be rewritten in terms of Casimir operators:

$$\begin{aligned} H = {} & e_0 + e_1 C_1[U(6)] + e_2 C_2[U(6)] + \eta C_2[O(6)] + \tilde{\epsilon} C_1[U(5)] \\ & + \alpha C_2[U(5)] + \beta C_2[O(5)] + \delta C_2[SU(3)] + \gamma C_2[O(3)] + \rho C_1[O(2)]. \end{aligned} \tag{3.21}$$

The forms of the Hamiltonian from Eq. 3.21 and Eq. 3.10 are equivalent and

$$\begin{aligned} \tilde{\epsilon} &= \epsilon + \frac{18}{35} a_4 \\ \eta &= -\frac{1}{8} a_0 \\ \gamma &= \frac{a_1}{2} - \frac{3}{16} a_2 - \frac{1}{20} a_3 - \frac{1}{28} a_4 \\ \delta &= \frac{3}{4} a_2 \\ \beta &= \frac{a_3}{4} - \frac{3}{28} a_4 \\ \alpha &= \frac{18}{35} a_4. \end{aligned}$$

The U(5) symmetry

The U(5) symmetry corresponds to the chain (I) (Eq. 3.18) where the general Hamiltonian from Eq. 3.21 can be simplified by considering only the Casimir operators of the subalgebras involved in this chain (*i.e* $\eta = \delta = 0$). The basis states of this symmetry are defined by $|N, n_d, v, v_\Delta, L, M\rangle$ with

$$n_d \in 0, 1, ..., N \tag{3.22}$$

$$v \in n_d, n_d - 2, ..., 0 \text{ (n}_d\text{=even) or 1 (n}_d\text{=odd)} \tag{3.23}$$

$$v_\Delta \in 0, 1, ..., [v/3] \tag{3.24}$$

$$L \in \lambda, \lambda+1, ..., 2\lambda-2, 2\lambda \text{ with} \tag{3.25}$$

$$\lambda = v - 3v_\Delta, \tag{3.26}$$

where N is the total number of bosons, n_d the number of d bosons, v is called the seniority and is defined as the number of boson pairs not coupled to zero angular momentum, v_Δ is chosen as the number of d-boson triplets coupled to zero angular momentum, L is the total angular momentum and M is its projection. By construction, the U(5) Hamiltonian is diagonal in the U(5) basis with eigenvalues

$$E^{(I)}(N, n_d, v, n_\Delta, L, M) = E_B + \tilde{\epsilon} n_d + \alpha n_d(n_d + 4) + 2\beta v(v+3) + 2\gamma L(L+1) + 2\rho M \tag{3.27}$$

with $E_B = e_0 + e_1 N + e_2 N(N+5)$. One can then “construct” an energy spectrum reflecting the U(5) symmetry for a given boson number N (see Fig. 2.1 in [29]). Note that the ratio $R_{4/2} = E(4_1^+)/E(2_1^+)$ is about 2 if the parameter $\tilde{\epsilon} \gg \alpha$, β, γ. The energy level pattern of the U(5) symmetry is similar to the one from a vibrational nucleus and when $N \to \infty$, the U(5) limit corresponds to the anharmonic quadrupole vibrator of the geometrical model [24].

The SU(3) symmetry

The SU(3) symmetry corresponds to the chain (II) (Eq. 3.19) where the general Hamiltonian from Eq. 3.21 can be simplified by considering only the Casimir operators of the subalgebras involved in this chain (*i.e* $\eta = \tilde{\epsilon} = \alpha = \beta = 0$). The basis states of this symmetry are defined by $|N, (\lambda, \mu), K, L, M\rangle$ with

$$
\begin{aligned}
(\lambda,\mu) &\in (2n,0),(2n-4,2),...,\begin{cases}(0,n) \text{ n even}\\(2,n-1) \text{ n odd}\end{cases} && (3.28)\\
\text{with } n &\in N, N-3, ..., N \text{ mod3} && (3.29)\\
K &\in 0,2,...,\min(\lambda,\mu) && (3.30)\\
L &\in K, K+1, ..., K + \max(\lambda,\mu), && (3.31)
\end{aligned}
$$

where only the even values of L are allowed for $K = 0$. For the magnetic substates M, one has $M \in -L, ..., L-1, L$. By construction, the SU(3) Hamiltonian is diagonal in the SU(3) basis with eigenvalues

$$
E^{(II)}(N, n_d, v, v_\Delta, L, M) = E_B + \frac{2}{3}\delta\left[\lambda^2 + \mu^2 + \lambda\mu + 3(\lambda+\mu)\right] + \gamma 2L(L+1) + 2\rho M. \qquad (3.32)
$$

A typical energy spectrum reflecting the SU(3) symmetry is shown in [29] (Fig. 2.2). Note that, the ratio $R_{4/2} = E(4_1^+)/E(2_1^+)$ is exactly 10/3≈3.33. In the case $N \to \infty$, the SU(3) limit corresponds to the axial symmetric rotor in the framework of the geometrical model [24].

The O(6) symmetry

The O(6) symmetry corresponds to the chain (III) (Eq. 3.20) where the general Hamiltonian from Eq. 3.21 can be simplified by considering only the Casimir operators of the subalgebras involved in this chain (*i.e* $\tilde{\epsilon} = \alpha = \delta = 0$).

The basis states of the O(6) symmetry are defined by the quantum numbers $|N, \sigma, \tau, n_\Delta, L, M\rangle$ whose values are given by:

$$
\begin{aligned}
\sigma &\in N, N-2, ..., 0 \text{ (N=even) or 1 (N=odd)} && (3.33)\\
\tau &\in 0, 1, ..., \sigma && (3.34)\\
n_\Delta &\in 0, 1, ..., [\tau/3] && (3.35)\\
L &\in \lambda, \lambda+1, ..., 2\lambda-2, 2\lambda \text{ with} && (3.36)\\
\lambda &= \tau - 3n_\Delta, && (3.37)
\end{aligned}
$$

where τ is the boson seniority, *i.e* the number of boson pairs not coupled to zero angular momentum and v_Δ is the number of d-boson triplets coupled to zero angular momentum. The physical meaning of σ is more complex and is not discussed here. By construction, the O(6) Hamiltonian is diagonal in the O(6) basis with eigenvalues

$$
E^{(III)}(\sigma, \tau, n_\Delta, L, M) = E_B + 2\eta\sigma(\sigma+4) + 2\beta\tau(\tau+3) + 2\gamma L(L+1) + 2\rho M. \qquad (3.38)
$$

A typical energy spectrum reflecting the O(6) symmetry is shown in [29] (Fig. 2.3). Note that the ratio $R_{4/2} = E(4_1^+)/E(2_1^+)$ is about 2.5 if $\gamma \ll \beta$. For $N \to \infty$, the O(6) limit corresponds in the geometrical model to the γ-soft (or γ-unstable) rotors of Wilets and Jean [31].

3.2.5 Electromagnetic transition operators

Besides excitation energy spectra, the IBM is also able to describe electromagnetic transition rates as well. To do so, one needs to define the transition operators in terms of boson operators. They are defined as

$$
\begin{aligned}
T(E0) &= \epsilon_{0,s}\frac{n_s}{N} + \epsilon_{0,d}\frac{n_d}{N} && (3.39)\\
T(M1) &= \sqrt{\frac{3}{4\pi}}gL && (3.40)\\
T(E2) &= e_B Q^\chi && (3.41)\\
T(M3) &= \beta_3 T^{(3)} && (3.42)\\
T(E4) &= \beta_4 T^{(4)}, && (3.43)
\end{aligned}
$$

where $\epsilon_{0,s}$, $\epsilon_{0,d}$,g,e_B,β_3 and β_4 are boson effective charges which have to be adjusted to the experimental values. They should stay constant for all electromagnetic transitions in the same nucleus but are allowed to vary from one nucleus to another.

3.2.6 Consistent Q Formalism (CQF)

The most general one-boson quadrupole operator is written as in Eq. 3.14, *i.e* $Q^{\chi} = [s^{\dagger} \times \tilde{d} + d^{\dagger} \times s] + \chi [d^{\dagger} \times \tilde{d}]^{(2)}$ with the parameter χ free to be chosen. This operator is conveniently employed both in the quadrupole-quadrupole interaction term $Q^{\chi} \cdot Q^{\chi}$ in the Hamiltonian and as the electric quadrupole transition operator $T(E2)$ from Eq. 3.41. Although in principle these two values of χ do not necessarily need to be the same, "consistency" is assured by assuming they are the same. This is the so called "Consistent Q Formalism" (CQF) [32]. The further assumption of the CQF is to simplify the Hamiltonian from Eq. 3.17 to

$$\begin{aligned} H_{CQF} &= \epsilon n_d + \kappa Q^{\chi} \cdot Q^{\chi} + \lambda L \cdot L && (3.44) \\ &= \kappa (\tfrac{\epsilon}{\kappa} n_d + Q^{\chi} \cdot Q^{\chi} + \tfrac{\lambda}{\kappa} L \cdot L). && (3.45) \end{aligned}$$

In Eq. 3.45, the energy eigenvalues will depend on the four parameters $(\epsilon, \kappa, \chi, \lambda)$. The parameter κ sets the energy scale and should be always negative since the quadrupole interaction is attractive. The parameter λ/κ does not change the structure of the wave functions since $L \cdot L$ is diagonal. The structure of the wave functions will then depend only on ϵ/κ and χ. Finally, for the three dynamical symmetries we have the parametrization

$$\begin{aligned} -\epsilon/\kappa &= \infty, & \chi &= 0 & U(5) && (3.46) \\ -\epsilon/\kappa &= 0, & &\begin{cases} \chi = \frac{\sqrt{7}}{2} \text{ oblate} \\ \chi = -\frac{\sqrt{7}}{2} \text{ prolate} \end{cases} & SU(3) && (3.47) \\ -\epsilon/\kappa &= 0, & \chi &= 0 & O(6). && (3.48) \end{aligned}$$

Fig. 3.1 shows the $(\epsilon/\kappa,\chi)$ plane of the CQF Hamiltonian from Eq. 3.45. The three dynamical symmetries points are also spotted.

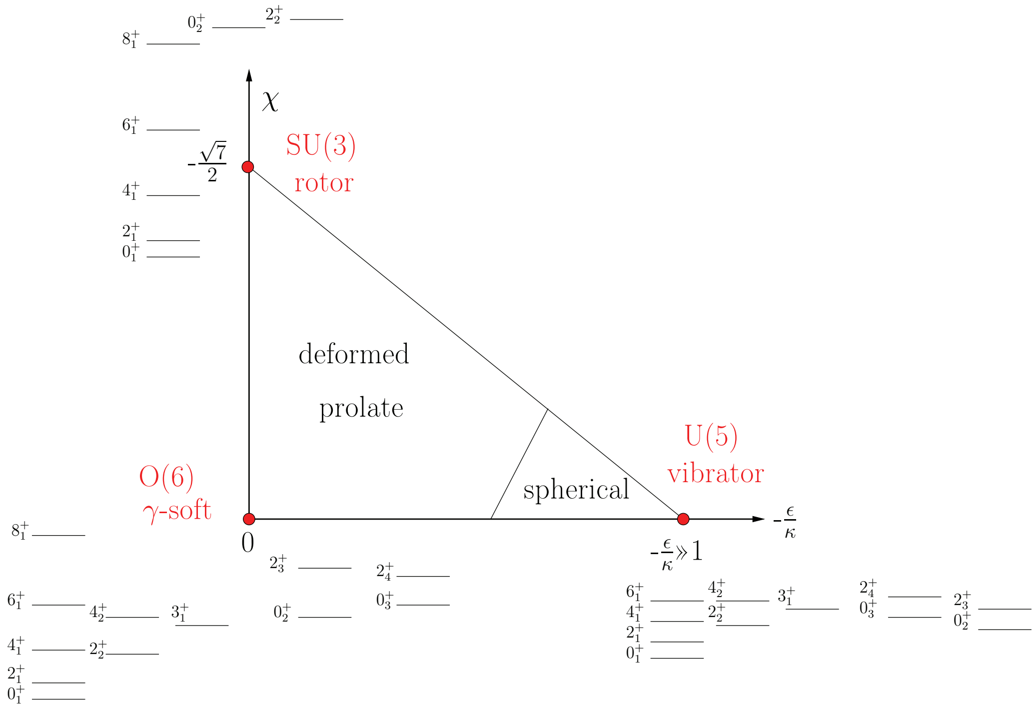

Figure 3.1: Symmetry triangle of the IBM as a function of the two structure parameters $(\epsilon/\kappa,\chi)$ of the CQF Hamiltonian from Eq. 3.45. For each symmetry is sketched the corresponding schematic low-lying levels structure.

By neglecting the term $L \cdot L$ in Eq. 3.45, one obtains the Hamiltonian of the Extended Consistent Q Formalism [33], which can be parametrized as in [34] by

$$H_{ECQF} = a \left[(1-\zeta) n_d - \frac{\zeta}{4N} Q^{\chi} \cdot Q^{\chi} \right]. \tag{3.49}$$

This parametrization $\zeta = 1/[1-\epsilon/(4N\kappa)$, $a = \epsilon - 4N\kappa$ was used recently in the discussion of shape phase transitions. It has the advantage that infinite values for structural parameters are avoided. The parameter a sets the absolute energy scale, the wave functions depend only on the two structural constants (ζ,χ). The ECQF Hamiltonian covers the three dynamical symmetry limits with $\zeta = 0$ [U(5)], $(\zeta = 1, \chi = 0)$ [O(6)] and $(\zeta = 1, \chi = -\sqrt{7}/2)$ [SU(3)]. The relations between different parameters of the ECQF Hamiltonian can be found in [35].

3.3 sd-IBM-2

The extended version of the IBM-1 is the IBM-2 which differentiates between proton bosons and neutron bosons [36, 37, 29]. Thus the model space is constructed from the two kinds of s- and d-bosons operators

$$\begin{array}{ll} s^\dagger_\rho, d^\dagger_{\rho,\mu} & (\mu = 0, \pm 1, \pm 2), \\ \tilde{s}_\rho, \tilde{d}_{\rho,\mu} & (\mu = 0, \pm 1, \pm 2), \end{array}$$

with $\rho = \pi, \nu$ for protons and neutrons respectively. The underlying algebra of the IBM-2 is $U_\pi(6) \times U_\nu(6)$, with the subgroup $U_{\pi+\nu}(6)$ derived by just adding the generators of $U_\pi(6)$ and $U_\nu(6)$. Analogically to the reduction chains of the IBM-1, one finds such chains also for the IBM-2, leading to the dynamical symmetry limits, *e.g* $U_{\pi+\nu}(5)$, $SU_{\pi+\nu}(3)$, or $O_{\pi+\nu}(6)$. The whole formalism of the IBM-2 is similar to the one of the IBM-1 and will not be treated here. However, adding the proton neutron degree of freedom to the sd-IBM-1 leads to some interesting properties of the nucleus which can exist only in the IBM-2. The best example here is the existence of eigenstates where protons and neutrons are not fully in phase, the so-called *Mixed-Symmetry States* (MSSs). In order to establish the properties of such states, we introduce the F-spin formalism [37].

3.3.1 F-spin

The F-spin formalism is analogous to the isospin formalism of nucleons. Proton bosons and neutron bosons have $F = 1/2$ and the z-projection is $F_z = +1/2$ for protons and $F_z = -1/2$ for neutrons. For a system of N_π proton bosons and N_ν neutron bosons, the maximum F-spin is $F = F_{max} = (N_\pi + N_\nu)/2$ and

$$F_z = \frac{|N_\pi + N_\nu|}{2} \leq F \leq F_{max} = \frac{N_\pi + N_\nu}{2}. \tag{3.50}$$

In the F-spin space, one can also define the creation and annihilation operators F_+ and F_- by

$$F_+ = s^\dagger_\pi s_\nu + \sum_\mu d^\dagger_{\pi,\mu} d_{\nu,\mu}, \tag{3.51}$$

$$F_- = s^\dagger_\nu s_\pi + \sum_\mu d^\dagger_{\nu,\mu} d_{\pi,\mu}. \tag{3.52}$$

The projection operator F_z is given by

$$F_z = \frac{1}{2}\left[(s^\dagger_\pi s_\pi + \sum_\mu d^\dagger_{\pi,\mu} d_{\pi,\mu}) - (s^\dagger_\nu s_\nu + \sum_\mu d^\dagger_{\nu,\mu} d_{\pi,\mu}) \right]. \tag{3.53}$$

A state composed by N_π proton bosons and N_ν neutron bosons with F-spin quantum number $F = F_{max}$ can be transformed by the successive action of the F-spin raising operator F_+ into a state that consists of proton bosons only. This state has still a total F-spin quantum number $F = F_{max}$ since the raising operator does not change the total F-spin quantum number. This new state has only proton bosons and obviously stays unchanged under a pairwise exchange of proton and neutron labels. Therefore, IBM-2 states with $F = F_{max}$ are called *Full Symmetry States* (FSSs). These states corresponds actually to the IBM-1 states which are all symmetric. All others states with F-spin quantum numbers $F < F_{max}$ contain pairs (at least one) of proton and neutron bosons that are antisymmetric under a pairwise exchange of protons and neutrons labels. They are called *Mixed-Symmetry States* (MSSs). An example of these two types of states is shown in Fig. 3.2.

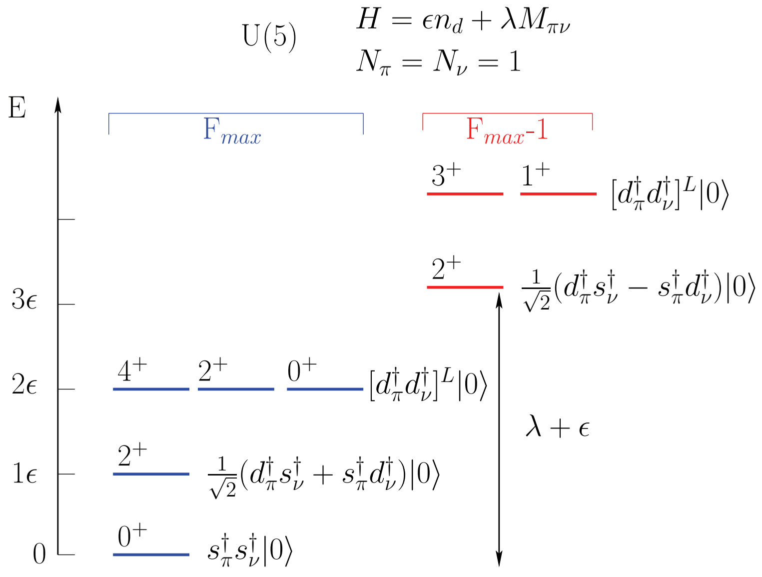

Figure 3.2: Low-lying collective states in the U(5) symmetry for $N_\pi = N_\nu = 1$. The Full Symmetry States (FSS) are those with $F = F_{max}$ (blue) and the Mixed-Symmetry States (MSS) are those with $F = F_{max} - 1$ (red). The boson wave functions are also displayed where $0\rangle$ denotes the boson vacuum and $[]^L$ denotes tensor coupling to rank L. The operator $M_{\pi\nu}$ corresponds to the Majorana operator of Eq. 3.56.

A comprehensive review of the F-spin symmetry of the IBM-2 has been given by Van Isacker *et al.* [38]. One important result of the F-spin formalism is given by the proton-neutron contribution to the matrix elements of any one-body operator between FSSs

$$\langle F_{max},\alpha||b^\dagger_{\rho,\beta}b_{\rho,\beta'}||F_{max},\alpha'\rangle = N_\rho c_{\alpha\alpha'\beta\beta'}, \tag{3.54}$$

where $\alpha,\alpha',\beta,\beta'$ are additional quantum numbers and $c_{\alpha\alpha'\beta\beta'}$ is independent of ρ. This major result tells us that there are no $M1$ transition between FSSs (see section 3.3.3).

3.3.2 Hamiltonian of the IBM-2

The Hamiltonian of the IBM-2 can be written as

$$H = H_\pi + H_\nu + V_{\pi\nu}, \tag{3.55}$$

where $H_{\rho=\pi,\nu}$ corresponds to the Hamiltonian of Eq. 3.8 by replacing the original boson operators $(b^\dagger,\tilde{b})$ by the proton boson operators $(b^\dagger_\pi,\tilde{b}_\pi)$ and the neutron boson operators $(b^\dagger_\nu,\tilde{b}_\nu)$. The third term in Eq. 3.55, $V_{\pi\nu}$ quantifies the proton-neutron interaction. $H_{\rho=\pi,\nu}$ can be written in a multipole expansion analog to that of the IBM-1 given in Eq. 3.10. However one often uses a shortened multipole expansion version of the Hamiltonian (3.55) including only the n_{d_ρ} boson operators and the quadrupole interaction. Additionally, the Majorana operator

$$M_{\pi\nu}(\xi_1,\xi_2,\xi_3) = \xi_2[s_\nu^\dagger\times d_\pi^\dagger - s_\pi^\dagger\times d_\nu^\dagger]^{(2)}\cdot[\tilde{s}_\nu\times\tilde{d}_\pi - \tilde{s}_\pi\times\tilde{d}_\nu]^{(2)} - 2\sum_{k=1}^{3}\xi_k[d_\nu^\dagger\times d_\pi^\dagger]^{(k)}\cdot[\tilde{d}_\nu\times\tilde{d}_\pi]^{(k)} \tag{3.56}$$

is introduced to describe interaction between protons and neutrons. This operator causes an overall energy shift for MSSs ($F < F_{max}$) and the simplified Hamiltonian becomes

$$H = \epsilon_\pi n_{d_\pi} + \epsilon_\nu n_{d_\nu} + \kappa_{\pi\pi}Q_\pi^{\chi_\pi}\cdot Q_\pi^{\chi_\pi} + 2\kappa_{\pi\nu}Q_\pi^{\chi_\pi}\cdot Q_\nu^{\chi_\nu} + \kappa_{\nu\nu}Q_\nu^{\chi_\nu}\cdot Q_\nu^{\chi_\nu} + M_{\pi\nu}(\xi_1,\xi_2,\xi_3). \tag{3.57}$$

Usually the quadrupole interaction between non-identical nucleons is known to be large. Thus, one often omits the proton-proton and the neutron-neutron parts of the quadrupole-quadrupole interaction so that the Hamiltonian is reduced to

$$H = E_0 + \epsilon_\pi n_{d_\pi} + \epsilon_\nu n_{d_\nu} + 2\kappa_{\pi\nu} Q^{\chi_\pi}_\pi \cdot Q^{\chi_\nu}_\nu + M_{\pi\nu}(\xi_1, \xi_2, \xi_3). \tag{3.58}$$

3.3.3 Electromagnetic transition operators

The transition operators are sums over the proton and neutron transition operators of the IBM-1 which are given in section 3.2.5. For example, in the IBM-2, the $M1$ and $E2$ operators are given by

$$\begin{aligned} T(M1) &= \sqrt{\frac{3}{4\pi}}(g_\pi L_\pi + g_\nu L_\nu), && (3.59)\\ T(E2) &= e_\pi Q^{\chi_\pi}_\pi + e_\nu Q^{\chi_\nu}_\nu. && (3.60) \end{aligned}$$

Both operators can be divided into F-scalar (denoted by s) and F-vector (denoted by v) parts

$$\begin{aligned} T(M1)_s &= \frac{g_\pi + g_\nu}{2}(L_\pi + L_\nu) && (3.61)\\ T(M1)_v &= \frac{g_\pi - g_\nu}{2}(L_\pi - L_\nu) && (3.62)\\ T(E2)_s &= \frac{e_\pi + e_\nu}{2}(Q^{\chi_s}_\pi + Q^{\chi_s}_\nu) && (3.63)\\ T(E2)_v &= \frac{e_\pi - e_\nu}{2}(Q^{\chi_v}_\pi - Q^{\chi_v}_\nu), && (3.64) \end{aligned}$$

with

$$\begin{aligned} \chi_s &= \frac{e_\pi \chi_\pi + e_\nu \chi_\nu}{e_\pi + e_\nu} && (3.65)\\ \chi_v &= \frac{e_\pi \chi_\pi - e_\nu \chi_\nu}{e_\pi - e_\nu}. && (3.66) \end{aligned}$$

The g_ρ are the orbital g-factors usually set to $g_\pi = 1$ and $g_\nu = 0$ while e_ρ are effective charges (usually $e_\nu \approx 0$).
If we rewrite the $M1$ transition operator of Eq. 3.59 one obtains

$$T(M1) = \sqrt{\frac{3}{4\pi}}\left[\frac{N_\pi g_\pi + N_\nu g_\nu}{N}(L_\pi + L_\nu) + (g_\pi - g_\nu)\frac{N_\pi N_\nu}{N}(\frac{L_\pi}{N_\pi} - \frac{L_\nu}{N_\nu})\right]. \tag{3.67}$$

By construction, the first term in Eq. 3.67 is diagonal in IBM-2 and hence can not induce transitions between different states. The second term in Eq. 3.67 vanishes for transitions between FSSs. This can be easily seen by using Eq. 3.54 and the definition of the angular momentum operators $L_\rho = \sqrt{10}[d^\dagger_\rho \times \tilde{d}_\rho]^{(1)}$. In contrast to that, the F-vector term does not vanish between MSSs and FSSs. Thus, the MSS which are defined by $F = F_{max} - 1$ have an allowed F-vector ($\Delta F = 1$) $M1$ transition to FSSs. This is important because in the IBM-1 framework all $M1$ transitions are forbidden. Thus such allowed $M1$ transitions between MSSs and FSSs can serve as an outstanding signature for mixed-symmetry character. Since $g_\pi - g_\nu \simeq 1\mu_N$ one can expect $M1$ matrix elements of about 1 μ_N. At the dynamical symmetries U(5), SU(3) and O(6), the matrix elements of the $T(M1)$ and $T(E2)$ operators can be calculated analytically [38]. It turns out that in the region relevant to the discussion of MSSs (in this work U(5) and O(6)), $E2$ transitions between FSSs are proportional to $(e_\pi N_\pi + e_\nu N_\nu)^2$ and $E2$ transitions between MSSs and FSSs are proportional to the expression $(e_\pi - e_\nu)^2 N_\pi N_\nu$. Another more intuitive way to describe the MSSs is given by the Q-phonon scheme which is described below.

3.3.4 The Q-phonon scheme

From the quadrupole collectivity of the low-lying states in even-even nuclei, one learns that the first excited state is almost always a 2_1^+ state, then comes the 4_1^+ state, the 6_1^+ state and so on. Therefore it is intuitive to build this low-lying excitations level scheme by using the $E2$ operator Q. In that sense each state is produced by Q phonon excitations, hence the name of this model, which has been invented by Otsuka, Siems and von Brentano [39, 40]. The first 2^+ is then created by acting the quadrupole operator Q on the ground state. In the framework of the IBM-1, it has been shown by Pietralla *et al.* [41] by calculations over the whole parameter space of the ECQF Hamiltonian (see section 3.2.6) that this assumption holds within only a few percent for all nuclei. Then the first excited 4_1^+ state is created by acting the quadrupole operator Q on the 2_1^+ state and so on.

In the IBM-2 there are two types of quadrupole operators (Q_π for protons and Q_ν for neutrons) so that the Q-phonon scheme can be expanded for the description of MSSs. For a symmetric coupling of proton and neutron quadrupole operators one obtains a proton-neutron symmetric Q_s-phonon by:

$$Q_s = Q_\pi + Q_\nu. \tag{3.68}$$

The antisymmetric combination of Q_π and Q_ν creates the MSS and is defined by

$$Q_m = Q_\pi - aQ_\nu, \tag{3.69}$$

where a assures the orthogonality between symmetric and antisymmetric Q-phonons and

$$Q_\rho^\chi = [s_\rho^\dagger \times \tilde{d}_\rho + d_\rho^\dagger \times s_\rho] + \chi_\rho [d_\rho^\dagger \times \tilde{d}_\rho]^{(2)}. \tag{3.70}$$

Using the Q-phonon formalism, one can write the unormalized wave functions of the lowest-lying fully symmetric and mixed-symmetry states in a compact way as Q-phonon excitations from the ground state $|0_1^+\rangle$:

$$\begin{aligned}
|2_1^+\rangle &= Q_s|0_1^+\rangle && (3.71)\\
|2_{1,\mathrm{ms}}^+\rangle &= Q_m|0_1^+\rangle && (3.72)\\
|4_1^+\rangle &= [Q_sQ_s]^{(4)}|0_1^+\rangle && (3.73)\\
|3_{1,\mathrm{ms}}^+\rangle &= [Q_sQ_m]^{(3)}|0_1^+\rangle && (3.74)\\
|1_{1,\mathrm{ms}}^+\rangle &= [Q_sQ_m]^{(1)}|0_1^+\rangle. && (3.75)
\end{aligned}$$

By coupling two Q_s-phonons one obtains a multiplet of states with $J^\pi = 0^+, 2^+, 4^+$. The coupling between a Q_m-phonon and a Q_s-phonon lead to a quintuplet with $J^\pi = 0^+, 1^+, 2^+, 3^+, 4^+$ since the nature of the two phonons are different. A schematic picture of the Q-phonon scheme is shown in Fig. 3.3. It shows that a strong collective $E2$ transition is expected between the first symmetric excited 2_1^+ state and the ground state while the $E2$ transition from the one-phonon mixed symmetry state $2_{1,\mathrm{ms}}^+$ to the ground state should be weak. This can be quantitatively understood by the minus sign in the Q_m operator which leads to partial cancellation of the proton and neutron $E2$ matrix elements. This result can be generalized in the case of multi-phonon states: the creation or annihilation of a Q_s-phonon should lead to a strongly collective $E2$ excitation, while the creation or annihilation of a Q_m-phonon leads to a weakly collective $E2$ transition. By evaluating the $M1$ and the quadrupole operator in the IBM-2 one obtains large $M1$ transitions between states where a Q_s-phonon changes to a Q_m-phonon and vice versa.

3.3.5 Signatures for Mixed-Symmetry States

From the previous discussion concerning the $E2$ and $M1$ decays of full symmetric states and the mixed-symmetry states (here discussed in near vibrational nuclei), we expect following signatures for mixed-symmetry one-phonon and two-phonon excitations for vibrational and transitional nuclei:

- The one-quadrupole-phonon $2_{1,\mathrm{ms}}^+$ state is the lowest-lying MSS in vibrational nuclei.
- The $2_{1,\mathrm{ms}}^+$ state decays to the 2_1^+ state by a strong $M1$ transition ($\langle 2_{1,\mathrm{ms}}^+ || T(M1) || 2_1^+ \rangle \approx 1\ \mu_N$).
- A weakly collective $E2$ transition strength of a few W.u. for the $2_{1,\mathrm{ms}}^+ \rightarrow 0_1^+$ transition.

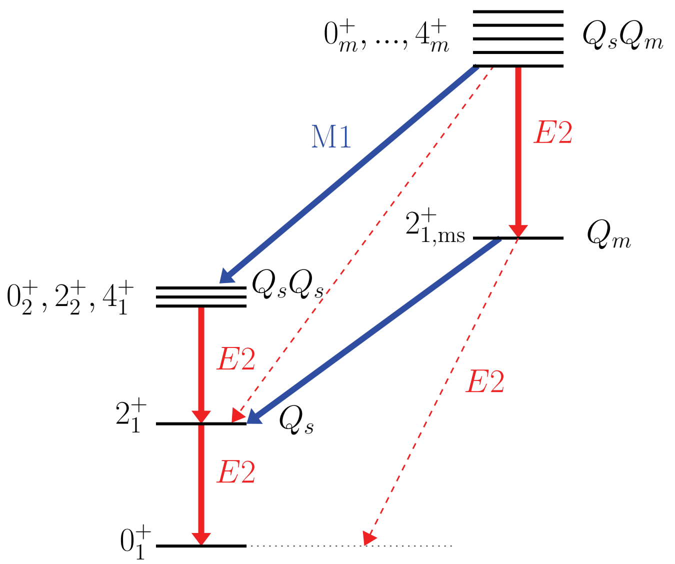

Figure 3.3: Schematic picture of the low-lying one- and two-phonon states in the Q-phonon scheme. Dashed red arrows represent weakly collective $E2$ transitions. The solid $E2$ arrows correspond to strongly collective $E2$ transitions. $M1$ transitions occur by the exchange of one phonon Q_s with one phonon Q_m.

- Two-phonon MSSs decay by a collective $E2$ transition to the one-phonon $2^+_{1,\mathrm{ms}}$ state.
- Two-phonon MSSs decay by a strong $M1$ transition to the symmetric two-phonon states with a matrix element of about 1 μ_N.
- Two-phonon MSSs should not decay by a strong $M1$ transition to the symmetric 2^+_1 state [42, 43, 44].
- Two-phonon MSSs should instead decay to the symmetric 2^+_1 state by a weakly collective $E2$ transition.
- All MSSs are very short lived ($t_{1/2} = 10 - 100$ fs).

3.3.6 Geometric picture of Mixed-Symmetry States

Another even more instructive way is to have a geometrical representation of the so-called MSSs. This is illustrated in Fig. 3.4. The symmetric states corresponds to in phase vibrations of protons and neutrons. For MSSs the proton and neutron vibrations are out of phase. This leads to different geometrical oscillations depending on either the nucleus is deformed or not. In the rotational limit [SU(3)], the ground state looks deformed but axially symmetric. Its shape can be either prolate or oblate. In these nuclei the non symmetric mode of vibration is called the “scissors mode” (from the geometrical picture that it gives). In spherical nuclei [U(5)], the MSSs are just out of phase oscillations of protons against neutrons arround the spherical ground state. The O(6) symmetry corrsponds to γ-unstable nuclei. They can be visualized as soft nuclei continuously changing their shape from prolate to oblate and vice versa.

The first experimentally observed case of mixed-symmetry state was the 1^+ scissors mode in deformed nuclei discovered by A. Richter *et al.* in 1984 [45]. The scissors mode in heavy nuclei typically lies at an energy of about 3 MeV. The scissors mode have been extensively reviewed in Refs. [10, 11, 12]. In weakly deformed vibrational and transitional nuclei, first examples for the $2^+_{1,\mathrm{ms}}$ were suggested by Hamilton *et al.* in 1984 [46] from the analysis of the $E2/M1$ mixing ratios. Based on similar arguments several authors suggested the existence of mixed-symmetry character in different mass regions [47, 48, 49, 50, 51]. However, a small value of the $E2/M1$ mixing ratio is not a safe criterion to affirm the existence of MSSs. The ineluctable proof for their existence is the large $B(M1)$ value to proton-neutron symmetrical phonon excitations with the same phonon number (typically 0.1-1.0 μ_N^2). In this work we focus only on the one-quadrupole phonon mixed symmetry state ($2^+_{1,\mathrm{ms}}$) in the isotopic Xe chain. The one-phonon and two-phonon MSSs of vibrational or transitional nuclei that were identified from measurements of the $M1$ matrix elements by different experimental techniques is reviewed in [9]. In our case one has to measure the large $[B(M1; 2^+_{1,\mathrm{ms}} \rightarrow 2^+_1)]$ which does not correspond to the excitation transition ($0^+_1 \rightarrow 2^+_{1,\mathrm{ms}}$). This is in contrast with the detection of the 1^+ scissors mode where the large $B(M1)$ value corresponds to the excitation mechanism (*i.e* $0^+_1 \rightarrow 1^+_{sc}$) in electron and photon scattering reaction. Consequently one has to use or combine different experimental techniques. In 2001, Pietralla *et al.* used a new technique

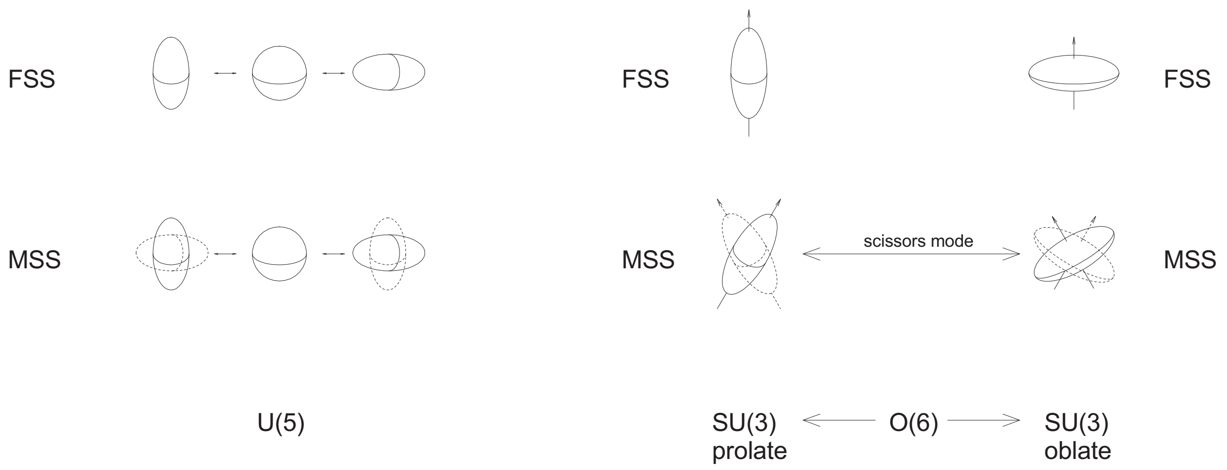

Figure 3.4: Schematic geometrical illustration of the FSSs (symmetric) and MSSs (non symmetric) for vibrational nuclei [U(5)] and for deformed nuclei [SU(3)] in IBM-2. In O(6) the shape oscillates between prolate and oblate. The neutron distribution is indicated by a solid line while the proton distribution by a dashed line.

for the identification of the MSSs in vibrational nuclei, the so called "Coulomb excitation in inverse kinematics". It was a great success which established the power of this new method. This technique could be possibly applied to radioactive nuclei and opens new exploration horizons in the neutron rich and exotic nuclei regions. This experimental technique has been used in this work and will be described in section 5.

4 The O(5)-Confined-Beta-Soft model (O(5)-CBS)

The concept of dynamical symmetries applies to systems that show a hierarchy of lifted degeneracies due to compatible symmetries. For example, the three dynamical symmetries [15, 29] of the Interacting Boson Model (IBM), U(5) [13], SU(3) [52], and O(6) [53] provide valuable benchmarks for nuclear quadrupole collectivity at low and medium angular momenta. These three symmetries correspond to analytically solvable cases of the geometrical Bohr Hamiltonian [54] - the harmonic vibrator, the quadrupole-deformed axial rotor, and the γ-unstable rotor [31]. They are extremly useful in the analysis of experimental data but idealized cases are hardly ever observed in nuclei. However there are other classes of dynamic symmetries also related to exactly solvable problems describing systems undergoing phase transitions between the three dynamical symmetries of the algebraic structure U(6).

The critical-point description of the U(5)→SU(3) transition is denoted as X(5) [55] and corresponds to a first order phase transition. It involves the solution of the Bohr collective Hamiltonian with a potential decoupled into two compoments (by an approximately separation of the variables): an infinite square well potential in the quadrupole deformation parameter β, combined with a harmonic potential well for the triaxiality deformation parameter γ. Several nuclei close to the X(5) symmetry have already been well established: ^{150}Nd [56], ^{152}Sm [57], ^{154}Gd [58], ^{178}Os [59]. In 2004, Pietralla and Gorbachenko [60] showed that the properties of the 0_2^+ state (or band head of the so called "β-band") in the $N \approx 90$ shape transitional region is well described in a one-parameter analytical solution of the Bohr-Hamiltonian eigenvalue problem using an infinite square-well potential over a confined range of values for β. This solution is called "the confined-β-soft model" (CBS) which interpolates between the phase-transitional point X(5) and the rigid-rotor limit SU(3) in an analytic way. This model was successful and accounts well for energies as well as for $E2$ rates observed in transitional and strongly deformed nuclei in the rare earths and actinides ([60, 61, 62, 63]).

Similarly, the critical-point description of the U(5)→O(6) transition is denoted as E(5) and corresponds to a second order phase transition. In this case the Bohr Hamiltonian is solved with an infinite square well potential depending only on β (exact separation of the variables) [64]. IBM calculations indicate that the flat-bottomed potential is a fair approximation such as can arise in a transition region from γ-soft to harmonic vibrator (where deformed and spherical minima cross as shown in Fig. 2 of Ref. [64]). In 2005, in a way similar to the CBS model, Bonatsos *et al.* [65] interpolated between the phase-transitional point E(5) and the γ-soft rotor [O(5)] limit by using in the E(5) framework γ-independent infinite square-well potentials in β with boundaries $\beta_M > \beta_m \geq 0$. The model contains one free parameter, $r_\beta = \beta_m/\beta_M$. The case with $r_\beta = 0$ corresponds to the original E(5) model, and $r_\beta \rightarrow 1$ leads to the γ-soft rotor [O(5)] limit. This model is called "γ-soft analog of the confined β-soft rotor model" labeled here as O(5)-CBS. In the following, we will briefly explain the O(5)-model. For further details the reader is referred to [65].

We consider the Bohr Hamiltonian [54]

$$H = -\frac{\hbar^2}{2B}[\Delta_R + \frac{1}{\beta^2}\Delta_\Omega] + U(\beta), \tag{4.1}$$

with

$$\begin{aligned} \Delta_R &= \frac{1}{\beta^4}\frac{\partial}{\partial\beta}\beta^4\frac{\partial}{\partial\beta} = \frac{\partial^2}{\partial\beta^2} + \frac{4}{\beta}\frac{\partial}{\partial\beta}, & (4.2) \\ \Delta_\Omega &= \frac{1}{\sin 3\gamma}\frac{\partial}{\partial\gamma}\sin 3\gamma\frac{\partial}{\partial\gamma} - \sum_{k=1}^{3}\frac{L_k'^2(\theta_i)}{4\sin^2(\gamma - \frac{2\pi}{3}k)}, & (4.3) \end{aligned}$$

where β and γ are the usual collective coordinates, L_k' $(k = 1, 2, 3)$ are the components of angular momentum in the intrinsic frame, $\theta_i (i = 1, 2, 3)$ are the Euler angles, and B is the mass parameter. The potential $U(\beta)$ depends only on the collective coordinate β and is shown in Fig. 4.1.

By factorizing the wave function $\phi(\beta, \gamma, \theta_i) = F(\beta)\Phi(\gamma, \theta_i)$ [64, 31], one can separate the Schrödinger equation corresponding to the Hamiltonian 4.1 into two parts (angular and radial):

$$-\Delta_\Omega\Phi(\gamma, \theta_i) = \tau(\tau + 3)\Phi(\gamma, \theta_i), \tag{4.4}$$

$$\frac{d^2F(\beta)}{d\beta^2} + \frac{4}{\beta}\frac{dF(\beta)}{d\beta} + [\frac{2B}{\hbar^2}(E - U(\beta) - \frac{\tau(\tau+3)}{\beta^2}] \times F(\beta) = 0. \tag{4.5}$$

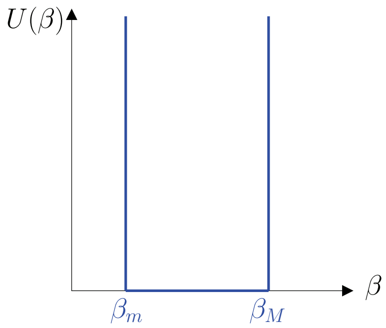

Figure 4.1: Infinite-well potential $U(\beta) = \begin{cases} 0, \beta_m \leq \beta \leq \beta_M \\ \infty, 0 \leq \beta < \beta_m, \beta > \beta_M \end{cases}$ used in the O(5)-CBS model.

where τ is the seniority quantum number (*i.e* number of particles which do not couple pairwise to total angular momentum $J = 0$). By defining $k^2 = 2BE/\hbar^2$ and substituting $F(\beta) = \beta^{-3/2}P(\beta)$, Eq. 4.5 in the interval $[\beta_m, \beta_M]$ takes the form of a Bessel equation of νth oder:

$$\beta^2 P''(\beta) + \beta P'(\beta) + (k^2\beta^2 - \nu^2)P(\beta) = 0, \tag{4.6}$$

where $\nu = \tau + 3/2$ and the boundaries condition $P(\beta_m) = 0$ and $P(\beta_M) = 0$. The general solution of Eq. 4.6 is the function

$$P(\beta) = aJ_\nu(k\beta) + bY_\nu(k\beta), \tag{4.7}$$

where $J_\nu(z)$ and $Y_\nu(z)$ are the Bessel functions of the first and second kind, respectively, of order $\nu = \tau + 3/2$. a and b are constants. The boundary conditions leads to

$$J_\nu(x)Y_\nu(r_\beta x) - J_\nu(r_\beta x)Y_\nu(x) = 0, \tag{4.8}$$

where $x = k\beta_M$ and $r_\beta = \beta_m/\beta_M$. By labeling the $x^{(r_\beta)}_{\xi\tau}$ the ξth positive root of Eq. 4.8 one obtains the energy spectrum

$$E_{\xi\tau}(r_\beta) = \frac{\hbar^2}{2B\beta_M^2}[x^{(r_\beta)}_{\xi\tau}]^2. \tag{4.9}$$

The normalized eigenfunctions $P^{(r_\beta)}_{\xi\tau}(\beta)$ can then be calculated using Eq. 4.8 and using the normalization condition

$$\int_{\beta_m}^{\beta_M} \beta^4 [F^{(r_\beta)}_{\xi\tau}(\beta)]^2 d\beta = \int_{\beta_m}^{\beta_M} \beta [P^{(r_\beta)}_{\xi\tau}(\beta)]^2 d\beta = 1. \tag{4.10}$$

Then the normalized solutions of Eq. 4.5 in the interval $[\beta_m, \beta_M]$ are

$$F^{(r_\beta)}_{\xi\tau}(\beta) = \beta^{-3/2} P^{(r_\beta)}_{\xi\tau}(\beta), \tag{4.11}$$

and the factorized wave functions are expressed

$$|r_\beta; \xi\tau\mu LM\rangle \equiv \phi^{(r_\beta)}_{\xi\tau\mu LM}(\beta, \gamma, \theta_i) = F^{(r_\beta)}_{\xi\tau}(\beta)\Phi^{\tau\mu}_{LM}(\gamma, \theta_i) \tag{4.12}$$

where $\mu = 0, 1, 2, ..., [\tau/3]$, and for a given value of μ the angular momentum L takes values $L = 2\rho, 2\rho - 2, 2\rho - 3, ..., \rho + 1, \rho$, where $\rho = \tau - 3\mu$. By expressing the angular part of the wave function according to [66] and using the quadrupole operator $T(E2)$ [65], one can calculate the reduced transition probabilities $B(E2)$. As an example, energy level spectra and $B(E2)$ transition rates are given in Fig. 4.2 for $r_\beta = 0.21$. Usually the unique parameter of this model (r_β) is fitted to the experimental $R_{4/2} = E(4^+_1)/E(2^+_1)$ energy ratio. The O(5)-CBS model will be used in this work to interpret the structure of the nucleus ^{128}Xe (see section 7.4).

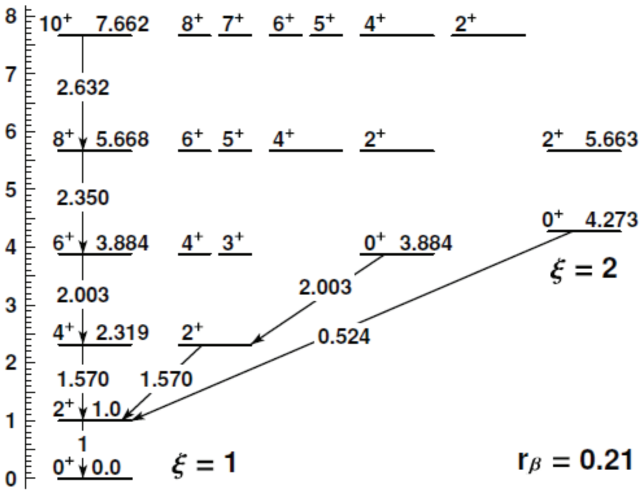

Figure 4.2: Energy levels (normalized to the excitation energy of the 2_1^+ state) and $B(E2)$ transition rates [normalized to $B(E2; 2_1^+ \rightarrow 0_1^+)$] for the structural parameter $r_\beta = \beta_m/\beta_M = 0.21$. Taken from [65].

5 Coulomb excitation theory

In Coulomb excitation (COULEX), the nucleus is excited by the Coulomb field of impinging charged projectiles passing the nucleus with velocity v at a short distance without penetrating into the range of nuclear forces. COULEX can be considered as an absorption process for virtual photons. In the early 1950's COULEX has become a major tool for γ-ray spectroscopy and it has been documented in several review articles [67, 68, 69, 70]. COULEX populates collective states relatively strongly and is therefore a well suited tool for studying collective excitations. The COULEX cross sections are directly related to the transition matrix elements for electromagnetic decay and thus the transition matrix elements can be obtained from the measurement of Coulomb excitation cross sections. The theory of COULEX also allows to calculate the angular distribution of γ-rays emitted from a Coulomb excited state. By measuring the angular distribution γ-rays, one can deduce the multipole mixing ratio (δ) of transitions of mixed multipolarity. In the following a brief summary of the COULEX technique is given.

5.1 Semi-classical theory of COULEX

In the semi-classical theory of COULEX, the projectile is considered to move in a classical trajectory, deflected by the Coulomb force steming from the electric field of the target. There are two basic assumptions for this semi-classical treatment. First, it is assumed that the interaction between the scattering ions is purely electromagnetic in origin, *i.e* there is no contribution from the nuclear forces of both interacting nuclei. Usually the condition is expressed in terms of the dimensionless Sommerfeld parameter η:

$$\eta = 2\pi \frac{a}{\lambda} = \frac{Z_1 Z_2 e^2}{\hbar v} >> 1, \tag{5.1}$$

where a denotes half the distance of closest approach in a head-on collision and is expressed as

$$a = \frac{Z_1 Z_2 e^2}{m_0 v^2}, \tag{5.2}$$

where Z_1 and Z_2 are the charge numbers of the projectile and the nucleus (index “1” always refers to projectile, “2” to target), e is the electric charge of the electron, m_0 is the reduced mass of the scattering problem, and λ is the wavelength of the incoming projectile with velocity v. The second assumption for the application of a classical description is that the energy loss of the particle (inelastic collisions) is small compared to the bombarding energy, so that the effect of the excitation on the particle motion can be neglected. In such a treatment, the nuclear excitation is a result of the time dependent electromagnetic field of the projectile acting on the nucleus which is small (in most cases) and may be treated by first-order quantum mechanical perturbation theory (see next part). It has been proven that this treatment is valid in almost all situations studied in Coulomb excitation at low energies [69]. For high energy collisions, because the nuclear interaction distorts the scattering waves appreciably, a quantum treatment might be necessary for some observables, e.g. angular distributions.
A simple and convenient semiclassical formula for estimating the maximum safe bombarding energy in head-on collisions has been given by Cline [71]:

$$E_{max}(MeV) = 1.44 \frac{A_1 A_2}{A_2} \cdot \frac{Z_1 Z_2}{1.25(A_1^{1/3} + A_2^{1/3}) + 5}, \tag{5.3}$$

where $A_{1,2}$ are the Mass numbers of the projectile and target. Criterion 5.3 corresponds to a minimum separation between the nuclear forces of about 5 fm which is required to ensure that the influence of nuclear excitation is $< 0.1\%$.

5.2 First-order time-dependent perturbation theory

A sufficient condition for the validity of the first oder perturbation theory approach is that all possible excitation probabilities are small. In order to excite an initial state $|i\rangle$ to a final excited state $|f\rangle$ via the time dependent electromagnetic interaction $V[\overrightarrow{r}(t)]$, the collision time $\tau_{coll} = a/v$ needs to be shorter or of the same magnitude as the excitation time for a given excitation energy $\Delta E = E_f - E_i$ in the nucleus, $\tau_{nuc} = \hbar/\Delta E$. This is reflected in the adiabaticity parameter ξ:

$$\xi = \frac{\tau_{coll}}{\tau_{nuc}} = \frac{a\Delta E}{\hbar v} \leq 1. \tag{5.4}$$

A classical treatment of the motion is valid as long as the excitation energy is smalled compared to the bombarding energy so that the trajectory is not significantly modified, *i.e* $\frac{\Delta E}{E} = 2\frac{\xi}{\eta} << 1$. This is automatically fulfilled when criterions 5.1 and 5.4 are met. If the motion is too slow ($\xi > 1$), the collision process becomes adiabatic and the probability of excitation is low. The excitation process is described by the time-dependent Schrödinger equation:

$$i\hbar\frac{\partial}{\partial t}|\psi(\overrightarrow{r},t)\rangle = \left\{H_0 + V[\overrightarrow{r}(t)]\right\}|\psi(\overrightarrow{r},t)\rangle, \tag{5.5}$$

where $|\psi(t)\rangle$ is the time-dependent state, H_0 is the free nucleus Hamiltonian, and $V[\overrightarrow{r}(t)]$ is the time-dependent Hamiltonian that arises from electromagnetic interaction. To solve the time-dependent Schrödinger Eq. 5.5 we represent $|\psi(\overrightarrow{r},t)\rangle$ as a linear combination of time-independent free nucleus wave functions $|\Phi(\overrightarrow{r})\rangle$, taken with time-dependent coefficients of the form:

$$|\psi(\overrightarrow{r},t)\rangle = \sum_n a_n(t)|\Phi_n(\overrightarrow{r})\rangle e^{-iE_n t/\hbar}, \tag{5.6}$$

with

$$H_0|\Phi_n(\overrightarrow{r})\rangle = E_n|\Phi_n(\overrightarrow{r})\rangle. \tag{5.7}$$

Substituting 5.6 in 5.5 gives:

$$i\hbar\sum_n \frac{da_n(t)}{dt}|\Phi_n(\overrightarrow{r})\rangle e^{-iE_n t/\hbar} = \sum_n a_n(t)V(t)|\Phi_n(\overrightarrow{r})\rangle e^{-iE_n t/\hbar}. \tag{5.8}$$

Taking into account orthonormality of the free nucleus wavefunctions $|\Phi_n(\overrightarrow{r})\rangle$, ($\langle\Phi_k|\Phi_n\rangle = \delta_{kn}$) gives:

$$\frac{da_k(t)}{dt} = -\frac{i}{\hbar}\sum_n a_n(t)\langle\Phi_k|V(t)|\Phi_n\rangle e^{it(E_k-E_n)/\hbar}. \tag{5.9}$$

To solve this system of coupled differential equations 5.9, one needs to know the initial and final conditions (corresponding to $t = -\infty$, $t = \infty$ respectively) and to expand the potential $V(t)$ into a multipole series [23]. The excitation of both projectile and target can be indepedently expressed from Eq. 5.5 as

$$i\hbar\frac{\partial}{\partial t}|\psi_{1,2}(\overrightarrow{r},t)\rangle = \left\{H^0_{1,2} + V_{1,2}[\overrightarrow{r}(t)]\right\}|\psi_{1,2}(\overrightarrow{r},t)\rangle, \tag{5.10}$$

where "1" labels the projectile and "2" the target. As mentioned above, the interaction potential $V(t)$ can be expanded into a multipole series:

$$V_{1,2}(t) = \sum_{\lambda=1}^{\infty}\sum_{\mu=-\lambda}^{\lambda}\frac{4\pi Z_{2,1}e}{2\lambda+1}(-1)^{\mu}S_{\lambda\mu}(t)\mathscr{M}_{1,2}(\lambda,-\mu) \tag{5.11}$$

where the functions $S_{\lambda\mu}$ and multipole moments $\mathscr{M}_{1,2}(\lambda,-\mu)$ are expressed for electric and magnetic excitations (Table 5.1). $Y_{\lambda\mu}(\theta,\phi)$ denotes standard normalized spherical harmonics. $\rho_{1,2}(\overrightarrow{r})$ and $\overrightarrow{j}_{1,2}(\overrightarrow{r})$ being spatial charge and current distributions of a free nucleus. Before the collision, the nucleus is assumed to be in the ground state, thus the initial condition is $a_k(-\infty) = \delta_{k0}$ where index 0 stands for the ground state. The nucleus after the collision is then described by the set of excitation amplitudes $a_k(t = \infty)$ (Eq. 5.9) defining excitation probabilities $P_k = |a_k|^2$. The coefficients a_k (amplitudes of the wave functions $\Phi_k(\overrightarrow{r})$) can be found by numerically integrating Eq. 5.9. Such numerical integration can be done by different programs including CLX [72, 73, 74] and GOSIA [75]. The reader is referred to the corresponding literature [72, 73, 74, 75] for more details concerning the numerical integration.

Function	Electric $E\lambda$	Magnetic $M\lambda$
$S_{\lambda\mu}(t)$	$\frac{Y_{\lambda\mu}(\theta(t),\phi(t))}{[r(t)]^{\lambda+1}}$	$\frac{1}{c\cdot\lambda}\frac{\frac{d\overrightarrow{r}}{dt}(\overrightarrow{r}\times\overrightarrow{\nabla})}{[r(t)]^{\lambda+1}}Y_{\lambda\mu}(\theta(t),\phi(t))$
$\mathscr{M}(\lambda,\mu)$	$\int\rho(\overrightarrow{r})r^{\lambda}Y_{\lambda\mu}(\theta,\phi)d^3\overrightarrow{r}$	$\frac{1}{c(\lambda+1)}\int r^{\lambda}\overrightarrow{j}(\overrightarrow{r})(\overrightarrow{r}\times\overrightarrow{\nabla})Y_{\lambda\mu}(\theta,\phi)d^3\overrightarrow{r}$

Table 5.1: List of the functions $S_{\lambda\mu}(t)$ and the multipole operators $\mathscr{M}$ for $E\lambda$ and $M\lambda$ excitations from [23].

5.3 Coulomb excitation cross sections

Once the amplitudes for COULEX are obtained, they can be used to calculate the COULEX cross sections. The probability for excitation from an initial state (index i) to the various final states (index f), irrespective of the orientation of the initial or final nuclear state, is given by:

$$P = P_{i\to f} = \frac{1}{2J_i+1}\sum_{M_i M_f}|a_k(M_i)|^2, \tag{5.12}$$

where J_i is the spin of the initial nuclear state and where M_i and M_f are the magnetic quantum numbers of the initial and final states. Since we have assumed that the trajectory of the particle is not appreciably affected by the excitation, the differential COULEX (CLX) cross section is given by,

$$\left(\frac{d\sigma}{d\Omega}\right)_{CLX} = P\left(\frac{d\sigma}{d\Omega}\right)_{Ruth} = P\frac{a^2}{4\sin^4(\frac{\theta_{CM}}{2})} \tag{5.13}$$

where P is the probability that the nucleus is excited in a collision (5.12) and $d\sigma/d\Omega|_{Ruth}$ corresponds to the Rutherford cross section (elastic scattering) in which the particle is scattered into the solid angle $d\Omega$, θ_{CM} is the scattering angle in the center-of-mass system (CM) (Fig. 5.1) and, a is half the distance of closest approach in a head-on collision, Z_1, Z_2 are the charge numbers of projectile and target respectively, m_0 is the reduced mass of the scattering problem, and v is the velocity of the projectile with respect to the target.

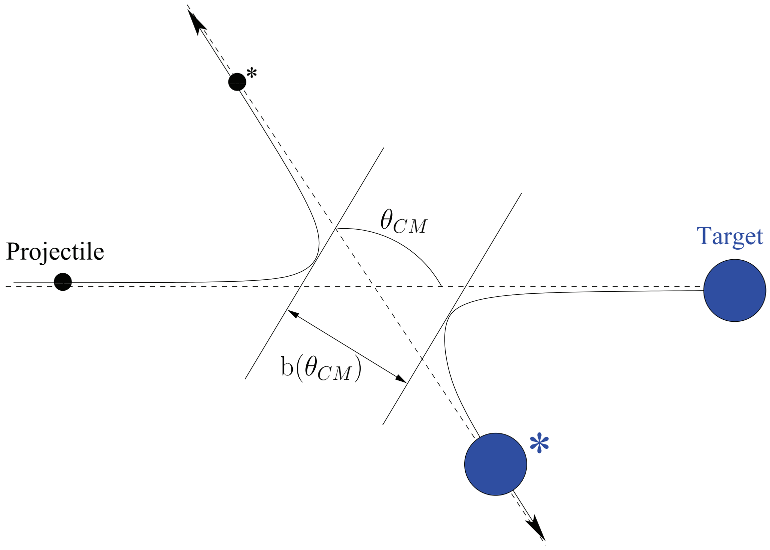

Figure 5.1: The scattering of the projectile off the target is shown in the center-of-mass system. The distance of closest approach as a function of θ_{CM} is given by [69] $b(\theta_{CM}) = a(1+1/\sin(\theta_{CM}/2))$. In a head-on collision $\theta_{CM} = 180°$ and $b = 2a$.

In general, the excitation cross section contains interfering terms from the sum over different excitation paths that correspond to multiple COULEX processes. The situation is considerably simplified in the one-step case where one excitation path predominates. This is the case, for instance, for the COULEX of one-quadrupole phonon states (e.g the

$2^+_{1,\mathrm{ms}}$ states) that are excited from the ground state in one-step $E2$-excitations. The general formula of the total cross section for a one-step $E\lambda$ COULEX process is calculated by integrating Eq. 5.13 over the whole solid angle and is given by

$$\sigma_{E\lambda} = \left(\frac{Z_1 e}{\hbar v}\right)^2 a^{-2} B(E\lambda; J_i \rightarrow J_f) f_{E\lambda}(\xi), \tag{5.14}$$

where $B(E\lambda; J_i \rightarrow J_f)$ is the reduced transition probability related to the nuclear matrix elements of the electric multipole operator $\mathscr{M}$ (see Table 5.1) by

$$B(E\lambda; J_i \rightarrow J_f) = \frac{1}{2J_i + 1} |\langle J_f || \mathscr{M}(E\lambda) || J_i \rangle|^2. \tag{5.15}$$

Eq. 5.14 shows that the one-step $E\lambda$ COULEX cross section is proportional to the reduced transition strength $B(E\lambda; J_i \rightarrow J_f)$. The cross section furthermore increases with decreasing excitation energy for a given transition matrix element. The kinematical function $f_{E\lambda}(\xi)$ are monotonically decreasing with increasing ξ, where ξ is given in Eq. 5.4, and ΔE is the excitation energy of the Coulomb excited state. Likewise, the total magnetic excitation cross section is given by

$$\sigma_{M\lambda} = \left(\frac{Z_1 e}{\hbar c}\right)^2 a^{-2\lambda+2} B(M\lambda; J_i \rightarrow J_f) f_{M\lambda}(\xi). \tag{5.16}$$

The functions $f_{E\lambda}(\xi)$ and $f_{M\lambda}(\xi)$ are plotted in [67]. The magnetic excitation cross section is reduced by a factor of $(v/c)^2$, compared to the electric excitation cross section. In the energy range considered in this work ($v/c \sim 6\%$), this factor is $\simeq 0.004$. Thus the magnetic excitation can be neglected. In our experiments we measure the one-step $E2$ excitation (for example of the $2^+_{1,\mathrm{ms}}$ state) from the ground state expressed as

$$\boxed{\sigma_{E2} = \left(\frac{Z_1 e}{\hbar v}\right)^2 a^{-2} B(E2; 0^+_1 \rightarrow 2^+) f_{E\lambda}(\xi)} \tag{5.17}$$

to finally derive the electromagnetic strength $B(E2; 0^+_1 \rightarrow 2^+)$. Another important second-order effect is that of a double $E2$ excitation leading to a final state which cannot be reached directly from the ground state by an $E2$ excitation. The order of magnitude of the cross section for such a double excitation is given in [67, 76] by

$$\sigma_{E2,E2} \approx \frac{1}{4} a^{-2} \sigma_{E2}(I_i \rightarrow I_z) \sigma_{E2}(I_z \rightarrow I_f). \tag{5.18}$$

For the specific case $I_i = 0$, $I_z = 2$, $I_f = 4$, and for $\xi_1 = \xi_2 = \xi = 0$ gives

$$\sigma_{E2,E2} = 0.0218 \left(\frac{Z_2 e}{\hbar v}\right)^4 a^{-6} B(E2; 0^+_1 \rightarrow 2^+) B(E2; 2^+ \rightarrow 4^+). \tag{5.19}$$

In order to calculate the absolute electromagnetic transition strengths, the multistep COULEX code CLX has been used. This is briefly outlined below.

5.4 Coulomb excitation code: CLX

The Coulomb excitation code “CLX” written by H. Ower [72, 74] is based on the multiple Coulomb excitation program developed by Winther and de Boer [77]. It calculates the excitation cross sections according to the first-order perturbation theory of Ref. [67] and puts-out the Coulomb excitation amplitudes given in Eq. 5.9. The calculation process is explained in detail in Ref. [77]. The coupled differential equations for the COULEX amplitudes (Eq. 5.9) can be transformed by the change of variables and symmetry relations. Then, a fourth-order Runge-Kutta method is used for the integration to find the initial values that are input into an Adams-Moulton predictor-corrector method. Input parameters to the code involve:

- (Z,A) for beam and target nuclei
- the “average” beam energy
- angular range of the CM scattering angles

- all spin and parity quantum numbers and excitation energies of states involved in the calculations
- all matrix elements connecting the populated states.

CLX outputs the differential cross sections at the specified angular mesh points and the excitation cross sections to each nuclear level. An example of input file is given in Appendix A.

6 Experiment, Data Analysis

In the first part of this chapter, a general description of the experiment set up will be done. Then, the general procedure for the data analysis will be explained in details. The results are given in the last section (section 7).

6.1 Experiment

The Coulomb excitation experiments were performed at the ATLAS (Argonne Tandem Linac Accelerator System) facility in ANL (Argonne National Laboratory) located in Argonne (Illinois, USA). The facility hosts a superconducting linear accelerator ATLAS combined to the high-purity germanium detector array Gammasphere.

6.1.1 ATLAS facility

One of the two injector accelerators, either a 9 Million Volt (MV) electrostatic tandem Van de Graff, or a new 12-MV low-velocity linac and electron cyclotron resonance (ECR) ion source called the Positive Ion Injector provide the beam requested. It is then sent on to the 20-MV booster linac, and then finally into the 20-MV ATLAS linac section. High precision heavy-ion beams ranging over all possible elements, from hydrogen to uranium, can be accelerated to energies as high as 17 MeV per nucleon and delivered to one of three experimental target areas as shown in Fig. 6.1.

Ions are accelerated through a strong electric field (800 000 V) applied inside of each of the superconducting niobium resonators cooled down to liquid helium temperatures. This $\overrightarrow{E}$ field is varying rapidly in time ($\approx 10^8$ Hz) which gives the acceleration structure to the linac. The beam was pulsed with a frequency of 12 MHz and sent to the different experimental areas. Xenon isotopes have been accelerated to an energy corresponding to $\approx$85% of the Coulomb barrier ($\sim$ 3 MeV/A) onto a $\approx$1.0 mg/cm^2 natural carbon target. The intensity of the beam was $\approx$1 pnA. Details for energies and duration of experiment for each respective Xe isotope is listed on Table 6.1.

6.1.2 Gammasphere array

Once the ions are accelerated and impinging on the ^{12}C target, they will be Coulomb excited inside the target and their emmited γ-rays (deexcitation) are detected in the Gammasphere array. The reason for choosing carbon as a target is two-fold. First, the first excited state of ^{12}C, which has a 98.9% natural abundance, lies above 4.4 MeV and therefore the probability to excite it is small in comparison with the nuclei of interest where the 2_1^+ state lies between 300-800 keV. Moreover, due to the low natural abundance of ^{13}C (1.1%) and the high excitation energy of its first excited state (3.1 MeV), it was assumed that there was no contribution of ^{13}C in the spectra. The second reason for the choice of carbon is its low atomic number $Z = 6$, favoring the one-step Coulomb excitation process (see formula for double excitation in Eq. 5.19), since the focus of the experiment was to study low-spin collective states, in particularly the 2^+ states polulated by a one-step $E2$ excitation.

The most important properties of a γ-ray detector array are energy resolution, efficiency and peak-to-background ratio (P/T). The current arrays use large volume Ge detectors to achieve good energy resolution and high peak efficiency. In

Isotope	Energy MeV	Beam current pnA	Target	Thickness mg/cm^2	Time Exp. h
^{124}Xe	394	$\approx$1	^{12}C	1.0	12
^{126}Xe	399	$\approx$1	^{12}C	1.0	29
^{128}Xe	404	$\approx$1	^{12}C	1.0	23
^{130}Xe	409	$\approx$1	^{12}C	1.0	24
^{132}Xe	414	$\approx$1	^{12}C	1.0	13
^{134}Xe	435	$\approx$1	^{12}C	1.0	38

Table 6.1: Parameters of the different experiments for each xenon isotope.

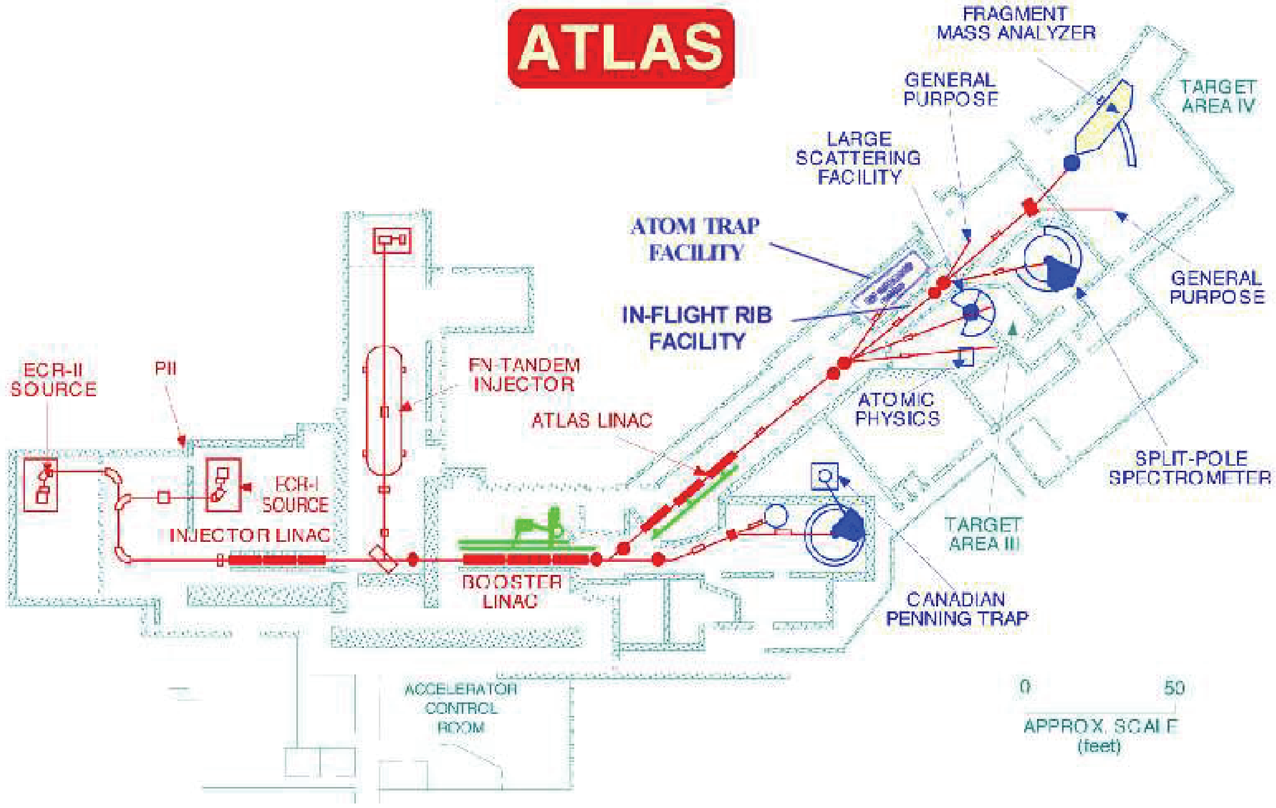

Figure 6.1: Map of the Atlas facility and the different experimental areas. Gammasphere is located in the Target area IV (blue spot before the Fragment Mass Analyser). Picture taken from Ref. [78].

addition, the detectors are surrounded by BGO (Bismuth Germanate) Compton suppressors for improving the peak-to-total ratio. The Gammasphere is an array of 110 high-purity Ge (HPGe) detectors with Compton suppression shields arranged in 17 rings. Each ring is placed at a certain polar angle θ from the beam axis. Details for the array can be found in Refs [79, 80, 81]. A drawing of the geometry of Gammasphere is shown in Fig. 6.2. The detectors are arranged symmetrically in roughly a sphere with the faces of the detectors forming a 122-element polyhedron. The polyhedron consists of 110 hexagons, which are occupied by the detectors and 12 pentagons, which are openings in the polyhedron for target chamber mounts and auxiliary detectors. A schematic diagram of the inner structure of the Ge detectors is shown in Fig. 6.3. All of the Ge detectors cover 46% of the total solid angle. Each of the detectors have an efficiency of 82% at 1.33 MeV with respect to the NaI standard and the entire array has a total photopeak efficiency of 9.9% (see Table 6.2). For a better ratio of full-energy to partial-energy events (called the peak-to-total, or P/T ratio), the Ge detectors are surrounded by a dense scintillator (BGO) which detects gamma rays Compton-scattered out of the Ge crystal and then electronically suppresses the partial-energy pulse left in the Ge detector. This results in an improvement in the P/T ratio for a 1.3 MeV gamma ray from about 0.25 for the bare crystal to about 0.6 when suppressed. A unique element of the Gammasphere detectors is the BGO backplug (Fig. 6.3). This BGO element is used for Compton supression is especially useful in that the Compton scattering cross section is large at angles close to 0° and 180°. The γ-rays from the target are also collimated with Hevimet, a dense metal alloy, which also shields the BGO element in the BGO Suppressor shield (Fig. 6.3). Two spectra illustrating the effect of Compton supression is shown in Fig. 6.4. The Compton unsuppressed spectrum shows the large Compton background that comes from the γ-rays that deposit only a portion of their full energy in the Ge crystal. The Compton suppressed spectrum shows a much lower Compton background that results from vetoing Compton scattered γ-rays detected in one of the BGO elements.

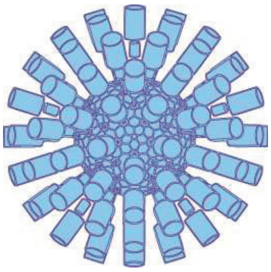

Figure 6.2: General view of the Gammasphere array, composed of 110 HPGe detectors arranged spherically. Figure taken from Ref. [83].

Figure 6.3: A schematic diagram of Gammasphere HPGe detectors. It consists of a HPGe crystal, BGO anti-Compton elements, photomultipliers for the BGO elements, Hevimet collimaters, detector electronics, and a liquid nitrogen dewar, which stores liquid nitrogen for cooling the HPGe crystal. Figure taken from Ref. [83].

	Gammasphere	Agata
Number of detectors	110	180
	40 unsegmented	
	70 segmented (2 segments each crystal)	180 (36 segments each crystal)
Target to Ge distance	25.25 cm	17 cm
Total Ge solid angle	46% 4π	78% 4π
Total Peak efficiency (1.33 MeV)	9.9%	50%
P/T (1.33 MeV)	0.6	0.59
Energy resolution (1.33 MeV)	2.5 keV (FHWM)	2.06 keV (FHWM)

Table 6.2: Characteristics parameters of Gammasphere compared with the next generation of γ-detector array AGATA. Datas for Gammasphere and Agata are taken from [81] and [82], respectively.

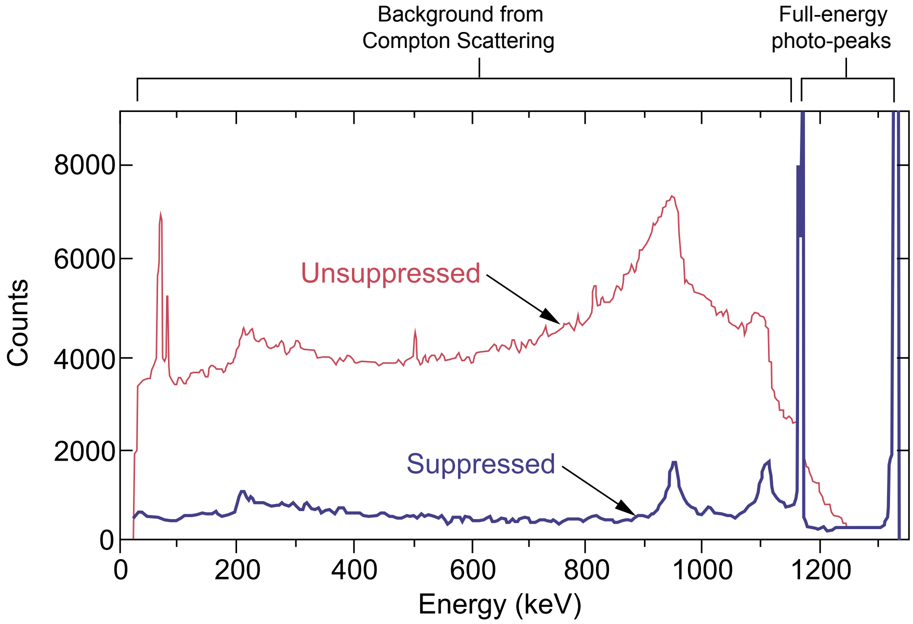

Figure 6.4: Two energy spectra are shown for data obtained from a ^{60}Co source with (blue spectrum) and without Compton suppression (red spectrum). Figure taken from Ref. [83].

6.2 Data Analysis

6.2.1 Efficiency calibration

Many textbooks deal with the interaction of γ-rays with matter. One of the best sources of information is [84]. In short, there are three ways that a γ-ray may interact with the matter: photoelectric effect, Compton Scattering and pair production. However, the occurence of these processes depends strongly on the energy of the incident photon as it is shown on Fig. 7.10 in Ref. [85]. Therefore the probability for a 0.1 MeV incident photon to be absorbed in the Ge crystal is not the same as a 1 MeV photon. This difference has to be taken into account for the analysis. This is called the efficiency calibration.
The efficiency calibration has been done using ^{152}Eu and ^{56}Co sources mounted at the position of the beam spot. The use of both sources provided γ rays with energies covering the energy range of interest, *i.e* from 121 keV to 2.6 MeV. Since the detectors are arranged in 17 rings (17 θ angles), it is usefull to do the efficiency calibration for each ring (if later any angular distribution has to be measured) in addition of the global efficiency over all Ge detectors. As an example, the relative efficiency measured for the ring 9 (θ=90°) is shown in Fig. 6.5. The experimental data have been fitted with the function

$$\epsilon(E) = exp\left(\left\{\left[a + b\times\ln(\frac{E}{100}) + c\times[ln(\frac{E}{100})]^2\right]^{-g} + \left[d + e\times ln(\frac{E}{1000}) + f\times[ln(\frac{E}{1000})]^2\right]^{-g}\right\}^{-1/g}\right), \tag{6.1}$$

where E is the Energy of a γ ray in keV. The error of the relative efficiency has been calculated from the error propagation formula [86] (see Appendix B).

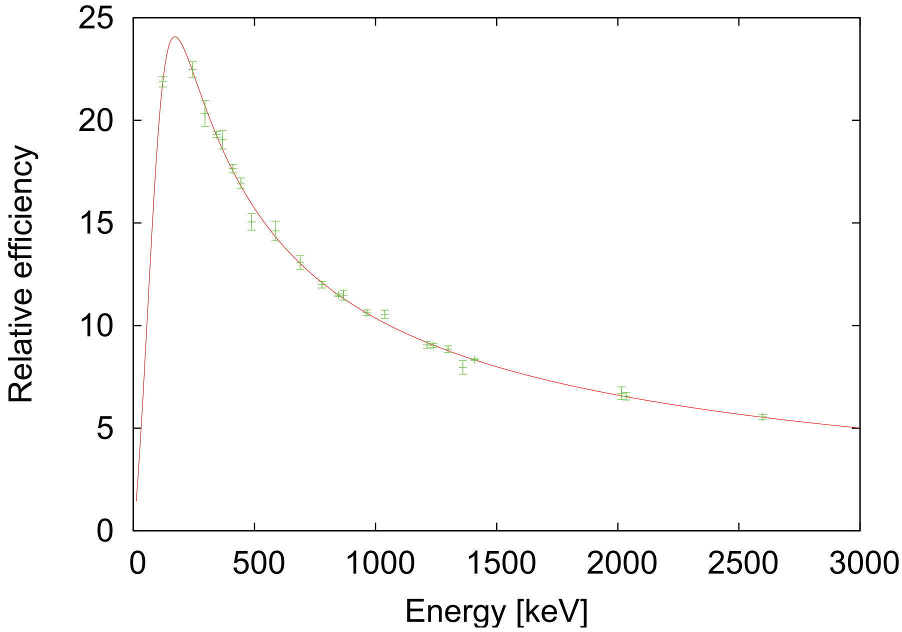

Figure 6.5: Relative efficiency from the ^{152}Eu and ^{56}Co sources measured for the ring 9 (θ=90°) and fitted by the function of Eq. 6.1 with the following parameters: a=3.43(5), b=3.83(18), c=0, d=2.342(5), e=-0.636(5), f=-0.023(3), g=3.19(5).

6.2.2 Doppler correction

The Xe ions impinging on the 1.0 mg/cm^2 carbon target loose ≈40 MeV and recoil in vacuum with approximately 6-7 % of the speed of light. Therefore the emitted γ rays are Doppler shifted. This Doppler shift is given by the relativistic Doppler formula:

$$E(\theta) = E_0\frac{1+\beta\cos\theta}{\sqrt{1-\beta^2}}, \tag{6.2}$$

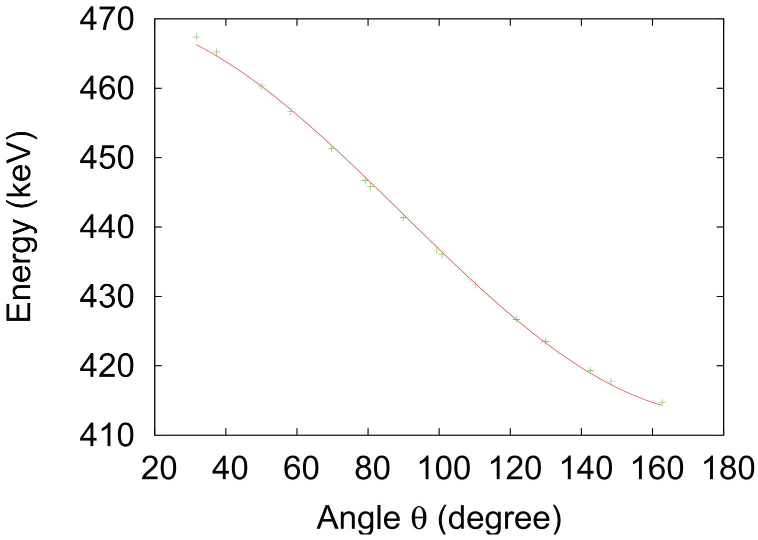

Figure 6.6: Measured energy of the $2_1^+ \rightarrow 0_1^+$ transition (unshifted energy 442.9 keV) plotted as a function of θ for ^{128}Xe (θ defined in text). The experimental points have been fitted via Eq. 6.2 and with β=0.065(2)%.

where E_0 is the unshifted energy, θ is the angle between the flying emitting Xe nucleus and the detector where the γ ray fired (in the Lab frame), and $\beta = v/c$. Due to the inverse kinematics of our reaction, the flying Xe nucleus was emitted in a forward cone (± 5°). The θ angle between the flying nucleus and its emitted γ ray was then approximated by the angle between the beam axis and the detector where the γ ray fired.

At Gammasphere, the position of the Germanium detectors are characterized by their (θ,ϕ) angles (Appendix C). The detectors are arranged into 17 rings. To each ring corresponds a θ value. The shifted energy position of the first 2^+ state has then been plotted for each ring (*i.e* for each 17 θ values). This is shown in Fig. 6.6. The experimental data have been fitted via equation 6.2.

Eq. 6.2 depends on three parameters (E$_0$, β, θ), which means there are three primary factors that contribute to the energy resolution (ΔE) of the Doppler corrected γ-ray spectrum. The uncertainty in β due to the slowing down of the projectile in the target ($\Delta\beta$), the uncertainty in the emission angle of the γ ray due to the finite opening angle of the γ-ray detector combined with the uncertainty in the angle of the scattered particle ($\Delta\theta$), and the intrinsic energy resolution of the Ge detector ($\Delta E_{0,det}$). The total energy resolution is then given by [88]:

$$\left(\frac{\Delta E}{E}\right)^2 = \left(\frac{\beta\sin\theta}{1-\beta\cos\theta}\right)^2 (\Delta\theta)^2 + \left(\frac{\beta-\cos\theta}{(1-\beta^2)(1-\beta\cos\theta)}\right)^2 (\Delta\beta)^2 + \left(\frac{\Delta E_{0,det}}{E}\right)^2. \tag{6.3}$$

This uncertainty from Eq. 6.3 is called the Doppler broadening. It can be easily calculated for our experiment at Gammasphere where $\Delta\beta$=0.002, $\Delta\theta$=14.8°, and $\frac{\Delta E_{0,det}}{E}$=0.2%. Table 6.3 gives some ΔE values for detectors from the ring 9 (θ=90°, β=0.065).

E [MeV]	ΔE [keV]
1	16.9
2	33.8
3	50.7

Table 6.3: ΔE values for different energies calculated from Eq. 6.3 for $\beta(\Delta\beta)$=0.065(2), θ=90°, $\Delta\theta$=14.8°, and $\frac{\Delta E_{0,det}}{E}$=0.2%.

6.2.3 Sorting

The Multi Instance Data Acquisition System (MIDAS) program using the MTSort language was used to sort the raw data into spectra and matrices. MIDAS as well as the guidelines for its installation can be downloaded here: [91]. The documentation about the MTSort language can be found here: [92]. In our experiments, the trigger used was defined by one γ ray firing in one of the Ge detectors from the Gammasphere array (the so called "pre-trigger"). Since this γ can result from the Compton scattering ("dirty" γ) and meantime suppressed by the BGO, an other trigger was defined (the so called "MASTER trigger") corresponding to the firing of a "clean" γ in the Gammasphere. This MASTER-trigger starts after an adjustable delay (≈500 ns) after the pretrigger as shown in Fig. 6.7. Finally, the stop signal was defined by the next pulse of the Radiofrequency (RF). This time, between the pre-trigger and the next pulse of the RF is defined as TAC2. It has been used to set our time gates (beam and background gates) in order to separate the "bad" gammas coming from the background radiation and the "good" gammas coming from the Coulex excitation reaction. This will be further explained in the next part. The experimental raw data from Gammasphere were sorted offline to produce the final spectra and matrices. The events were defined as the detection of one or more γ-rays not Compton suppressed in any of the detectors (multiplicity 1). γ-rays fold higher than 1 (multiplicity > 1) have been sorted into a E_γ-E_γ matrix. The total number of events (multiplicity 1), as well as the events with multiplicity 2 or higher are listed on Table 6.4.

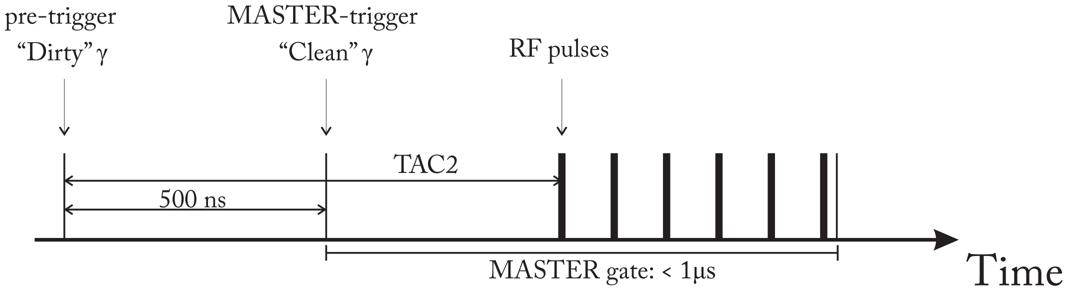

Figure 6.7: Schematic representation of the different triggers used at Gammasphere as well as TAC2, time between the pre-trigger and the next pulse of the RF. The Master gate is a fixed interval of time which can also be used as the stop signal (end of the Master gate).

Isotope	Number events	
	Multiplicity 1	Multiplicity > 1
^{124}Xe	5.1×10^{8}	2.04×10^{7}
^{126}Xe	1.3×10^{9}	1.8×10^{7}
^{128}Xe	1.0×10^{9}	1.7×10^{7}
^{130}Xe	9.2×10^{8}	8.4×10^{6}
^{132}Xe	4.7×10^{8}	6.2×10^{6}
^{134}Xe	8.4×10^{8}	2.6×10^{6}

Table 6.4: Total number of events with multiplicity 1 (middle) or higher (right) for the different Xe isotopes. The data for ^{124}Xe and ^{134}Xe are taken from [89] and [90] respectively.

6.2.4 Room background subtraction

In Fig. 6.8 is shown a typical TAC2 time spectrum. The peak corresponds to the prompt gammas observed after the Coulomb excitation reaction. By setting the "beam gate", we select the gammas coming from the COULEX reaction and thus create the so-called "in-beam" spectrum. Unfortunately this "in-beam" spectrum is still contaminated by the natural room background which also needs to be subtracted. By setting the "background gate", we select only the gammas coming from the background and create the "off-beam" spectrum. Finally, we produce a background free spectrum by differentiating the "in-beam" spectrum and the "off-beam" spectrum scaled to eliminate the 1461-keV from the decay of natural ^{40}K line. The background subtracted spectrum is then obtained by

$$N_{sub}(E) = N_{beam}(E) - K \times N_{back}(E), \tag{6.4}$$

where the normalization factor K is expressed by the 1461-keV intensities ratio: $K = I_{beam}(1461\text{ keV})/I_{back}(1461\text{ keV})$.

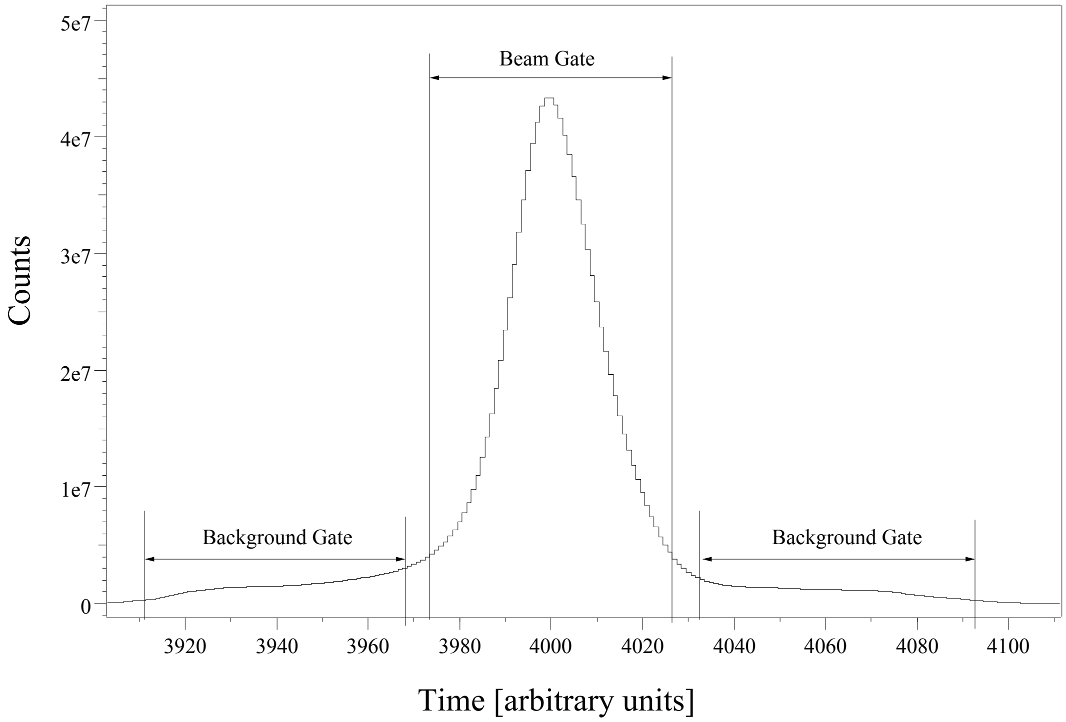

Figure 6.8: Time spectrum (TAC2) with its corresponding beam and background gates.

6.2.5 Calculation of cross sections

- **Energy loss**

Charged ions penetrating into matter lose their energy by interaction with charges in the material. The Coulomb excitation cross sections are very sensitive to the energy of the incoming particle and this energy loss has to be taken into account in the CLX code. In our case the average beam energy ($\overline{E}$ input in the CLX code, see section 5.4) is calculated by subtracting the initial beam energy (E_0) with the integrated energy loss over the target of thickness $\rho = 1.0$ mg/cm^2:

$$\overline{E} = E_0 - \int_0^{1.0} \frac{dE}{d\rho} d\rho. \tag{6.5}$$

In our experiments (Table 6.1), the energy loss is about 40 MeV.

- **Relative measurement**

The number of inelastically scattered particles (beam or target nuclei) in a COULEX experiment is a measure for the excitation probability to a state $|n\rangle$ (P$_n$) (see Eq. 5.12). Experimentally, the number of inelastically scattered beam or target nuclei may be determined from the γ-decay of the state $|n\rangle$ in the considered nucleus. In this work, the de-excitation γ rays following Coulomb excitation of the beam were detected by the Germanium Gamma Detector Array Gammasphere (see section 6.1.2). For example, the number of detected $2_1^+ \rightarrow 0_1^+$ de-excitation γ rays associated with the de-excitation of the 2_1^+ state of the incoming beam particles (even-even $^{124-134}$Xe) is given by

$$N_\gamma^{Xe}(2_1^+ \rightarrow 0_1^+) = \epsilon(E) \cdot \sigma_{E2,Xe} \cdot \frac{\rho N_A}{A} I_{Xe}, \tag{6.6}$$

where ϵ is the efficiency of Gammasphere at the energy of the transition $2_1^+ \rightarrow 0_1^+$, $\sigma_{E2,Xe}$ is the total one-step $E2$ COULEX cross section for the 2_1^+ state, ρ is the target thickness in mg/cm^2, N_A is the Avogadro number, A the target mass number and I_{Xe} the total incoming beam intensity. However, Eq. 6.7 gives us the number of γ rays emitted only from the one step $E2$ excitation assuming no feeding from other states lying at higher energies. This feeding has to be taken into account. Therefore we measure experimentally the yields of each state (Y_i), *i.e* by adding and subtracting the γ-ray intensities (I$_{\gamma_i}$) according to the known level schemes to account for the population of a state from a γ transition from a higher-lying state. Thus, these yields correspond exactly to the population of the excited state $|i\rangle$ coming exclusively from the one- or multistep Coulomb excitation from lower lying states (for 2^+ states, mainly from a one-step excitation from the ground state). For example:

$$Y_{2_1^+} = \frac{I_\gamma(2_1^+ \to 0_1^+)}{\epsilon[E_\gamma(2_1^+ \to 0_1^+)]} - \sum_{i=feeding} \frac{I_{\gamma i}}{\epsilon(E_{\gamma i})} = \sigma_{E2,Xe} \cdot \frac{\rho N_A}{A} I_{Xe}. \tag{6.7}$$

In oder to avoid some systematical uncertainties (for example due to the not accurately known beam intensity I_{Xe}), the total inelastic cross sections should therefore be measured relative to a known inelastic cross section in the same experiment. In our experiments, we used the one from the $2_1^+ \to 0_1^+$ decay with the known $B(E2; 2_1^+ \to 0_1^+)$ value taken from [94]. In this sense, we obtain for the $2^+_{1,\mathrm{ms}}$ state populated mainly by a one-step $E2$ Coulomb excitation relative to the yields of the 2_1^+ state

$$\frac{Y_{2^+_{1,\mathrm{ms}}}}{Y_{2_1^+}} \simeq \frac{\sigma_{E2}(2^+_{1,\mathrm{ms}})}{\sigma_{E2}(2_1^+)}. \tag{6.8}$$

The left part of Eq. 6.8 is our observable from the experiment and the right part of Eq. 6.8 is calculated by the multiple Coulomb excitation code CLX. As explained in section 5.4, a set of matrix elements was to input in the program CLX and the corresponding cross sections were calculated. These cross sections were then compared with the relative yields from our experiment (Eq. 6.8) and then changed accordingly to reproduce the experimental yields using the known branching ratios and multipole mixing ratios to constrain the ratio of matrix elements. Once the matrix elements are known, the corresponding electromagnetic transition strengths are derived according to Eq. 5.15.
One of the unknown parameters in the calculation was determining the relative phase of the matrix elements. The values of the matrix elements can be either positive or negative without changing the value of the corresponding electromagnetic transition strength. Use of different phases can modify the cross section due to interference effects. Therefore the relative phases must be “quantum mechanically coherent” as outlined by Wu *et al.* [95]. The coherence to quantum mechanics was assumed by a comparison to an interacting boson model calculation (see section 7). The other unknown parameters were the quadrupole moments of excited states. They were allowed to vary between the extreme rotational limits adding uncertainties to the transitional matrix elements of about 5% on average.

6.2.6 Gamma angular distribution

As mentioned previously in this section, the Ge detectors of Gammasphere are arranged in 17 rings (see Appendix C). This enables us to measure the intensity of a certain line for 17 different θ angles (if enough statistics available). The direction of the γ-ray emission depends on the radiation multipolarity $\pi\lambda$ and on the aligment of the state which has been populated (relative population of the M magnetic substates). Thus, it is possible to measure the multipole mixing ratio δ from a mixed $E2$,$M1$ transition (*e.g* $2_i^+ \to 2_1^+$) by measuring the two corresponding angular distributions (*i.e* $2_i^+ \to 2_1^+$ and $2_i^+ \to 0_1^+$). This will be explained in details in the next part. However, some relativistic effects need to be accounted for.

- **Relativistic effects: Lorentz boost correction**

The angle between the beam axis and the direction of emission of the photon is affected if the nucleus is in motion rather than at rest. The relativistic velocity addition formulae can be used to show that the angles of emission in the laboratory, $(\theta_{lab}\ , \phi_{lab})$, are related to those in the rest frame of the nucleus, $(\theta_{nuc}\ , \phi_{nuc})$, by the expressions [93]

$$\cos\theta_{lab} = \frac{\cos\theta_{nuc} + \beta}{1 + \beta\cos\theta_{nuc}} \tag{6.9}$$

$$\phi_{lab} = \phi_{nuc} \tag{6.10}$$

or,

$$\cos\theta_{nuc} = \frac{\cos\theta_{lab} - \beta}{1 - \beta\cos\theta_{lab}} \tag{6.11}$$

$$\phi_{lab} = \phi_{nuc} \tag{6.12}$$

where $\beta = v/c$ is the recoil velocity of the nucleus. It follows that an element of solid angle in the rest frame is related to an element of solid angle in the laboratory frame by

$$d\Omega_{nuc} = \frac{(1+\beta\cos\theta_{nuc})^2}{1-\beta^2} d\Omega_{lab}. \tag{6.13}$$

Since the γ-ray flux emitted into 4π of solid angle is conserved, *i.e.*

$$\int_{4\pi} W_{nuc}(\theta_{nuc}) d\Omega_{nuc} = \int_{4\pi} W_{lab}(\theta_{lab}) d\Omega_{lab}, \tag{6.14}$$

one obtains,

$$W_{nuc}(\theta_{nuc}) = W_{lab}(\theta_{lab}) \times \frac{d\Omega_{lab}}{d\Omega_{nuc}} = W_{lab}(\theta_{lab}) \times \frac{1-\beta^2}{(1+\beta\cos\theta_{nuc})^2} \tag{6.15}$$

where $\mathrm{W}_{lab}\theta_{lab})$ [$\mathrm{W}_{nuc}(\theta_{nuc})$] is the angular distribution in the lab frame [nuclear frame].

- **Multipole mixing ratio δ**

The multipole mixing ratio δ is usually defined by using the phase convention of Krane, Steffen and Wheeler [98, 99]

$$\delta = \frac{< J_f || \overrightarrow{j}_N \overrightarrow{A}_2^{(E)} || J_i >}{< J_f || \overrightarrow{j}_N \overrightarrow{A}_1^{(M)} || J_i >} = \frac{\sqrt{3}}{10} \frac{E_\gamma}{\hbar c} \frac{< J_f || E2 || J_i >_{BM}}{< J_f || M1 || J_i >_{BM}}. \tag{6.16}$$

$\overrightarrow{j}_N$ is the nuclear current operator and $\overrightarrow{A}_L^{(\pi)}$ are the electromagnetic multipole fields operators. The second part in Eq. 6.16 is the relation using the transition matrix elements of the corresponding $\pi\lambda$ operators as defined in the Bohr and Mottelson model [23]. Another useful definition is also given for δ^2 by

$$\delta^2 = \frac{\Gamma_{1,E2}}{\Gamma_{1,M1}} = \frac{c_{E2} E_1 (MeV)^5 B(E2; J \to J_f)}{c_{M1} E_1 (MeV)^3 B(M1; J \to J_f)}, \tag{6.17}$$

where $\Gamma_{f,\pi\lambda}$ is the natural linewidth of the $\pi\lambda$ electromagnetic radiation and is expressed as

$$\Gamma_{f,\pi\lambda} = 8\pi \frac{\lambda+1}{\lambda[(2\lambda+1)!!]^2} \left(\frac{E_\gamma}{\hbar c}\right)^{2\lambda+1} B(\pi\lambda; J \to J_f), \tag{6.18}$$

c_{E2}=8.0638146 meV/$10^{-3}\mathrm{e}^2\mathrm{fm}^2$, c_{M1}=11.574 meV/μ_N^2 and B($\pi\lambda$; J → J_f) is the reduced $\pi\lambda$ electromagnetic transition strength. The knowing of δ enables us to deduce $B(M1; J \to J_f)$ (which is the relevant signature of the $2^+_{1,ms}$ one-quadrupole Mixed-Symmetry State) after having calculated the $B(E2; J \to J_f)$ via the Coulex Analyis (see section 6.2.5). A typical decay scheme of a 2^+ state is shown in Fig. 6.9.

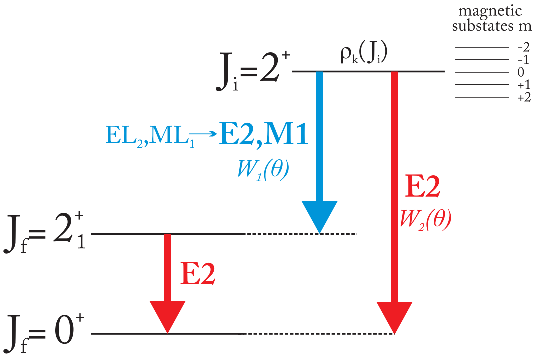

Figure 6.9: Typical decay scheme of a 2^+ state: through a mixed ($E2$,$M1$) transition to 2^+_1 and through a pure $E2$ transition to the ground state 0^+.

After a state has been populated via the Coulomb excitation reaction, its degree of alignment possessing spin J is specified by population parameters $\mathrm{P}_M(J)$ and quantified by the so called statistical tensors $\rho_k(J)$ [96], which are related to the relative population of M submagnetic states $\mathrm{P}_M(J)$ by

$$\rho_k(J) = (2J+1)^{1/2} \sum_M (-1)^{J-M} < JMJ-M|k0 > P_M(J) \tag{6.19}$$

where $< JMJ-M|k0 >$ are Clebsch-Gordan coefficients. Usually $\mathrm{P}_M(J)$ is a Gaussian distribution of the form

$$P_M(J) = \frac{e^{-\frac{M^2}{2\sigma^2}}}{\sum\limits_{M'=-J}^{J} e^{-\frac{M'^2}{2\sigma^2}}}. \tag{6.20}$$

If the M substates are non-uniformly populated, it gives rise to an observed anisotropic distribution of radiation. For an aligned state $[\mathrm{P}_M(J)=\mathrm{P}_{-M}(J)]$, $\rho_k(J)$ vanishes unless k is even. The angular distribution function for the general case $J_i \rightarrow J_f$ can be written as a function of the Legendre Polynomes $\mathrm{P}_k(\cos\theta)$ by

$$W(\theta) = A_0 + A_2 P_2(\cos\theta) + A_4 P_4(\cos\theta) = A_0[1 + a_2 P_2(\cos\theta) + a_4 P_4(\cos\theta)], \tag{6.21}$$

with the coefficients a_k expressed as

$$a_k(J_i L_1 L_2 J_f) = \frac{A_k(J_i L_1 L_2 J_f)}{A_0} = \rho_k(J) \frac{1}{1+\delta^2} \left[F_k(J_f L_1 L_1 J_f) + 2\delta F_k(J_f L_1 L_2 J_i) + \delta^2 F_k(J_f L_2 L_2 J_i) \right], \tag{6.22}$$

where

$$F_k(J_f L_1 L_2 J_i) = (-1)^{J_f - J_i - 1} \left[(2L_1+1)(2L_2+1)(2J_i+1) \right]^{1/2} \times < L_1 1 L_2 -1|k0 > W(J_i J_i L_1 L_2; k J_f). \tag{6.23}$$

$< L_1 1 L_2 - 1|k0 >$ are Clebsch-Gordan coefficients and W are Racah coefficients. Their definitions and expressions can be found in [97]. L_1, L_2 are the angular momenta of a mixed transition from $J_i \rightarrow J_f$. From the coefficients A_k of the angular distribution $W_2(\theta)$ (Fig. 6.9) corresponding to a pure $E2$ transition, we can deduce the alignment $\rho_k(J_i)$ of the excited state J_i (Eq. 6.22 with $\delta = 0$). And from the coefficients A_k of the angular distribution $W_1(\theta)$ and the knowing of $\rho_k(J_i)$, we can then deduce the value of δ (Eq. 6.22). The coefficients $F_k(J_f L_1 L_2 J_i)$ are tabulated in [96]. The observed angular distributions for the first and second 2^+ of ^{126,128,130,132}Xe are plotted on Figs. 6.10, 6.11, 6.12, 6.13, respectively. The resulting angular distribution ellipses for $2^+_2 \rightarrow 2^+_1$ transitions of ^{126,128,130}Xe calculated with the orientation resulting from $a_2 = A_2/A_0$ and $a_4 = A_4/A_0$ coefficients for the $2^+_2 \rightarrow 0^+_1$ transitions are shown in Fig. 6.14. The measured values of the mixing ratio δ for these transitions are listed in Table 6.5.

The measured values of δ in ^{134}Xe is given in [90]. In ^{124}Xe no δ value could have been measured. In ^{126,128}Xe, the measured δ values are in agreement with the previously known values (see Table 6.5). In ^{130}Xe our measured value is in contradiction with the value reported in [136]. This contradiction or in general the discrepancies observed in ^{126,128}Xe with the previously measured δ values can be explained by the “flatness” of our angular distributions. This unexpected “isotropy” is due to the fluctuating atomic hyperfine fields which causes the reorientation of the nuclear states. This turns into an attenuation of the angular distribution of the γ rays. This effect is known as the nuclear deorientation effect. This effect is the basic principle of the Recoil in vacuum method (RIV).

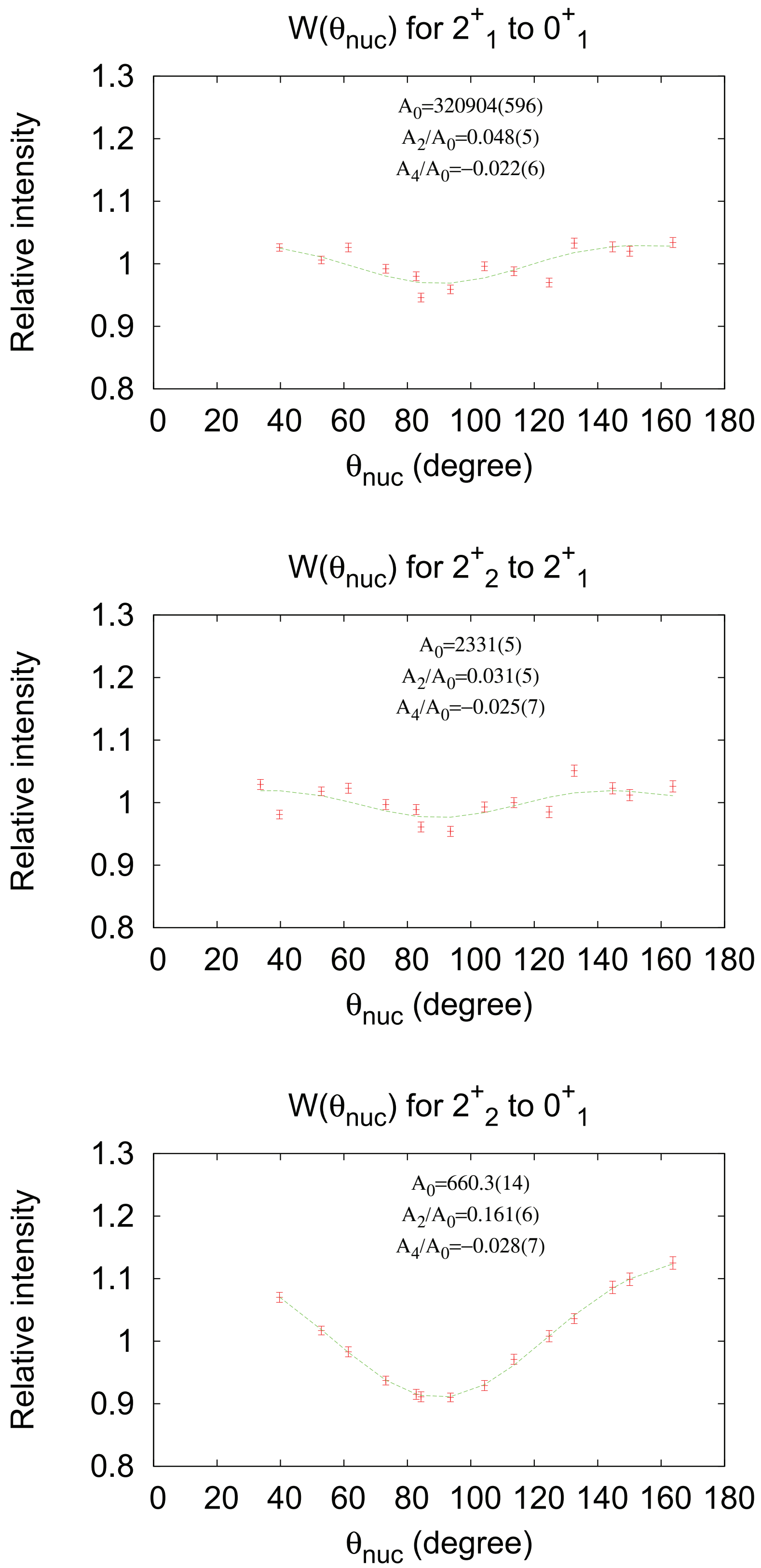

Figure 6.10: Angular distributions from the 2^+_1 and 2^+_2 states in ^{126}Xe.

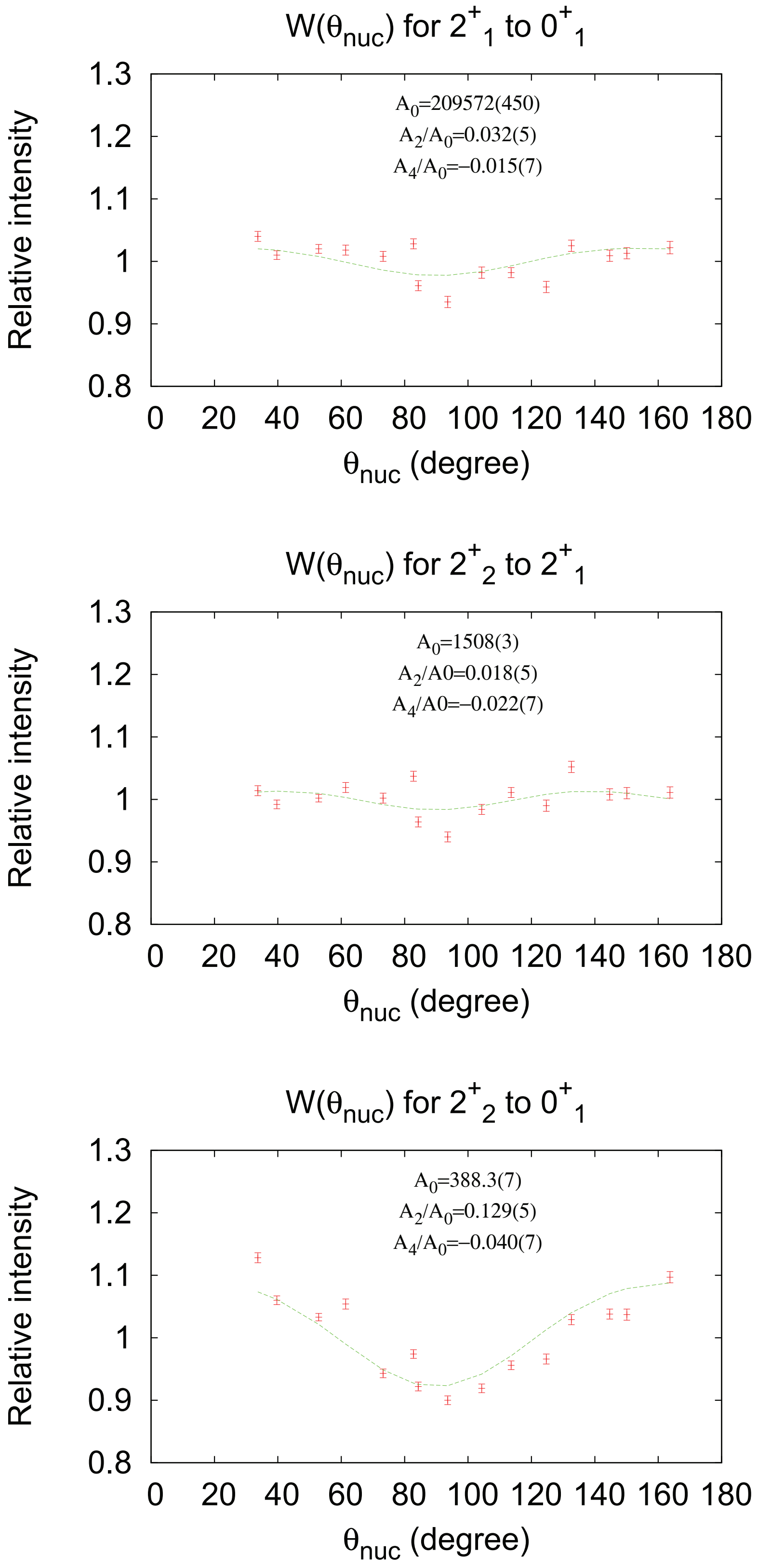

Figure 6.11: Angular distributions from the 2_1^+ and 2_2^+ states in ^{128}Xe.

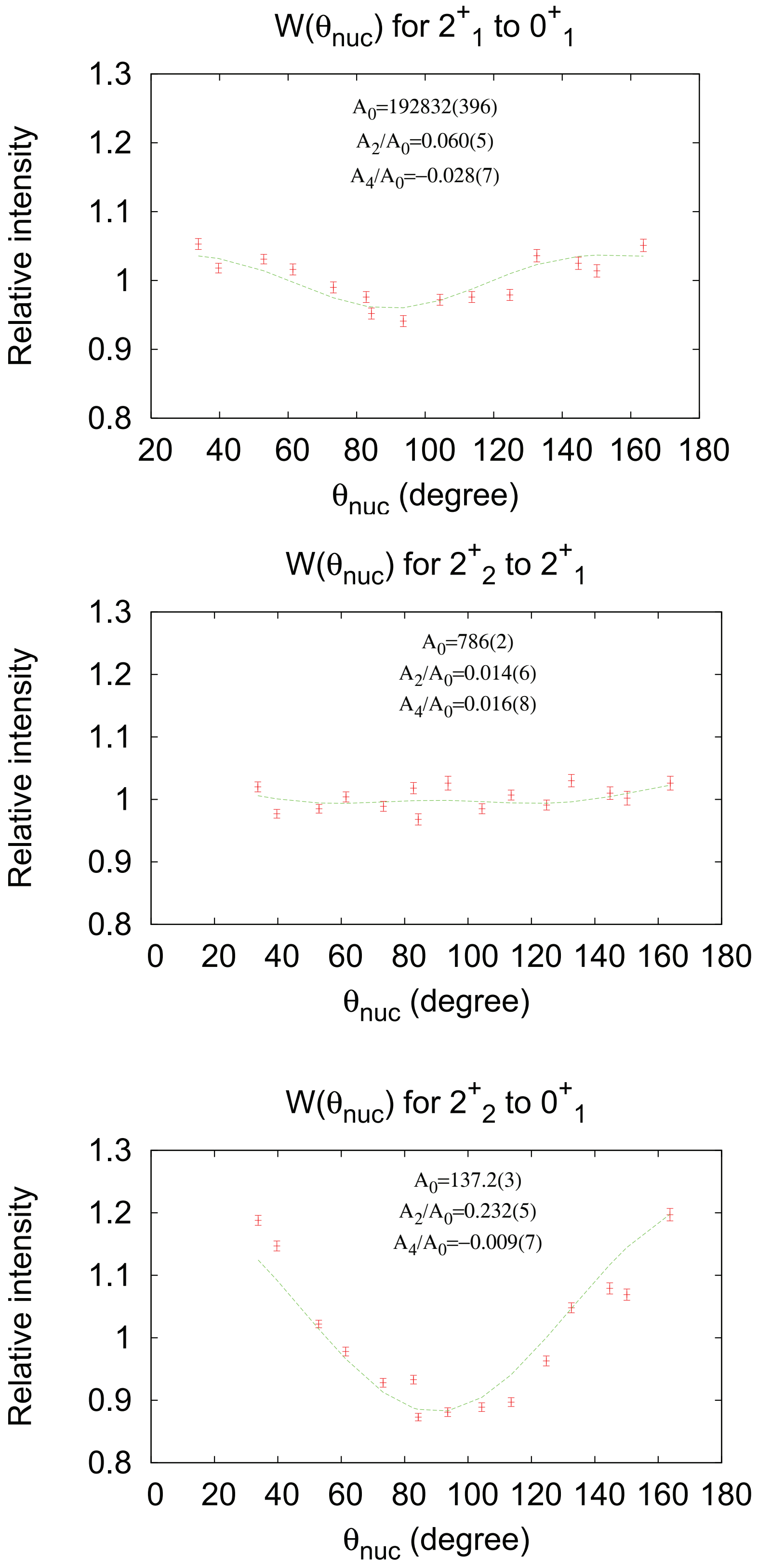

Figure 6.12: Angular distributions from the 2_1^+ and 2_2^+ states in ^{130}Xe.

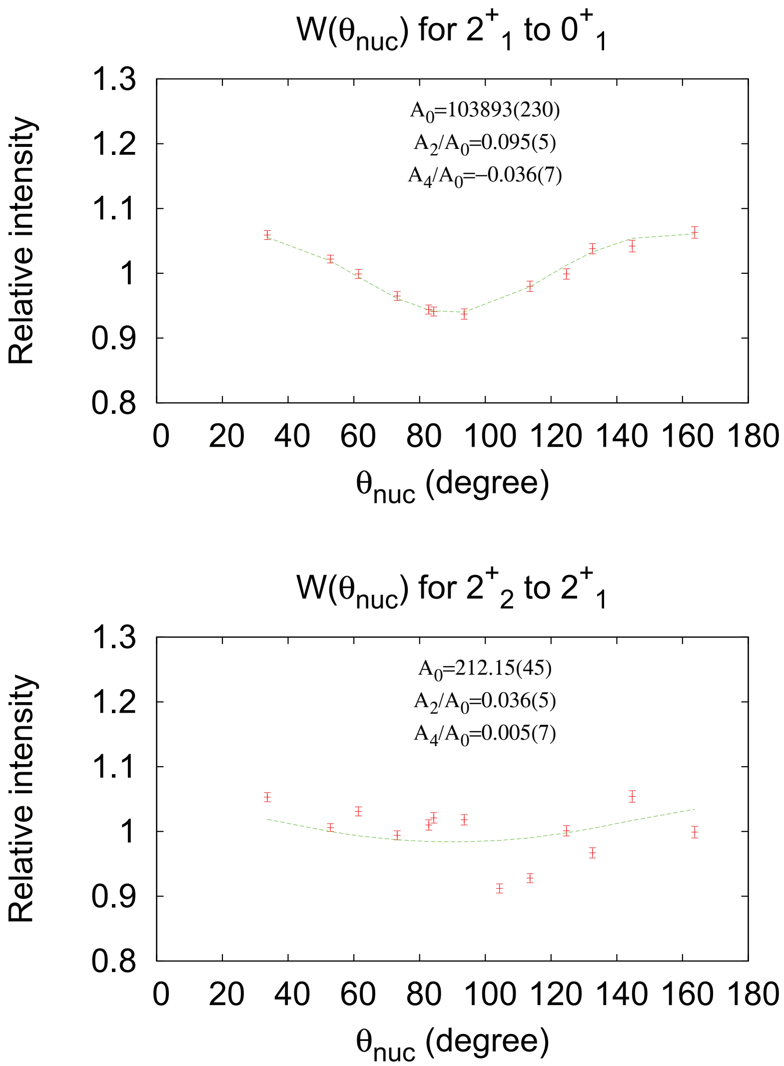

Figure 6.13: Angular distributions from the 2_1^+ and 2_2^+ states in ^{132}Xe. No angular distribution could be measured for the 1297-keV transition ($2_2^+ \rightarrow 2_1^+$). This line was mixed with the strong 1317-keV line ($2_{1,\mathrm{ms}}^+ \rightarrow 2_1^+$).

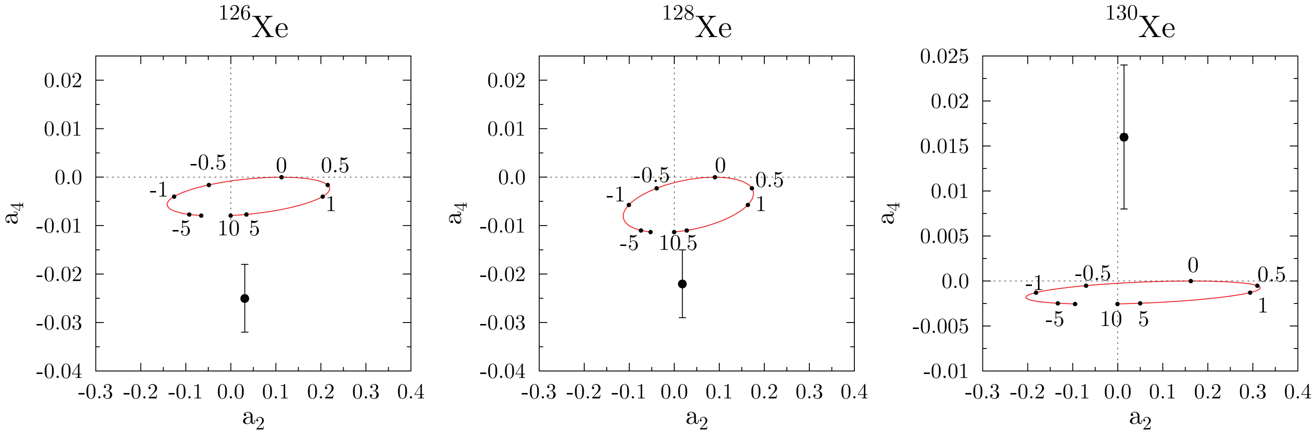

Figure 6.14: Angular distributions ellipses for $2_2^+ \rightarrow 2_1^+$ transitions of ^{126,128,130}Xe calculated with the orientation resulting from $a_2 = A_2/A_0$ and $a_4 = A_4/A_0$ coefficients for the $2_2^+ \rightarrow 0_1^+$ transitions. The numbers on the ellipses denote the values for the mixing ratio δ. The points outside from the ellipses correspond to the $a_2 = A_2/A_0$ and $a_4 = A_4/A_0$ coefficients for the $2_2^+ \rightarrow 2_1^+$ transitions. The resulting values of δ are given in Table 6.5.

Isotope	δ (this work)	δ (Litt.)	Reference
^{126}Xe	5.24(9)	9.1^{+43}_{-2}	[109]
^{128}Xe	6.06^{13}_{-11}	4.4(7)	[128]
^{130}Xe	-0.30(5)	3.75(12)	[136]

Table 6.5: Values of the measured mixing ratio δ values for the $2^+_2 \rightarrow 2^+_1$ transitions of ^{126,128,130}Xe compared with the previously known values (references are listed in the last column).

7 Results and Discussion

In the following the results for the nuclei ^{126,128,130,132}Xe are presented. In the last part, and for better understanding of the evolution of the one-quadrupole phonon $2^+_{1,\mathrm{ms}}$ Mixed-Symmetry State in even-even Xe isotopes, they are combined with the results of ^{134}Xe [90]. Details of the experiment have been already given in the previous section 6.1. The data analysis described in section 6.2 was the same for each nuclide. All of our results deal with collectivity in the proton-neutron valence shell and some new interesting and surprising results have been found. Our results are outlined as

- O(6)-symmetry breaking in the γ-soft nuclei ^{124,126}Xe
- ^{128}Xe fails a robust test of E(5) symmetry
- The $2^+_{1,\mathrm{ms}}$ mixed-symmetry states in ^{130,132}Xe.

7.1 ^{124}Xe

Details concerning the experiment can be found in section 6.1. Gammasphere was used in singles mode, resulting in an average counting rate of 8000 counts-per-second (cps), while the room background was producing about 600 cps. A total of 5.1×10^8 events of γ-ray fold 1 or higher was collected in about 12 hours. The room background has been subtracted as explained in section 6.2.4. The singles spectrum for ^{124}Xe is displayed in Fig. 7.1. All γ rays in the spectrum originate from ^{124}Xe nuclei recoiling with $v/c \approx 6.3(2)\%$. They have been placed in the level scheme of ^{124}Xe and plotted in Fig. 7.2 and their corresponding intensities are listed on Table 7.1. Most of these γ rays have already been identified in ^{124}Xe [102, 100, 101, 105]. In addition, we have observed three new transitions with respective energies of 1051, 1413 and 1444 keV. About 4% of the data have γ-ray fold higher than 1. These events were sorted into a γ-γ coincidence matrix. The coincidence relationships and the energy balances suggest that the 1051-keV γ ray connects the 3^- state at 1898 keV [105] to the 2^+_2 level at 847 keV. The latter two γ rays, at 1413 keV and the 1444 keV, depopulate a newly observed level at 2291 keV. Population yields of each state have been deduced from γ-singles and $\gamma\gamma$-coincidence data. The contributions from the electron conversion decays to the populations of the states was small in comparison to the systematic errors ($< 1.5\%$, [131]) and have been neglected. The contributions of known transitions that we were not able to observe (*e.g.* due to too small energy or contaminations), have been determined from previously published branching ratios from Ref. [103]. The observed relative yields measure the Coulomb Excitation (CE) cross sections relative to the 2^+_1 state. The multiple code CLX, based on the Winther-De Boer theory [77] has been used to determine the set of matrix elements for reproducing the observed relative cross sections. The previously known $B(E2; 2^+_1 \rightarrow 0^+_1)$=0.2121(54) e^2b^2 value from Ref. [103] sets the absolute scale. The signs of the matrix elements have been chosen as the corresponding one proposed by an IBM-1 calculation and are also given in Table 7.1. The parameters of the IBM-1 calculation are listed in Table 7.4. Details concerning the IBM-1 fit are given in section 7.3. For more details concerning the CLX analysis (energy loss, constraints, quadrupole moments, relative phases), see section 6.2.5. The data yield 25 absolute $E2$ transition strengths between low spin states (see section 6.2 for more details concerning the Coulex analysis) and 9 lifetimes values. The spectroscopic information is summarized in Table 7.1 and the lifetimes are given in Table 7.2.

- **2^+_1 state at 354 keV**
  The spectrum of Fig. 7.1 is dominated by the 354-keV line from the 2^+_1 state to the ground state with about 1.68×10^8 counts. Due to the nuclear deorientation effect, no angular distribution has been observed for this transition (see section 6.2.6).

- **4^+_1 state at 879 keV**
  The $4^+_1 \rightarrow 2^+_2$ transition with $E_\gamma = 32$ keV has not been observed. However, this transition was included in the CLX calculations and was inferred instead (with a large uncertainty) from the CE yield of the 4^+_1 state, assuming that a direct $E4$ population from the ground state is not larger than 26 W.u.($E4$).

- **2^+_3 state at 1629 keV**
  The 2^+_3 state at 1629 keV decays by a strong collective $E2$ transition to the full symmetric state 0^+_2 [62(36) W.u.].

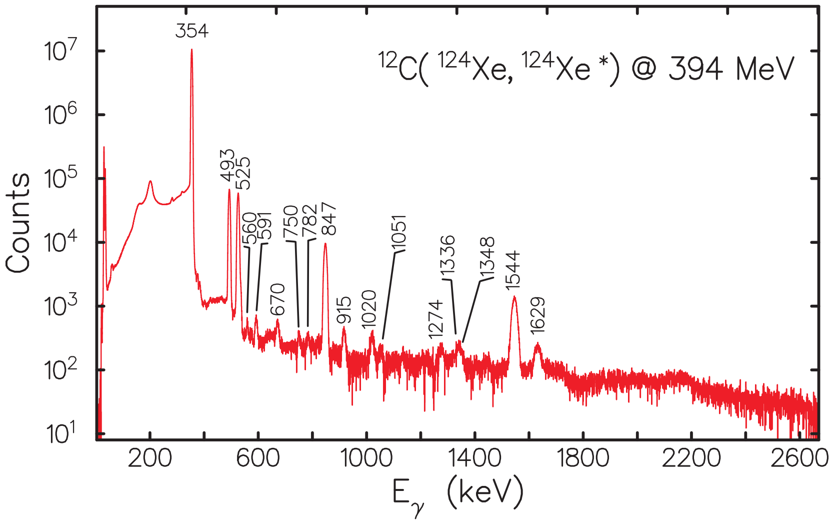

Figure 7.1: Background-subtracted, Doppler-corrected γ-ray spectrum of ^{124}Xe observed with Gammasphere after Coulomb excitation on a carbon target. The weak transitions in ^{124}Xe are not indicated.

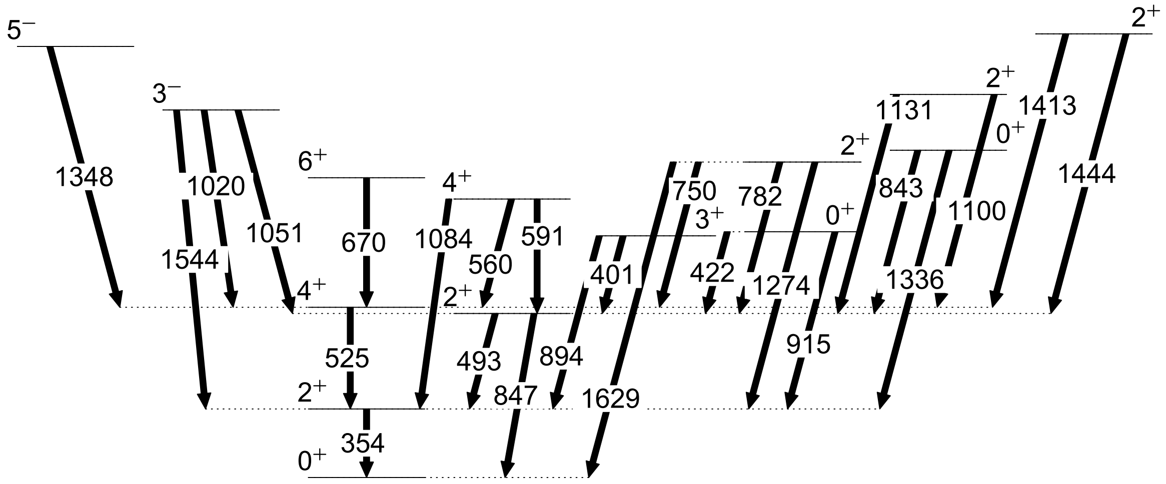

Figure 7.2: γ-ray transitions observed in the ^{12}C(^{124}Xe,^{124}Xe*) Coulomb excitation reaction.

This untypical behavior enables us to rule out the mixed-symmetry character of this state eventhough the absolute $B(M1)$ value to the 2_1^+ state could not be measured. The mixing ratio for the $2_3^+ \rightarrow 2_1^+$ transition is unknown and due to low statistics, our data did not enable us to measure it from the angular distributions. In Table 7.1, the $B(E2)$ values of the mixed transitions coming from this state have been calculated by assuming pure $E2$ transitions, hence the upper values. However, if we assume that the $2_3^+ \rightarrow 2_1^+$ transition is a pure $M1$ transition, we finally obtain $B(M1; 2_3^+ \rightarrow 2_1^+) \leq 0.0025(3)\ \mu_N^2$ which supports the fact that the 2_3^+ state at 1629 keV is not a MSS.

- **2_4^+ state at 1978 keV**
  The $2_4^+ \rightarrow 0_3^+$ transition with E$_\gamma$=288 keV has not been observed. However we included it in the CLX calculations. The yields from the 2_4^+ and 0_3^+ are known with a certain precision and the matrix element of the $2_4^+ \rightarrow 0_3^+$ transition does not influence much the populations of the 2_4^+ and 0_3^+ states. It was calculated that a $B(E2; 2_4^+ \rightarrow 0_3^+)$ value between 5 W.u. and 68 W.u. will modify the yields of the 2_4^+ and 0_3^+ states within their experimental error bars. The mixing ratio δ of the $2_4^+ \rightarrow 2_1^+$ transition is unknown, the upper $B(E2)$ and $B(M1)$ values refered in Table 7.1 are calculated for pure $E2$ and $M1$ transitions respectively. The $B(M1; 2_4^+ \rightarrow 2_1^+) \leq 0.0014(5)\ \mu_N^2$ upper value rules out the mixed-symmetry character of this state.

Table 7.1: Measured properties of the levels and γ-ray transitions in ^{124}Xe. The absolute $E2$ strengths are compared to sd-IBM-1 calculations.

E_{level} (keV)	J^π	E_γ (keV)	I_γ	J^π_{final}	δ^a	σ	Transition strength^b Expt	IBM-1^c
354	2^+_1	354	$10^6(79)$	0^+_1		+	$57.7(15)^d$	57.7
847	2^+_2	493	10019(80)	2^+_1	$+7.84^{+7.90}_{-1.59}$	-	64(5)	61.24
		847	3332(12)	0^+_1		-	1.45(12)	1.47
879	4^+_1	525	10297(75)	2^+_1		+	$67.6(19)^d$	85.08
		$32^{\ e}$		2^+_2		+	92(58)	0.06
1248	3^+_1	$894^{\ f}$	24(2)	2^+_1	$+3.41^{+0.45}_{-0.36}$	+	2.33(38)	2.20
		401	17(2)	2^+_2	$+15.7^{+15.8}_{-7.9}$	+	95(19)	65.69
		$369^{\ e}$	$3(1)^g$	4^+_1	$+3.85^{+0.57}_{-0.45}$	-	26(12)	20.71
1269	0^+_2	915	130(2)	2^+_1		+	13.2(31)	16.12
		422	18(2)	2^+_2		+	87(21)	76.45
1438	4^+_2	591	80(2)	2^+_2		+	66(12)	48.48
		560	39(2)	4^+_1	$2.29^{+0.76}_{-0.35}$	-	35(6)	33.53
		$1084^{\ f}$	$1.5(8)^g$	2^+_1		-	0.058(11)	0.33
1548	6^+_1	670	54(2)	4^+_1		+	90(18)	96.95
1629	2^+_3	1629	154(3)	0^+_1		-	0.315(49)	0.07
		1274	87(4)	2^+_1		+	$\leq 0.613(68)^h$	0.02
		1274		2^+_1			$B(M1) \leq 0.0025(3)^h\ \mu_N^2$	
		750	56(2)	4^+_1		-	5.55(79)	4.50
		782	44(2)	2^+_2		+	$\leq 3.54(71)^h$	1.03
		782		2^+_2			$B(M1) \leq 0.0055(11)^h\ \mu_N^2$	
		$360^{\ e}$	$30(16)^g$	0^+_2		-	62(36)	35.85
1690	0^+_3	$1336^{\ f}$	81(3)	2^+_1		-	11.9(17)	12.75
		$843^{\ f}$	13(2)	2^+_2		+	18.5(17)	14.85
1898	3^-_1	1544	1179(9)	2^+_1				
		1020	113(3)	4^+_1				
		1051	41(2)	2^+_2				
		1898		0^+_1		+	$B(E3)=0.123(24)^i$	
1978	2^+_4	$1131^{\ f}$	23(4)	2^+_2		-	$\leq 2.75(84)^h$	4.39
		1131		2^+_2			$B(M1) \leq 0.0090(27)^h\ \mu_N^2$	
		$1978^{\ e}$	$15(4)^{\ g}$	0^+_1		+	0.11(2)	0.10
		$1624^{\ e}$	$11(3)^{\ g}$	2^+_1		-	$\leq 0.21(7)^h$	0.15
		1624		2^+_1			$B(M1) \leq 0.0014(5)^h\ \mu_N^2$	
		1100^f	11(2)	4^+_1		+	1.47(38)	6.36
		288^e		0^+_3		-	$5 \div 68$	33.
2226	$5^{(-)}$	1348^f	27(2)	4^+_1				
2291	(2^+_5)	1444^f	35(6)	2^+_2		-		
		1413^f	5(1)	4^+_1		+		

---

[a] The multipole mixing ratios are taken from Ref. [102].

[b] $B(E2)$ values are given in W.u.(1 W.u. = 36.7 $e^2\text{fm}^4$), $B(M1)$ in μ_N^2 and the $B(E3; 0^+_1 \rightarrow 3^-_1)\uparrow$ value is given in e^2b^3.

[c] $E2$ transition strengths from a numerical IBM-1 calculation with parameters from Ref. [102].

[d] From Ref. [103].

[e] This transition is not observed directly, but it is included in the calculations for the Coulomb excitation cross-sections for a best match with the data.

[f] This transition was observed only in coincidence spectra.

[g] Determined through the branching ratio from Ref. [102] or National Nuclear Data Center (http://www.nndc.bnl.gov).

[h] Upper values since the mixing ratio was unknown, $B(E2)$ and $B(M1)$ upper values are given for pure $E2$ and pure $M1$ transitions, respectively.

[i] The $B(E3; 0^+_1 \rightarrow 3^-_1)\uparrow$ value determined from our data. In Ref. [105] a value of B(E3)↑ = 0.091(10) e^2b^3 is reported.

Table 7.2: Lifetimes of the low-lying states in ^{124}Xe compared with the previously known values from the literature.

E_{level} (keV)	J^{π}	τ (ps)	τ^{a} (ps)	τ^{b} (ps)
354	2_1^+	67.5(17)[a]	67.5(17)	48(3)
847	2_2^+	8.87(64)	17.8(30)	10(2)
879	4_1^+	8.24(28)	8.19(23)	5.1(6)
1248	3_1^+	8.52(99)	9.0(10)	9(2)
1269	0_2^+	2.32(49)		
1438	4_2^+	3.12(43)		3(1)
1548	6_1^+	1.84(37)	1.86(16)	1.4(6)
1629	2_3^+	2.65(21)		
1690	0_3^+	0.380(46)		
1978	2_4^+	1.65(26)		

---

[a] From Ref. [103].

[b] From Ref. [104].

7.2 ^{126}Xe

Details about the experiment can be found in section 6.1. The singles spectrum was Doppler corrected (recoiling velocity β=6.4(2)%) and time random background subtracted. It is displayed in Fig. 7.3. The total number of events was 1.3×10^9 for a running time of ∼29 h and approximately 1.8×10^7 of γ-ray fold higher than 1 were sorted into a $\gamma\gamma$-coincidence matrix. All γ transitions observed have been placed in the level scheme of ^{126}Xe and plotted in Fig. 7.4 and their corresponding intensities are listed in Table 7.3. They were reported previously in [106] [107] and [108] except the 1373 keV γ-ray line originating from the decay of the 3_2^- state at 2315 keV to the 4_1^+ state at 942 keV. Population yields of each state have been deduced from γ-singles and $\gamma\gamma$-coincidence data. The contributions from the electron conversion decays to the populations of the states was small in comparison to the systematic errors (< 1.5%, [131]) and have been neglected. The contributions of known transitions that we were not able to observe (*e.g.* due to too small energy or contaminations), have been determined from previously published branching ratios from Ref. [109]. The observed relative yields measure the Coulomb Excitation (CE) cross sections relative to the 2_1^+ state. The multiple code CLX, based on the Winther-De Boer theory [77] has been used to determine the set of matrix elements for reproducing the observed relative cross sections. The previously known $B(E2; 2_1^+ \to 0_1^+)$=0.152(5) e^2b^2 value from Ref. [109] sets the absolute scale. The signs of the matrix elements have been chosen as the corresponding one proposed by an IBM-1 calculation and are also given in Table 7.3. The parameters of the IBM-1 calculation are listed in Table 7.4. Details concerning the IBM-1 fit are given in section 7.3. For more details concerning the CLX analysis (energy loss, constraints, quadrupole moments, relative phases), see section 6.2.5. Our analysis resulted in 22 absolute and 6 upper limits for $B(E2)$ values, 8 values and 1 upper value for the lifetimes (τ), which are also listed on Table 7.3.

- **2_1^+ state at 388 keV**
  The spectrum of Fig. 7.3 is dominated by the 388-keV line from the 2_1^+ state to the ground state with about 7.09×10^8 counts. The corresponding angular distribution with its respective coefficients $a_2 = A_2/A_0$ and $a_4 = A_4/A_0$ is given in Fig. 6.10.

- **2_2^+ state at 879 keV**
  The angular distributions coming from this state with their respective coefficients $a_2 = A_2/A_0$ and $a_4 = A_4/A_0$ are given in Fig. 6.10. A value of $\delta = 5.24(9)$ has been deduced. This value is in agreement with the previously known $\delta = 9.1^{4.3}_{-2}$ value from Ref. [109]. However the CLX calculations have been made by using the $\delta = 9.1^{4.3}_{-2}$ value. In this case both δ values are large and assign almost a pure $E2$ transition character for the $2_2^+ \to 2_1^+$ transition (>96%).

- **4_1^+ state at 942 keV**
  The unobserved $4_1^+ \to 2_2^+$ transistion at 62 keV does not play a significant role for the population of the 4_1^+ state at 942 keV. Another issue with the population of the 4_1^+ is the contribution of the one-step $E4$ excitation. In Fig. 7.5 is shown different sets of $B(E2; 4_1^+ \to 2_1^+)$ and $B(E4; 4_1^+ \to 0_1^+)$ values reproducing the experimental yields of the 4_1^+ state (blue spots). Since, we could not quantify nor estimate this $B(E4)$ transition strength, we chose to quote the $B(E2; 4_1^+ \to 2_1^+)$ value in Table 7.3 assuming no $E4$ transition from the ground state.

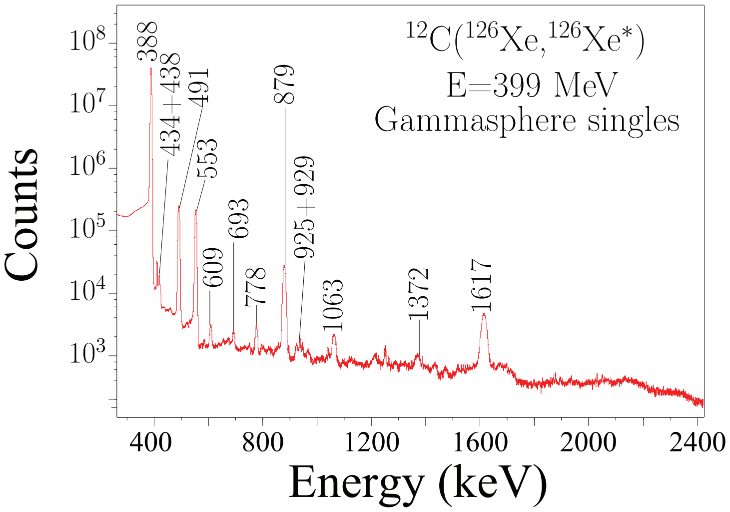

Figure 7.3: Background-subtracted and Doppler-corrected single γ-ray spectra for the sum over all Ge detectors after the Coulomb excitation on ^{12}C targets for ^{126}Xe.

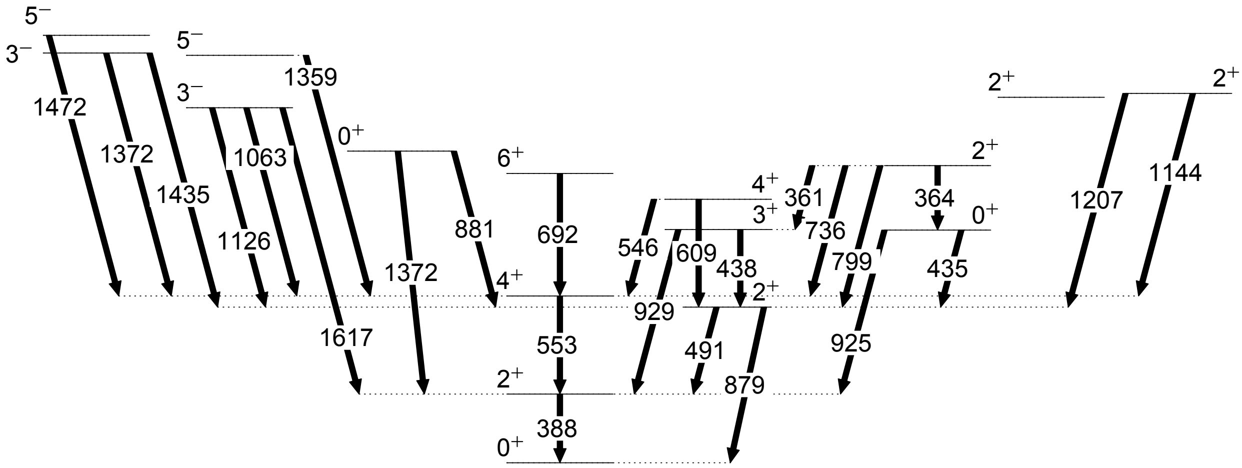

Figure 7.4: γ-ray transitions observed in the ^{12}C(^{126}Xe,^{126}Xe*) Coulomb excitation reaction.

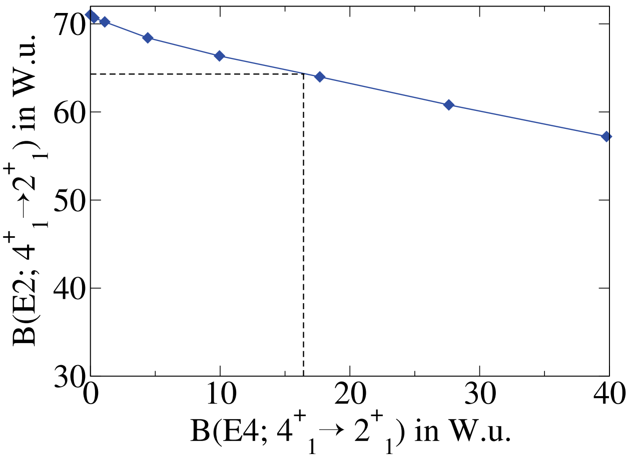

Figure 7.5: Set of different $B(E2; 4^+_1 \rightarrow 2^+_1)$ and $B(E4; 4^+_1 \rightarrow 0^+_1)$ strengths reproducing the experimental yields of the 4^+_1 state (blue spots). The blue line is for guiding the eye (no interpolation has been made). The horizontal dashed line is the lower value of the $B(E2; 4^+_1 \rightarrow 2^+_1) = 71.0(67)$ W.u. which corresponds to a $B(E4; 4^+_1 \rightarrow 0^+_1)$ value of about 17 W.u. (vertical dashed line).

- **0^+_2 state at 1314 keV and 3^+_1 state at 1317 keV**
  The 0^+_2 state at 1314 keV decays through the 434 keV γ-ray line to the 2^+_2 state and through the 925 keV γ-ray line to the 2^+_1 state. These lines are doublets with the two γ-ray lines coming from the 3^+_1 state at 1317 keV. This 3^+_1 state decays also to the the 2^+_2 state with E_γ=438 keV and to the 2^+_1 state with E_γ=925 keV. The energy resolution achieved in our experiment did not permit us to resolve these two doublets. Therefore we fitted the intensities of each doublet and we used the previously known branching ratios from Ref. [109] to obtain the individual respective intensities.

- **4^+_2 state at 1488 keV**
  Similarly, the 546 keV γ-ray line from the 4^+_2 state at 1488 keV to the 4^+_1 state is a doublet with the strong 553 keV γ-ray line from the 4^+_1 state at 942 keV to the 2^+_1 state. The individual intensity of the 546 keV γ-ray line has been deduced from the known branching ratio from Ref. [109] and the intensity of the $4^+_2 \rightarrow 2^+_2$ transition of 609 keV. Again like the procedure for the 4^+_1 state, no $E4$ transition from the ground state has been considered.

- **2^+_3 state at 1678 keV**
  The mixing ratio for the $2^+_3 \rightarrow 2^+_1$ transition is so far unknown. Due to low statistics our data did not enable us to measure it from the angular distributions. In Table 7.3, the $B(E2)$ values for the mixed transitions coming from this state have been calculated by assuming pure $E2$ transitions, hence the upper values. However, if we assume that the $2^+_3 \rightarrow 2^+_1$ transition is a pure $M1$ transition, we obtain $B(M1; 2^+_3 \rightarrow 2^+_1) \leq 4.35(87) \times 10^{-4}\ \mu_N^2$. This small value rules out the mixed-symmetry character of this state.

- **2^+_5 state at 2086 keV**
  The 1698-keV line from the 2^+_5 state to the 2^+_1 state has not been seen in our experiment. This 1698-keV line has also never been observed so far ([109]) and may not exist at all. Therefore we can rule out the mixed-symmetry character of this 2^+_5 state. The $2^+_5 \rightarrow 0^+_3$ transition with E_γ=326 keV has neither been observed. However, we included it in the CLX calculations. The yields from the 2^+_5 and 0^+_3 are known with a certain precision and the matrix element of the $2^+_5 \rightarrow 0^+_3$ transition does not influence much the populations of the 2^+_5 and 0^+_3 states. It was calculated that a $B(E2; 2^+_5 \rightarrow 0^+_3)$ value between 11 W.u. and 48 W.u. will influence the yields of the 2^+_5 and 0^+_3 states within their experimental error bars.

- **2^+ state at 2455 keV**
  Since the mixing ratio for the $2^+ \rightarrow 2^+_1$ is unknown [109], we assumed a pure $E2$ transition, leading to an upper

value $B(E2; 2^+ \rightarrow 2_1^+) \leq 1.82(54)$ W.u.. By assuming that this transition is purely $M1$, we obtain $B(M1; 2^+ \rightarrow 2_1^+) \leq 0.020(6)$. This small value rules out the mixed-symmetry character of this state.

The interpretation of our results in ^{124,126}Xe in the framework of the IBM-1 is given in the next part.

Table 7.3: Measured properties of the levels and γ-ray transitions in ^{126}Xe. The absolute $E2$ strengths are compared to sd-IBM-1 calculations.

E_{level}	J^{π}	E_{γ}	I_{γ}	J^{π}_{final}	δ^{a}	σ	Transition strength^{a}		τ
(keV)		(keV)					Exp.	IBM-1	(ps)
388	2^+_1	388	10^6	0^+_1		+	41.0(13)^{b}	41.0	58.8(19)^{b}
879	2^+_2	491	7836(58)	2^+_1	$+9.1^{+43}_{-2}$	-	43.2(26)	48.9	13.5(17)
		880	2134(17)	0^+_1		+	0.63(7)	0.65	
942	4^+_1	63^{c}		2^+_2		-		0.01	5.9(6)
		553	7655(56)	2^+_1		+	71.0(67)	58.9	
1314	0^+_2	434^{d}	11.1(18)	2^+_2		+	64(9)	58.0	4.36(54)
		925^{d}	45.4(21)	2^+_1		-	5.9(9)	5.51	
1317	3^+_1	376^{e,g}	1.43(28)	4^+_1		-	$\leq$22.1(13)^{f}	15.9	11.8(12)
		438^{d}	7.7(15)	2^+_2	$+8^{+3}_{-2}$	+	55.7(63)	45.0	
		929^{d}	7.3(15)	2^+_1	$+1.6^{+3}_{-7}$	-	0.90(23)	0.91	
1488	4^+_2	546^{d}	35.6(6)	4^+_1	$+3.0^{+10}_{-9}$	+	28.3(38)	25.8	4.2(3)
		609	70.7(9)	2^+_2		-	36.1(42)	33.2	
		1100^{d}	14.9(3)	2^+_1		-	0.40(8)	0.14	
1635	6^+_1	693	54.7(18)	4^+_1		+	84(11)	64.8	1.64(21)
1678	2^+_3	361^{d,h}	5.1(20)	3^+_1		-	$\leq$ 20.6(44)^{f}	28.3	9.1(9)
		364^{d,h}	9.8(21)	0^+_2		+	38.3(91)	23.1	
		736^{g}	8.54(53)	4^+_1		-	0.96(4)	1.36	
		799^{h}	24.1(14)	2^+_2		+	$\leq$ 1.86(41)^{f}	0.23	
		1290^{g}	14.7(9)	2^+_1		-	$\leq$ 0.10(2)^{f}	0.002	
				2^+_1			$B(M1) \leq 4.35(87) \times 10^{-4f}\ \mu_N^2$		
		1678^{g}	33.8(21)	0^+_1		-	0.063(14)	0.02	
1760	0^+_3	881^{h}	7.8(16)	2^+_2		-	13.4(41)	4.75	0.36(8)
		1372^{h}	58.6(22)	2^+_1		-	10.9(25)	11.1	
2005	3^-_1	1063	166(4)	4^+_1					
		1126^{h}	29.1(18)	2^+_2					
		1617	885(11)	2^+_1					
						+	$B(E3)$=0.090(15)^{i}		
2086	2^+_5	326^{e}		0^+_3		+	11÷48	23.4	$\leq$3.0(7)^{j}
		1144^{g}	10.4(11)	4^+_1		-	1.63(16)	4.9	
		1207^{h}	18.2(15)	2^+_2	$+0.9^{+5}_{-3}$	+	0.99(61)	3.0	
		2086^{g}	4.99(58)	0^+_1		-	0.04(1)	0.07	
2301	$5^{(-)}$	1359^{h}	15.6(12)	4^+_1					
2315	$3^{(-)}$	1373^{h}	14.2(11)	4^+_1					
		1435^{h}	31.1(18)	2^+_2					
2414	$5^{(-)}$	1472^{h}	13.7(11)	4^+_1					
2455	2^+	1138^{g}	0.81(10)	3^+_1		+	$\leq$ 1.96(60)^{f}	0.0002	0.20(4)
		1514^{g}	1.36(15)	4^+_1		-	0.79(25)	0.0015	
		1576^{g}	3.66(39)	2^+_2		-	$\leq$ 1.76(52)^{f}	0.0009	
		2067^{h}	14.8(15)	2^+_1		-	$\leq$ 1.82(54)^{f}	0	
				2^+_1			$B(M1) \leq 0.020(6)^{f}\ \mu_N^2$	0	
		2455^{g}	2.69(30)	0^+_1		+	0.14(4)	0	

---

[a] $B(E2)$ values are given in W.u. (1 W.u.$(E2)$=0.003752 e^2b^2), $B(M1)$ in μ_N^2 and the $B(E3; 0^+_1 \to 3^-_1)\uparrow$ value is given in e^2b^3.

[b] Adopted value taken from Ref. [94].

[c] This transition is not observed. Contrary to Ref. [89], this transition does not play a relevant role for the population of the 4^+_1 state.

[d] These transitions are doublets, the individual intensities have been separated from the known branching ratios taken from Ref. [109].

[e] This transition is not observed directly but it is included in the calculations for the Coulomb cross-sections for a best match with the data.

[f] Upper values since the mixing ratio was unknown, $B(E2)$ and $B(M1)$ upper values are given for pure $E2$ and pure $M1$ transitions, respectively.

[g] Determined through the branching ratio from [109].

[h] This transition was observed only in coincidence spectra.

[i] In Ref. [105], a $B(E3)\uparrow = 0.085(13)$ e^2b^3 value is reported.

[j] Upper value since only a lower value of the total width (Γ_{tot}) of the state has been measured.

7.3 O(6)-symmetry breaking in the γ-soft nuclei ^{124,126}Xe

Symmetries offer powerful quantitative concepts in many fields of physics ranging from the formulation of the fundamental forces to the classification of many-body systems. In quantum mechanics the presence of a symmetry is related to conserved quantum number that can be established experimentally. Analogously, symmetry breaking is related to a situation in which the wave functions of the system contains many components with different quantum mumbers. It is intriguing to study the question when and how a symmetry dissolves on a quantitative basis. Nuclear collective excitations states offer a unique quantum laboratory where this question can be studied experimentally. In nuclear physics, the three dynamical symmetries [15, 29] of the Interacting Boson Model (IBM), U(5) [13], SU(3) [52], and O(6) [53] provide valuable benchmarks for the description of nuclear quadrupole collectivity at low and medium angular momenta. These three symmetries correspond to analytically solvable cases of the geometrical Bohr Hamiltonian [54]- the harmonic vibrator, the quadrupole-deformed axial rotor, and the γ-unstable rotor [31]. Such idealized cases are hardly ever observed in nuclei. Finding nuclides with behaviours close to expectations for specific dynamical symmetries is an intriguing task because such nuclei serve as benchmarks for the evolution of nuclear collectivity [110]. However, a quantitative answer to the question to what extent a certain symmetry is preserved or broken in nuclei requires that one measure observables that are particularly sensitive to the symmetry under investigation. It is the purpose of this discussion to study the degree of O(6)-breaking in the cases of ^{124}Xe and ^{126}Xe, nuclei considered before to be close to the O(6) dynamical symmetry [21].

The O(6) symmetry of the sd-IBM-1 is based on the chain U(6)$\supset$ O(6)$\supset$ O(5)$\supset$ O(3) of nested sub-algebras with quantum numbers N, σ, τ, and L, respectively [15, 29]. The empirical evidence for the existence of nuclei at the O(6) dynamical limit of the IBM is based on energy level patterns, branching ratios and, more convincingly, on selection rules for $E2$ transitions. Within the Consistent Q-Formalism (CQF) [111] they are such that $E2$ transitions are allowed and collective only between states with $\Delta\sigma = 0$ and $\Delta\tau = \pm 1$ [29][1]. It is the $\Delta\sigma = 0$ selection rule that is definitive of pure O(6)-symmetry; the $\Delta\tau = \pm 1$ selection rule is rather ubiquitous for all nuclei between U(5) and O(6) dynamical symmetries. A nucleus showing energy spectrum and decay patterns which can be classified in terms of σ, τ, L quantum numbers and obeys the respective selection rules is said to possess O(6) symmetry. Observation of the O(6) symmetry in nuclei has first been reported in the case of ^{196}Pt [113]. This claim was based on energy level pattern and $E2$ decay branching ratios that closely follow the O(6) selections rules. It was later on supported by establishing a lower limit for the lifetime of the 0_3^+ state, the lowest state of the $\sigma = N - 2$ representation [114]; the resulting upper limits for the absolute $B(E2)$ values are small, in agreement with pure O(6) dynamical symmetry [114]. Another, even more extensive region of O(6)-candidate nuclei is found in the Xe-Ba-Ce region [21] around mass number $A = 130$. It has been shown that the low-spin structures of the nuclei ^{128}Xe [115], ^{126}Xe [108] and ^{124}Xe [102] manifest O(5)-like arrangements of energy levels and $E2$ branching ratios which reflects the selection rules for the $\sigma = N$ states of the O(6). On the other hand, the nuclei from the Pt and the Xe-Ba-Ce regions exhibit two systematic deviations from the exact O(6) symmetry, *i.e.*, the smaller than expected energy staggering in the quasi-γ bands and the τ-compression effect [21]. These deviations can be accounted for by adding perturbative terms to the O(6) Hamiltonian [116]. These terms improve the description of the low-lying states with $\sigma = N$ [102]. Quantifying the degree of symmetry preservation (or breaking), introduced by such realistic symmetry-perturbing terms is not an easy task because it, ideally, requires information on absolute $E2$ transition rates, preferably between states with different O(6) quantum numbers. This crucial experimental information is either scarce [108, 119, 103] or often absent altogether. This is particularly true for transitions between off-yrast states, which supposedly belong to higher $\tau \geq 3, 4$ and lower $\sigma < N$ multiplets. Thus, due to the lack of data, a quantitative assessment of the goodness of the O(6) quantum number σ in the Xe-Ba region has not been performed to date. In this respect, the question of the extent in which the energies and the $B(E2)$ branching ratios of levels with $\sigma = N$ can serve as a unique signature for O(6)-like behaviour [120, 121], especially for the off-yrast states, also remains open. To address these issues, we have measured absolute $E2$ strengths between off-yrast, low-spin states of ^{124}Xe and ^{126}Xe.

The energy levels of ^{124}Xe and ^{126}Xe with positive parity appear to form a pattern typical for O(6) symmetry (see Fig. 7.6 and Fig. 7.7). Similarly to [102] and [89], for each eigenstate with O(6) quantum number $\sigma = N$ a corresponding nuclear state can be found up to O(5) quantum number $\tau = 5$ and angular momentum $10\hbar$, while the 0_3^+ state seems to be the band-head of the excited O(6) family with $\sigma = N - 2$. Therefore, it is reasonable to check whether the data on absolute $E2$ strengths can be understood qualitatively in terms of O(6) ($\Delta\sigma = 0$) and O(5) ($\Delta\tau = \pm 1$) selection rules.

Indeed, the data for transitions between the states tentatively assigned to the $\sigma = N$ multiplet typically concur to a large extend with the O(5) ($\Delta\tau = \pm 1$) selection rules (see Tables 7.1, 7.3): Those $E2$ transitions that violate the O(5) selection rules are suppressed by about one order of magnitude to a level of $\sim$ 1 W.u., only. In our experiments we were able to determine the $E2$ transition strengths for the decays of off-yrast, low-spin states such as the 2_3^+ level. If classified according to O(5) symmetry, this state is the lowest one from the $\tau = 4$ multiplet (see Fig. 7.6 and 7.7). In agreement with the O(5) selection rules, it decays to the 0_2^+ ($\tau = 3$) state by a collective $E2$ transition. The other transitions observed

---

[1] The O(6) selection rules depend also on the choice of the $E2$ operator. In its most general one-body form $T(E2) = e\left(s^+\tilde{d} + d^+s + \chi_{\mathrm{E2}}[d^+\tilde{d}]^{(2)}\right)$, the $E2$ operator also generates transitions between states with $\Delta\tau = 0, \pm 2$ and $\Delta\sigma = 0, \pm 2$ [112].

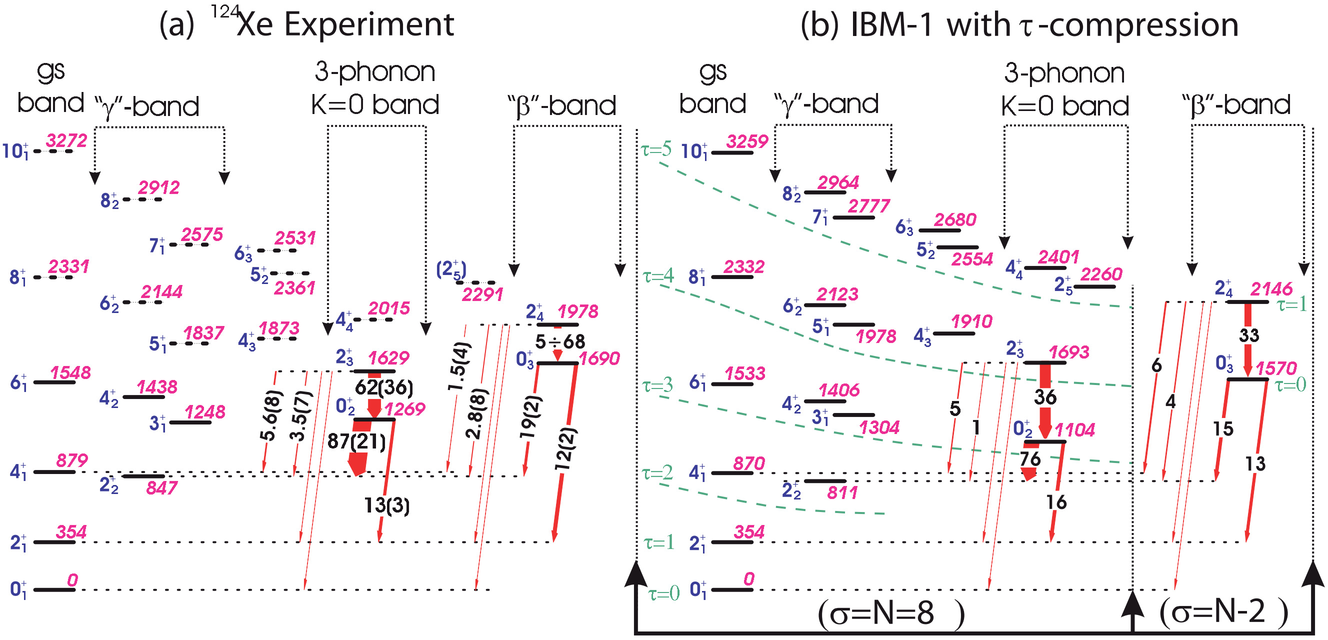

Figure 7.6: (a) Low-energy positive-parity levels of ^{124}Xe. Levels observed in the present experiment are represented by solid lines. (b) sd-IBM-1 calculation for ^{124}Xe [102]. The eigenstates are arranged in (τ, σ) multiplets according to the O(6) dynamical symmetry, as suggested in Ref. [102]. Since in Ref. [102] the σ quantum numbers are assigned tentatively, they are presented in parentheses. The arrows represent the $E2$ transitions of off-yrast, quasi-$K = 0$ levels of particular interest. The thickness of the arrows and the numbers associated with them (for transitions with $B(E2) \geq 1$ W.u.) are the absolute $B(E2)$ values in W.u.

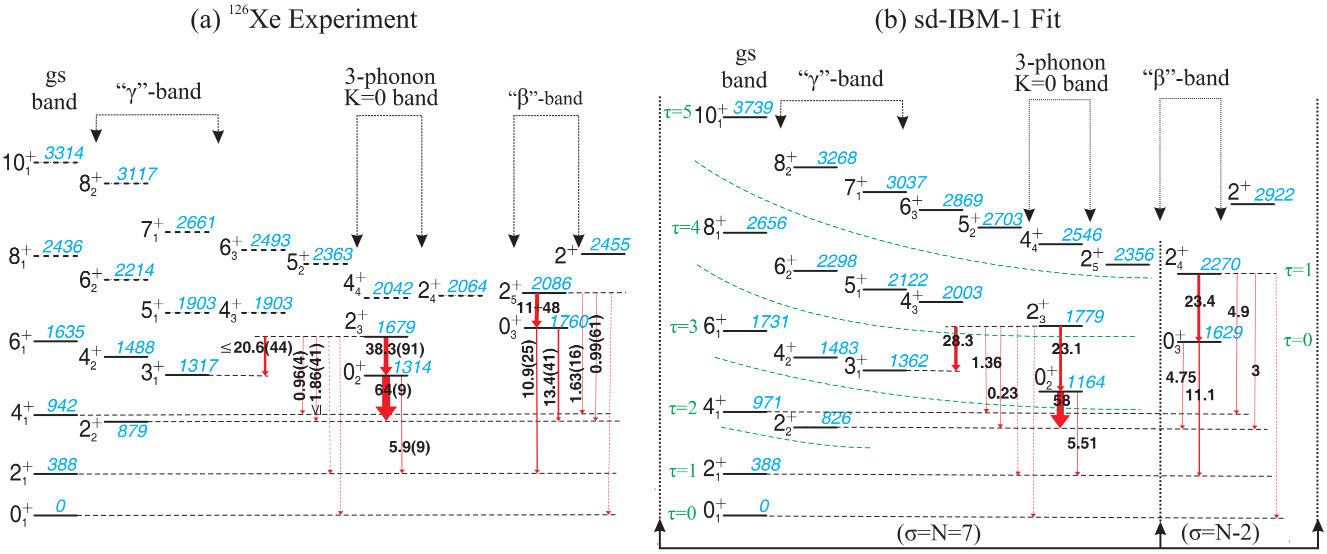

Figure 7.7: (a) Low-energy positive-parity levels of ^{126}Xe. Levels observed in the present experiment are represented by solid lines. (b) sd-IBM-1 calculation for ^{126}Xe (see text). The eigenstates are arranged in (τ, σ) multiplets according to the O(6) dynamical symmetry. The arrows represent the $E2$ transitions of off-yrast, quasi-$K = 0$ levels of particular interest. The thickness of the arrows and the numbers associated with them are the absolute $B(E2)$ values in W.u. The dashed arrows are transitions with $B(E2) \leq 0.1$ W.u.

in the decay of the 2_3^+ state are forbidden in the exact O(6) symmetry and, indeed, their experimental $E2$ strengths are weak. Moreover, the absolute $B(E2)$ values for these transitions clearly reflect the degree of τ-forbiddenness.

The $2_3^+ \rightarrow 0_1^+$ transition, which corresponds to $\Delta\tau = 4$, is about two and three orders of magnitude weaker than the allowed $2_3^+ \rightarrow 0_2^+$ decay for ^{124}Xe and ^{126}Xe respectively while, for the $\Delta\tau = 2$ transitions, this suppression factor is about 10 and 25, respectively (see Fig. 7.6 and 7.7(a)). Altogether, the decay of the 2_3^+ state illustrates the degree of realization of the O(5) selection rules for $E2$ transitions between highly excited, off-yrast states rather well. In terms of the geometrical collective model [31], the 0_2^+ and the 2_3^+ states can be considered as the head and the first member of the quasi-($K = 0$) three-quadrupole phonon band. The absolute $B(E2)$ value between them is a measure of the collectivity in this excited $K = 0$ band. In the case of ^{124}Xe and ^{126}Xe, the results indicate (see Tables 7.1, 7.3) that the collectivity is comparable to that of the ground state band.

In ^{124}Xe, the $B(E2)$ value for the $4_1^+ \rightarrow 2_2^+$ transition (albeit with a large uncertainty) represents the largest deviation between the $E2$ data on ^{124}Xe and the O(5) selection rules for levels corresponding to $\sigma = N$. However, this transition has not been observed directly (see Table 7.1), but was inferred instead (with a large uncertainty) from the CE yield of the 4_1^+ state, assuming that a direct $E4$ population from the ground state is not larger than 26 W.u.(E4).

With the 0_3^+ and 2_5^+ states in ^{124}Xe and the 0_3^+ and 2_5^+ states in ^{126}Xe, the data include a level structure that does not fit into the $\sigma = N$ O(6) family. At first glance, it is tempting to interpret this structure as the bottom of the excited O(6) family with $\sigma = N - 2$. If this interpretation was correct, the $E2$ decays of these levels to the lower lying structure with $\sigma = N$ would be forbidden, due to the O(6) selection rules. However, from the Coulomb excitation yields in ^{124}Xe, $E2$ transition rates of 11.9(17) W.u. and 18.5(17) W.u. follow for the decays of the 0_3^+ state at 1690 keV to the 2_1^+ and 2_2^+ levels, respectively. Similarly in ^{126}Xe, the same behavior is observed with $E2$ transition rates of 10.9(25) W.u. and 13.4(41) W.u. for the decays of the 0_3^+ state at 1760 keV to the 2_1^+ and 2_2^+ levels, respectively. These $E2$ strengths are mildly collective, at least; an observation in severe conflict with the exact O(6) selection rules. Therefore, we must conclude that, for ^{124}Xe and ^{126}Xe, the O(6) symmetry appears to be severely broken rather than somewhat perturbed, as has been assumed before.

The qualitative analysis of the decay rates shows that the new data on the absolute $E2$ strengths in ^{124,126}Xe agree to a large extent with the $\Delta\tau = \pm 1$ selection rules, but are in severe conflict with the $\Delta\sigma = 0$ selection rules. This fact leads to the hypothesis that the O(5) symmetry is predominantly preserved while the O(6) symmetry is broken in ^{124,126}Xe. As a consequence, it is incorrect to use the σ quantum number to label the states. For the purpose of the discussion from this point on we will refer to the structures built on the 0_1^+, 2_2^+, 0_2^+ and 0_3^+ states as the ground state band, the quasi-γ band, the quasi-($K = 0$) three-quadrupole phonon band and the quasi-β band, respectively, as indicated on the top of Fig. 7.6 and Fig. 7.7.

At this point of the discussion we are left with the following questions: Do the new experimental data on absolute transition strengths for the decay of the structure based on the 0_3^+ state of ^{124,126}Xe fit at all into a consistent sd-IBM-1 description of this nucleus? If so, what is the amount of O(6) symmetry breaking in these two nuclei?

According to [21], there are two main differences between the pure theoretical O(6)-limit of the IBM model, experimentally reproduced in ^{196}Pt [113] and the O(6)-like nuclei in the mass region $A = 130$. The first difference results in the staggering of the quasi γ-band: the observed staggering is smaller than the expected one in the O(6)-limit which leads to the conclusion that the collective potential is not completly γ-independent as explained in [21]. The second deviation from the exact O(6)-limit is the smaller spacing between high τ-states than expected according to $E(\tau) \sim \tau(\tau + 3)$ in the O(6) symmetry. This is the so called τ-compression effect which results from the pairing interaction [116]. In order to reproduce the experimental data (staggering in γ-band as well as spacing between the high τ-states), the Hamiltonian of the Extended Consistent Q Formalism (ECQF), has been modified, exactly as described in [102]. Consequently, the modified O(6) Hamiltonian contains two terms, one (L.L) term to correct for the staggering of the quasi γ-band, and one proportional to the O(5) Casimir operator $C_2[O(5)]$ to allow n_d as an independant τ-compressor. The complete sd-IBM-1 Hamiltonian for our calculation is then (the index W refers for Werner since this sd-IBM-1 Hamiltonian corresponds to the one used in [102]):

$$H_W = \epsilon n_d + \lambda LL + \kappa Q^\chi Q^\chi + \beta C_2[O(5)] \tag{7.1}$$

$$H_W = \kappa \left[\frac{\epsilon}{\kappa} n_d + \left(\frac{\lambda}{\kappa} + \frac{2}{5} \frac{\beta}{\kappa} \right) LL + Q^\chi Q^\chi + 4 \frac{\beta}{\kappa} T^{(3)} T^{(3)} \right], \tag{7.2}$$

and in terms of s- and d-bosons the quadrupole operator Q^χ is given by:

$$Q^\chi = s^+ \tilde{d} + d^+ s + \chi [d^+ \tilde{d}]^{(2)}. \tag{7.3}$$

Finally, the E2 transition operator is defined within the ECQF as:

$$T(E2) = e_B Q^{\chi}. \tag{7.4}$$

The diagonalization of the Hamiltonian has been done using the code PHINT of O. Scholten [117]. The way how to find the free parameters of the Hamiltonian is briefly explained here. The reader is referred to Ref. [102] for further details. The Hamiltonian of Eq. 7.2 is a particular case of the Hamiltonian of Eq. 3.17. A very useful Table linking the different parameters of the different versions of the IBM Hamiltonian (sometimes very confusing) of Eq. 3.10, 3.17, 3.21 is given in Ref. [118]. Using Eq. 3.38, one knows for example that E(8_1^+)-E(5_1^+)= 84γ, the relation between the parameter γ and the parameters used in Eq. 3.17 is given in [118] and leads to the determination of λ/κ. Similarly, the other free parameters ($\epsilon/\kappa, \beta/\kappa, \chi, \kappa, e_B$) have been fitted to experimental data: β/κ reproduces the energy spacing in the ground state band, ϵ/κ and χ were adjusted according to the two $B(E2)$ ratios:

$$R_\gamma = \frac{B(E2; 2_2^+ \to 0_1^+)}{B(E2; 2_2^+ \to 2_1^+)}, R_\beta = \frac{B(E2; 0_2^+ \to 2_1^+)}{B(E2; 0_2^+ \to 2_2^+)}. \tag{7.5}$$

The absolute scale parameter κ and the boson effective charge e$_B$ were fixed to reproduce the energy and the $E2$ transition strength of the 2_1^+ state. The last ambiguity was the sign of the χ parameter. In ^{124}Xe, it was chosen to be negative in Ref. [102]. However, it was chosen to be positive for ^{126}Xe. As a first step we compared the Coulex yields predicted by the IBM with our experimental data. This has been done for the two possible solutions: $\chi < 0$ and $\chi > 0$. Note that within the IBM, the sign of χ does not influence the energy levels but the signs of the matrix elements and therefore the corresponding calculated yields. For better visibility we restrict the γ-ray yields plotted on Fig. 7.8 to those stemming from the $2_{1,2,3}^+$ states. In the case of $\chi < 0$, a $B(E2; 3_1^+ \to 2_1^+)$=10.1 W.u value and a $B(E2; 3_1^+ \to 2_2^+)$=624 W.u value were necessary to reproduce the experimental yields of the 3_1^+ state contrary to $B(E2; 3_1^+ \to 2_1^+)$=0.90(23) W.u and $B(E2; 3_1^+ \to 2_2^+)$=55.7(63) W.u for the case $\chi > 0$. Other $B(E2)$ IBM predictions were similar in both cases in order to reproduce the experimental yields. This permitted us to rule out the case $\chi < 0$. The final set of parameters for ^{124,126,128}Xe is given in Table 7.4.

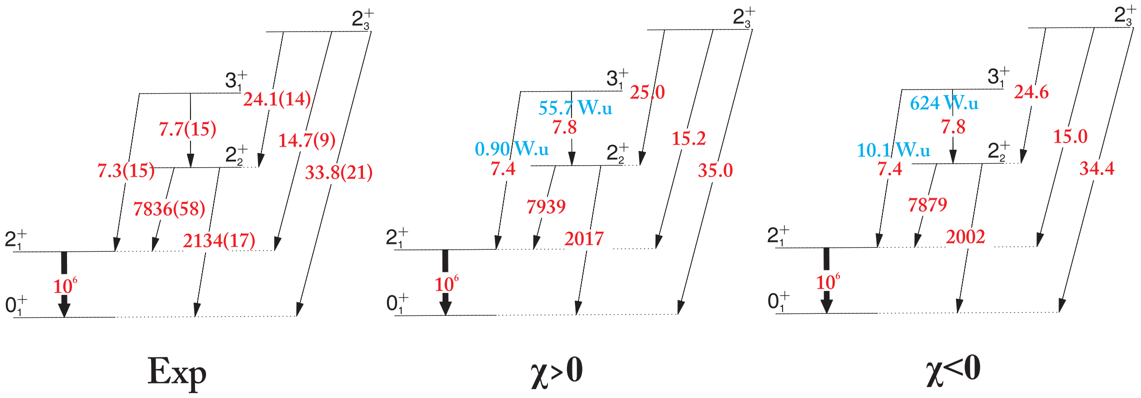

Figure 7.8: Comparison between the experimental yields of ^{126}Xe (Exp) with the Coulex yields predicted by the IBM calculations for the two cases: $\chi > 0$ and $\chi < 0$. Due to extremly large $B(E2)$ values in the case $\chi < 0$ to reproduce the experimental yields of the 3_1^+ state, this solution has been excluded. For more details, see text.

Table 7.4: Parameters used in the τ-ECQF Hamiltonian for ^{128,126}Xe and comparison with the parameters found in [102] for ^{124}Xe.

	ϵ/κ	χ	β/κ	λ/κ	κ [keV]	e$_B$ [eb]
^{128}Xe	-16.8	+0.173	0.76	-0.245	-53.0	0.1153
^{126}Xe	-17.0	+0.180	0.55	-0.322	-41.9	0.12246
^{124}Xe	-20.9	-0.257	0.563	-0.284	-34.91	0.14224

The results from these numerical IBM calculations are presented in the right-most column in Table 7.1 and Table 7.3 for ^{124}Xe and ^{126}Xe, respectively. Except for the $2_1^+ \rightarrow 0_1^+$ transition, the calculated absolute $E2$ transition strengths must be considered as predictions. The agreement between the calculated and the experimental $B(E2)$ values is strikingly good for all observed $E2$ transitions.

In order to document the noteworthy good agreement between the theoretical predictions (outside of any dynamical symmetries) and the data on absolute $E2$ transition rates, we draw attention to the decays of the excited quasi-($K=0$) structures (see Fig. 7.6 and Fig. 7.7). The $E2$ decay strengths of the 0_2^+ and 2_3^+ head and first member states of the 3-phonon K=0 band have been correctly predicted by the IBM, *i.e* in both nuclei, collective $E2$ transitions for the $2_3^+ \rightarrow 0_2^+$, $2_3^+ \rightarrow 3_1^+$ and $0_2^+ \rightarrow 2_2^+$ decays ($\Delta\tau = \pm 1$) and weak $E2$ transitions from 2_3^+ state to other states lower than 0_2^+ state and for the $0_2^+ \rightarrow 2_1^+$ decay ($\Delta\tau = \geq 1$). The transitions from the head and first member of the β-band (0_3^+ and 2_4^+ states in ^{124}Xe while 0_3^+ and 2_5^+ states in ^{126}Xe) can also be well predicted by the IBM calculations eventhough the collective $2_4^+ \rightarrow 0_3^+$ (^{124}Xe) or the $2_5^+ \rightarrow 0_3^+$ (^{126}Xe) transition have not been observed. Note that in ^{126}Xe, the 2_5^+ state from our experiment corresponds to the 2_4^+ state proposed by the IBM. The labels of the 2_4^+ and 2_5^+ states at respectively 2064 keV and 2086 keV are different: one should be the lowest state of the $(\sigma,\tau) = (N,5)$ multiplet and the other one should correspond to the $(\sigma,\tau) = (N-2,1)$ state. In our experiment, we have not observed the 2_4^+ state which is known to exist at 2064 keV. We have however observed the 2_5^+ state at 2086 keV. This state decays to the 4_1^+ and 2_2^+ states, ressembling the decay of the $(\sigma,\tau) = (N-2,1)$ state. A similar decay was for the 2_4^+ IBM state (Fig. 7.7). Therefore we assumed that the 2_5^+ state from our experiment corresponds to the 2_4^+ state proposed by the IBM. In ^{124}Xe and ^{126}Xe, the 2_3^+ state at 1629 keV and 1679 keV, respectively decay to the 0_2^+ level with a collective $E2$ transition in agreement with the predictions of the IBM. The 2_4^+ state at 1978 keV in ^{124}Xe and at 2066 keV in ^{126}Xe are observed to decay by weak transitions to the levels below the 0_3^+ state, again in agreement with the IBM results. The IBM calculations predict a collective $2_4^+ \rightarrow 0_3^+$ $E2$ transition with a strength well within the experimentally estimated limits for both nuclei. We conclude that the structure built on top of the 0_3^+ state of ^{124,126}Xe is accounted for well within the framework of the general sd-IBM-1 in a consistent way, as are the other lower-lying collective excitations. The quantitative agreement between the experimental energies and $B(E2)$ values and the IBM calculations indicates that quadrupole collectivity persists, even for off-yrast states, to quite high excitation energy in ^{124,126}Xe.

The present sd-IBM calculation also makes apparent the breaking of the O(6) symmetry observed in the experimental data. To illustrate this fact, we have projected the wave functions of the first few 0^+ and 2^+ IBM states to the O(6) basis $\{| J^{\pi}\rangle^{(\sigma,\tau)}\}$. These results are presented in Fig. 7.9 (^{124}Xe) and Fig. 7.10 (^{126}Xe). It is obvious that neither τ nor σ are perfect quantum numbers, of course. However, τ quantum numbers are usually quite well preserved which indicates that O(5) is a relevant symmetry. The components with “correct” τ quantum number exhaust about 70% or more of the total wave functions in ^{124}Xe and of about 90% in ^{126}Xe. The small admixtures with different τs are such that the deviations from the O(5) selection rules can easily be explained. For example, the wave function of the 0_2^+ state, the band head of the three phonon $K=0$ structure [Fig. 7.6(b) and Fig. 7.7(b)], contains a small component with $(\sigma = N, \tau = 0)$ which has an amplitude of about 3.4% [see Fig. 7.9(a)] in ^{124}Xe and 1.4% [see Fig. 7.10(left)] in ^{126}Xe. This component makes possible an allowed ($\Delta\sigma = 0, \Delta\tau = -1$) $E2$ transition to the main component of the 2_1^+ state which has the “correct” $(\sigma = N, \tau = 1)$ quantum number. In the same time, the main component of the 0_2^+ state with $(\sigma = N, \tau = 3)$ quantum numbers can make an allowed transition to the component of the 2_1^+ state with $(\sigma = N, \tau = 2)$.

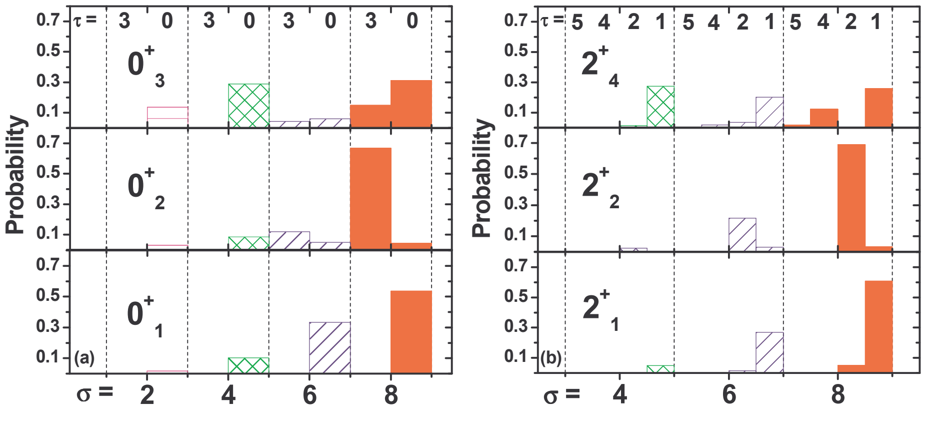

Figure 7.9: Squared amplitudes of the components with different (σ,τ) values of the $0^+_{1,2,3}$ (a) and the $2^+_{1,2,4}$ (b) sd-IBM-1 wave functions for ^{124}Xe.

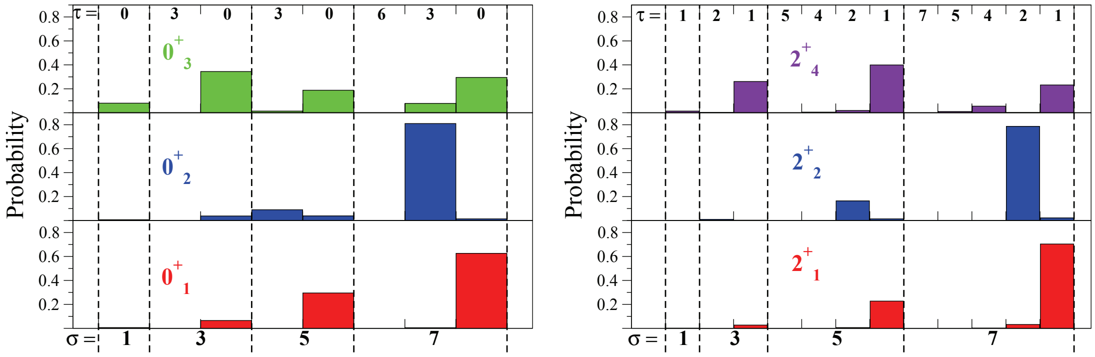

Figure 7.10: Squared amplitudes of the components with different (σ,τ) values of the $0^+_{1,2,3}$ (left) and the $2^+_{1,2,4}$ (right) sd-IBM-1 wave functions for ^{126}Xe.

Analogously, the components with $(\sigma = N-2, \tau = 0)$ and $(\sigma = N-4, \tau = 0)$ of the 0^+_2 state can make allowed transitions to the components with $(\sigma = N-2, \tau = 1)$ and $(\sigma = N-4, \tau = 1)$ of the 2^+_1 state (see Fig. 7.9 and Fig. 7.10). All these $\Delta\tau$ allowed contributions may add up and result in the mildly collective $0^+_2 \rightarrow 2^+_1$ transition which is observed experimentally (see Fig. 7.6(a) and Fig. 7.7(a)). In the same way the small components with “incorrect” τ and σ in the wave functions of the 0^+_3 and the 2^+_1 IBM states are the main reasons for the existence of the otherwise forbidden transition $0^+_\beta \rightarrow 2^+_1$ while main contributions to the collective $E2$ transition between the 2^+_4 and the 0^+_3 states come mostly from components with $\Delta\tau = \pm 1$. The σ quantum numbers are, however, totally dispersed (see Figs. 7.9, 7.10). Even the ground state contains only 53.5% of $\sigma = N = 8$ in ^{124}Xe and 63.1% of $\sigma = N = 7$ in ^{126}Xe. For the states which were thought to belong to the $\sigma = N-2$ representation, the 0^+_3 and the 2^+_4 levels, the σ quantum number is completely diluted. In fact, the components with $\sigma = N-2$ account only for 25.9 % and 10.2 % of the total wave functions of these IBM states in ^{124}Xe and for 20.2 % and 42.3 % in ^{126}Xe (see Fig. 7.9 and Fig. 7.10). While the IBM is very well suited to describe the γ-soft nuclei in the $A \approx 130$ mass region, the present calculations also confirm our conclusion that the nuclei ^{124,126}Xe lie outside the region of O(6) symmetry.

In order to quantify to what extent the dynamical symmetries break down in ^{124}Xe and ^{126}Xe, we investigated the fluctuations in the quantum number of states, defined as $\Delta q = \sqrt{\langle q^2\rangle - \langle q\rangle^2}$, where q represents the quantum number related to the symmetry under consideration. An analysis of the quantum-number fluctuations is preferable over the conventional analysis of the wave function amplitudes which has been done above, because it provides one number which is independent of the basis representation. This number enables us to compare the realization of a symmetry in different dynamical systems on a quantitative basis. In a case of exact symmetry, Δq is 0. All the other cases represent a broken-symmetry situation. It is tempting to classify those using Δq. The scale of such classification depends on the minimum step the quantum number q can change by, denoted δq_{min}. In order to motivate a reasonable classification scheme, we have assumed that, for broken symmetries, the quantum numbers are normally distributed. Then the case of broken symmetry can be subdivided on two cases depending on how the Full-Width-Half-Maximum (FWHM) of the distribution of quantum numbers q compares to the δq_{min}. If FWHM$\leq \delta q_{min}$ we consider the broken symmetry to be *perturbed* only, otherwise (FWHM $> \delta q_{min}$) the symmetry is considered *dissolved*. However, in the case of a normal distribution, the quantum-number fluctuation is equal to the standard deviation of the normal distribution. This allows the above definition of perturbed and dissolved symmetry to be refined by introducing a classification value $\Delta q_{class.} \equiv \delta q_{min}/(2\sqrt{2ln2})$. We consider the symmetry to be *perturbed*, but *dominant*, if the fluctuations in the quantum number is $\Delta q \leq \Delta q_{class.}$, otherwise $(\Delta q > \Delta q_{class.})$ we consider the symmetry related to this quantum number to be *dissolved*. For example, the quantum number σ changes with a minimum step $\delta\sigma_{min} = 2$. Then, the classification value for the fluctuations in the σ quantum number is $2/(2\sqrt{2ln2})$. If the fluctuations in the σ quantum number are larger than 0.849, we consider the O(6) symmetry dissolved in the state of interest.

Since the Δq values are related to the detailed structure of the wave functions, they impact the $E2$ transition rates directly. In order to disentangle the influences of different symmetries, states whose decay is sensitive to a particular selection rule have to be chosen. In the case of ^{124,126}Xe, the band heads of the quasi-β structure and the quasi-γ structure are the obvious choices. In terms of the O(6) selection rules, the $2^+_\gamma \rightarrow 0^+_1$ transition is σ-allowed and τ-forbidden, while the $0^+_\beta \rightarrow 2^+_1$ is a σ-forbidden-τ-allowed transition. We traced the evolution of the $B(E2;2^+_\gamma \rightarrow 0^+_1)/B(E2;2^+_1 \rightarrow 0^+_1)$ and the $B(E2;0^+_\beta \rightarrow 2^+_1)/B(E2;2^+_1 \rightarrow 0^+_1)$ ratios as functions of $\Delta\tau$ and $\Delta\sigma$ on the trajectory through the parameter space of the IBM-1 from the exact O(6) symmetry to the point defined by the model parameters fitted here in the same way as in Ref. [102] (indexed here with the subletter W) (see Fig. 7.11 and Fig. 7.12). This trajectory is defined by the Hamiltonian (7.2) with the following parametrisation:

$$\begin{gathered}\beta(a) = \beta_{O(6)} + a(\beta_W - \beta_{O(6)})\\ \epsilon(a) = \epsilon_W a\\ \chi(a) = \chi_W a\\ \kappa(a) = cst = \kappa_W\\ \lambda(a) = cst = \lambda_W .\end{gathered}$$

The parameters with a subscript index W, refers to the parameters listed in Table 7.4. The parameters λ and κ do not change the wave functions. Therefore they have been arbitrarily fixed in the parametrisation to the values from Table 7.4. Obviously, when $a = 1$ the above parametrisations represent exactly the original Hamiltonian H_W used in Ref. [102] or Eq. 7.2, while, in the case of $a = 0$, the above parametrisations represent an IBM Hamiltonian in the exact O(6) symmetry. The parameter $\beta_{O(6)} = -0.455$ keV, was chosen to produce the head of the $\sigma = N - 2$ structure as the third 0^+ state in the exact O(6) symmetry ($a = 0$). From this point on, this 0^+ state was traced on the basis of its unique feeding and decay pattern to the 0^+_3 which results from the sd-IBM-1 calculation ($a = 1$). No crossings with other 0^+ states were observed on the way. A comparison between the resulting evolution of the $B(E2; 0^+_\beta \to 2^+_1)/B(E2; 2^+_1 \to 0^+_1)$ ratio and the experimental value in ^{124,126}Xe [Fig. 7.11 (a) and Fig. 7.12 (a)] provides

$$\boxed{\Delta\sigma_{exp}(0^+_3; {}^{124}\text{Xe}) = 2.29^{+0.07}_{-0.11}}$$

$$\boxed{\Delta\sigma_{exp}(0^+_3; {}^{126}\text{Xe}) = 2.03^{+0.08}_{-0.16}}.$$

These 2 values are well beyond the classification value of 0.849. In Fig. 7.11 (a) and Fig. 7.12 (a), the fluctuations in the σ quantum number for the other dynamical symmetries, U(5) and SU(3), are also presented. Both of them are above the classification value which demonstrate the usefulness of such a criteria for quantifying the degree of O(6) symmetry breaking. The obtained value of $\Delta\sigma_{exp}$ for the 0^+_β state of ^{124,126}Xe not only confirm our previous conclusion that the O(6) symmetry is broken, but also indicates that the degree of breaking is comparable to the one in the other dynamical symmetries, *i.e.* in ^{124,126}Xe the O(6) symmetry is actually completely dissolved. An analogous analysis for the $B(E2; 2^+_\gamma \to 0^+_1)/B(E2; 2^+_1 \to 0^+_1)$ ratio tells a different story for the O(5) symmetry [Fig. 7.11 (b) and Fig. 7.12 (b)]; even though the experimental ratio is close to the ratio corresponding to the maximum possible fluctuations in the τ quantum number on the trajectory we have investigated (afterwards it bends back down), it is still well below the classification value $\Delta\tau_{class.} = 1/(2\sqrt{2ln2})$=0.425.

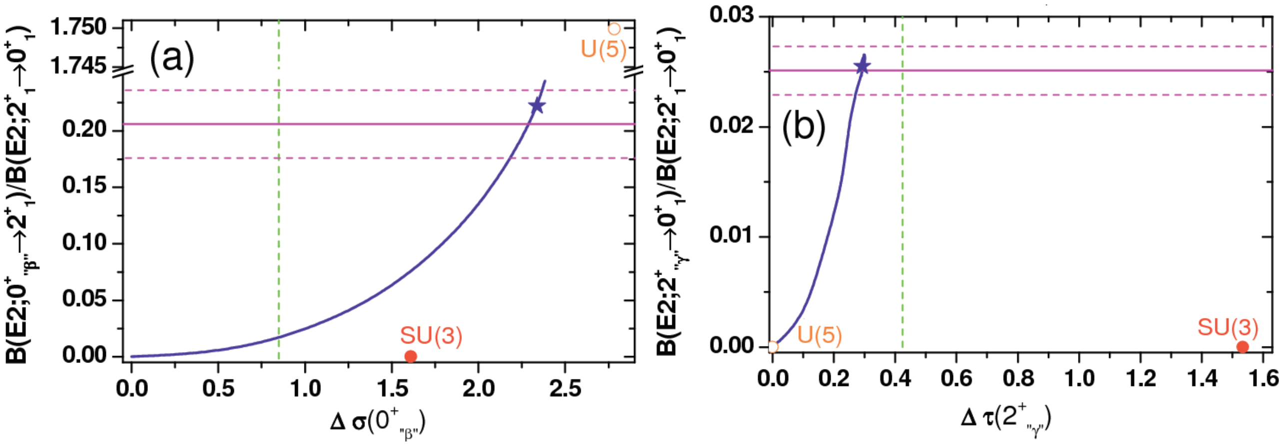

Figure 7.11: Evolution of the $B(E2; 2^+_\beta \to 2^+_1)/B(2^+_1 \to 0^+_1)$ (a) and the $B(E2; 2^+_\gamma \to 0^+_1)/B(2^+_1 \to 0^+_1)$ (b) ratios as functions of $\Delta\sigma$ and $\Delta\tau$ (solid curves) on the linear trajectory from the exact O(6) symmetry to the point defined by the IBM parameters of Ref. [102] (stars). The vertical dashed lines represent the classification values of $\Delta\sigma$ and $\Delta\tau$ beyond which the respective symmetry is dissolved. The circles represent the values of the respective ratios and the fluctuations at U(5) (open circles) and SU(3) (filled circles) dynamical symmetries of IBM. The horizontal lines represent the experimental values in ^{124}Xe.

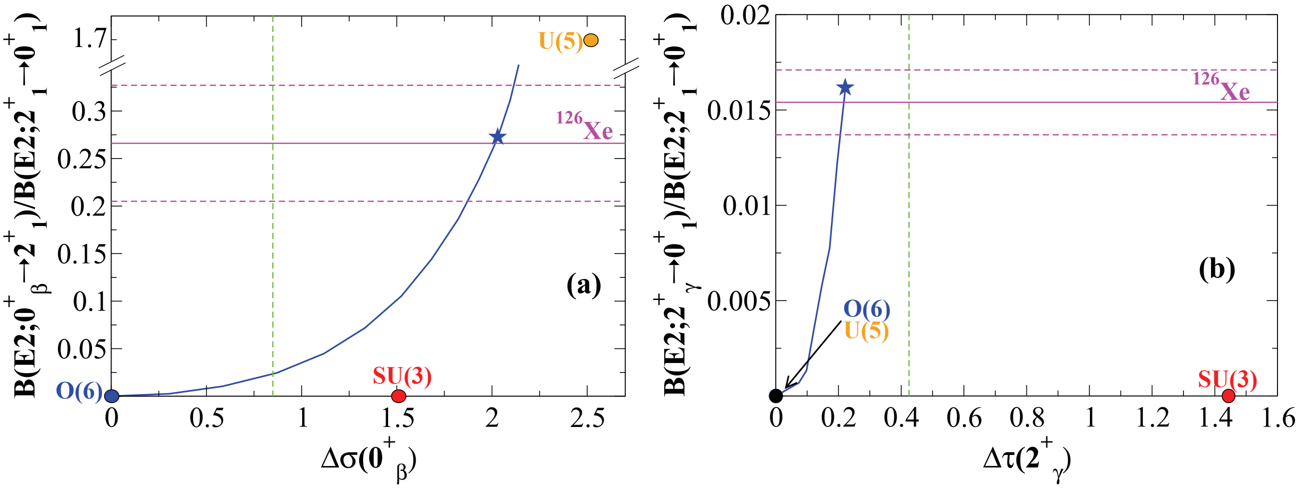

Figure 7.12: Evolution of the $B(E2;2^+_\beta \to 2^+_1)/B(2^+_1 \to 0^+_1)$ (a) and the $B(E2;2^+_\gamma \to 0^+_1)/B(2^+_1 \to 0^+_1)$ (b) ratios as functions of $\Delta\sigma$ and $\Delta\tau$ (solid curves) on the linear trajectory from the exact O(6) symmetry to the point defined by the IBM-1 parameters described in this work (stars). The vertical dashed lines represent the classification values of $\Delta\sigma$ and $\Delta\tau$ beyond which the respective symmetry is dissolved. The circles represent the values of the respective ratios and the fluctuations at U(5) and SU(3) dynamical symmetries of IBM. The horizontal lines represent the experimental values in ^{126}Xe.

The experimental values of

$$\boxed{\Delta\tau_{exp}(2^+_2;{}^{124}\mathrm{Xe}) = 0.292(22)}$$

$$\boxed{\Delta\tau_{exp}(2^+_2;{}^{126}\mathrm{Xe}) = 0.221(14)}$$

indicate that the O(5) symmetry is only slightly perturbed. Indeed, this value is closer to 0, where the value for fluctuations in the τ quantum numbers for the U(5) symmetry abides (U(5) includes O(5) symmetry, *i.e.*, no fluctuations in the τ quantum number are present in U(5) symmetry) than to the value for the fluctuations expected at the SU(3) symmetry, which is well beyond the classification value of 0.425 [see Fig. 7.11 (b) and Fig. 7.12 (b)]. We stress that such an analysis is made possible only by the comprehensive set of absolute values of $E2$ transition rates available from the present projectile Coulomb excitation measurements on a light target.

In summary, we have studied ^{124,126}Xe using projectile Coulomb excitation. The data yield 47 absolute $E2$ transition strengths between low spin states. The experimentally observed level energies, branching ratios and the absolute transition strengths are reproduced well by an sd-IBM-1 calculation [102] outside of the O(6) dynamical symmetry. The new data allow the symmetry breaking to be investigated by relating the fluctuations in the quantum numbers directly to the experimental observables. Using this approach, we have quantitatively shown that, in ^{124,126}Xe, the O(6) symmetry is completely dissolved while the O(5) symmetry is only slightly perturbed. It is therefore important the issue to be investigated further which requires more $E2$ transition rates for high-lying off-yrast states of nuclei that are currently being viewed as close to the O(6) symmetry be measured and analysed with the method we have proposed here. Clearly ^{196}Pt becomes a very interesting case.

7.4 ^{128}Xe: Robust test of the E(5) symmetry

Details about the experiment can be found in section 6.1. The singles spectrum Doppler corrected (recoiling velocity β=6.5(2)%) and time random background subtracted is displayed in Fig. 7.13. The total number of events was 1.0×10^9 for a running time of $\sim$ 23h. Approximately 1.7×10^7 events of γ-ray fold higher than 1 were collected and sorted into a $\gamma\gamma$-coincidence matrix. All the γ-transitions observed were placed in the level scheme of ^{128}Xe and are plotted in Fig. 7.14. Their corresponding intensities are listed in Table 7.6. Information on these levels was reported previously in Refs. [126, 127, 119, 115, 42]. Population of each state have been deduced from γ-singles and $\gamma\gamma$-coincidence data (Fig. 7.13). For unobserved transitions (e.g energy too small or contaminated lines), their contributions have been determined from the previously known branching ratios from Ref. [128]. In order to minimize systematical uncertainties, the γ-ray yields have been normalized to the $2_1^+ \rightarrow 0_1^+$ transition, which predominates the spectrum by three orders of magnitude. The γ-ray yields normalized to the intensity of the $2_1^+ \rightarrow 0_1^+$ transition (Table 7.6) measure the relative Coulomb Excitation (CE) cross sections. The contribution from the electron conversion decays to the populations of the states are negligible according to [131]. The multiple CE code CLX, based on the Winther-De Boer theory [77] has been used to determine the set of matrix elements reproducing the experimental normalized yields. The fit was made by using the previously well known $B(E2; 2_1^+ \rightarrow 0_1^+) = 0.1650(24)\ e^2b^2$ from [105] as well as considering the energy loss of the beam inside the target (about 40 MeV). The signs of the matrix elements have been chosen as the corresponding one proposed by an IBM-1 calculation and are also given in Table 7.6. The parameters of the IBM-1 calculation are listed in Table 7.4. Details concerning the IBM-1 fit are given in section 7.3. For more details concerning the CLX analysis (energy loss, constraints, quadrupole moments, relative phases), see section 6.2.5. Our analysis resulted in 19 absolute and 7 upper limits for $B(E2)$ values, 8 values and 3 upper values for the lifetimes (τ), which are listed on Table 7.6 and Table 7.7, respectively.

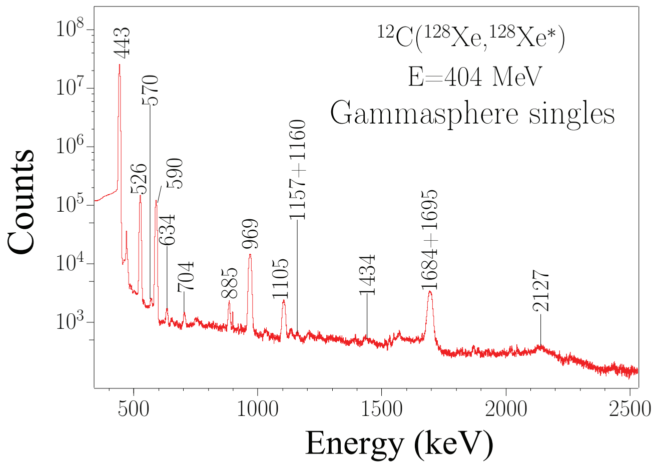

Figure 7.13: Background-subtracted and Doppler-corrected single γ-ray spectra for the sum over all Ge detectors of Gammasphere after the Coulomb excitation of ^{128}Xe on a carbon target.

- **2_1^+ state at 442.9 keV**
  The spectrum of Fig. 7.13 is dominated by the 443-keV line from the 2_1^+ state to the ground state with about 5.07×10^8 counts. The corresponding angular distribution with its respective coefficients $a_2 = A_2/A_0$ and $a_4 = A_4/A_0$ is given in Fig. 6.11.

- **2_2^+ state at 969.5 keV**
  The angular distributions coming from this state with their respective coefficients $a_2 = A_2/A_0$ and $a_4 = A_4/A_0$ are given in Fig. 6.11. A value of $\delta = +6.06^{+13}_{-11}$ has been deduced. This value is in agreement with the previously known $\delta = +4.4(7)$ value from Ref. [128]. However the CLX calculations have been made by using the $\delta = +4.4(7)$ value. Both δ values are large and assign almost a pure $E2$ transition character for the $2_2^+ \rightarrow 2_1^+$ transition (>95%). The 969-keV γ-ray line was a doublet with the 966-keV γ-ray line from the 2_3^+ state at 1999 keV. The individual intensity of the 969-keV γ-ray line has been deduced from the branching ratio from Ref. [128].

- **4_1^+ state at 1033.1 keV**
  The unobserved $4_1^+ \rightarrow 2_2^+$ transistion at 63.6 keV does not play a significant role for the population of the 4_1^+ state

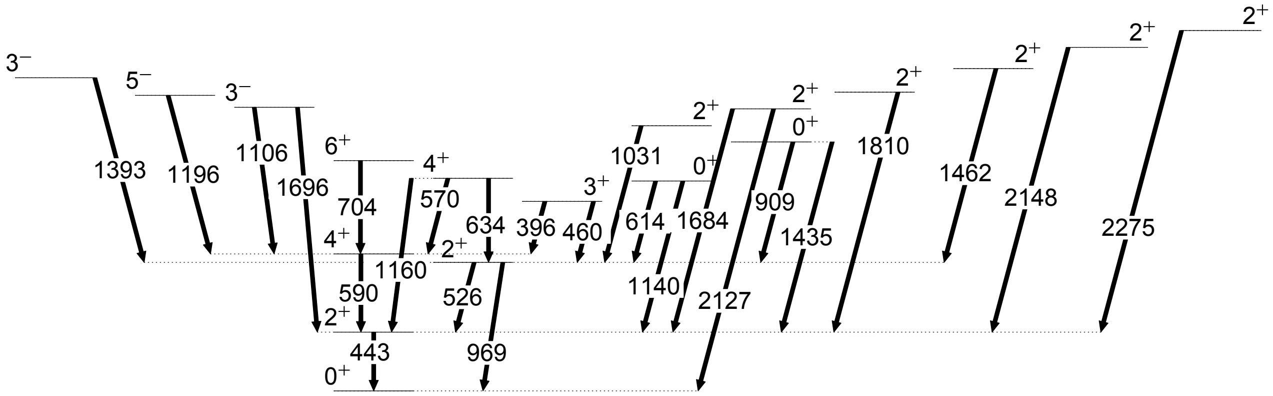

Figure 7.14: Part of the low-spin level scheme of ^{128}Xe showing all levels for which we observed γ-ray transitions in the ^{12}C(^{128}Xe,^{128}Xe*) projectile Coulomb excitation reaction.

at 1033.1 keV. Similarly to the 4_1^+ state in ^{126}Xe, the CLX calculations have been done assuming no $E4$ transition from the ground state to the 4_1^+ state (see section 7.2).

- **2_3^+ state at 1999.6 keV**
  No lines steming from this state have been directly observed. However, the 966.5-keV γ-ray line to the 4_1^+ state is a doublet with the strong 969.5-keV γ-ray line from the 2_2^+ state to the ground state. By fitting the doublet and using the individual intensity of the 969.5-keV γ-ray line, we deduced the normalized intensity of the 966.5-keV γ-ray line [$I(966.5keV) = 33(55)$ counts]. The branching ratios with the other lines steming from the 2_3^+ state are also known (see Table 7.5). Since there was a lot of discrepancies between the different branching ratios found in the literature (Table 7.5, Ref. [128, 126, 130]), the respective individual intensities from the other lines steming from the 2_3^+ state have not been deduced. However, if we suppose the branching ratios from Ref. [126] and Ref. [130] corrects, we should have obtained a normalized intensity for the 1030-keV line of $I(1030) = 206(350)$. Since we did not oberve such a strong line we can only suggest the branchings from Ref. [126] and Ref. [130] are wrong. However since the error is so large, we could have also expected few counts in the 1030-keV γ-ray line that we could not fit. In this sense it was too confusing and not reliable to derive any other intensities steming from the 2_3^+ state at 1999.6 keV.

Table 7.5: Branching ratios steming from the 2_3^+ state at 1999.6 keV in ^{128}Xe.

Transition	Energy [keV]	I$_\gamma$ [128]	I$_\gamma$ [126]	I$_\gamma$ [130]
$2_3^+ \rightarrow 4_1^+$	966.5	100(8)	16(9)	16.9(18)
$2_3^+ \rightarrow 2_2^+$	1030.2	5.1(3)	100(5)	100(3)
$2_3^+ \rightarrow 2_1^+$	1556.7	38.8(25)	6.2(4)	not observed
$2_3^+ \rightarrow 0_1^+$	1999.6	2.3(8)	0.37(12)	not observed

- **2^+ state at 2430.7 keV**
  The mixing ratio from the literature for the $2^+ \rightarrow 2_1^+$ transition is unknown and due to low statistics our data did not enable us to measure it from the angular distributions. In Table 7.6, the $B(E2)$ values from the mixed transitions coming from this state have been calculated by assuming pure $E2$ transitions, hence the upper values. However, if we assume that the $2^+ \rightarrow 2_1^+$ transition is a pure $M1$ transition, we finally obtain $B(M1; 2_3^+ \rightarrow 2_1^+) \leq 0.005(2)\ \mu_N^2$ which supports the fact that the 2^+ state at 2430.7 keV is not a MSS.

- **2^+ state at 2591.6 keV**
  Once again the low statistics of the transitions from this 2^+ state to the 2_1^+ and 0_1^+ states did not allow us to observe any angular distributions and thus no mixing ratio has been measured. Since the mixing ratio for the $2^+ \rightarrow 2_1^+$ is unknown, we assumed a pure $E2$ transition, leading to an upper value $B(E2; 2^+ \rightarrow 2_1^+) \leq 5.3(13)$ W.u.. By assuming that this transition is purely $M1$, we obtain $B(M1; 2^+ \rightarrow 2_1^+) \leq 0.065(16)\ \mu_N^2$. This upper value does not enable us to rule out the mixed-symmetry character of this state. The decay to the ground state is also

weakly collective ($B(E2;2^+ \rightarrow 0_1^+) = 0.98(27)$ W.u. as expected for the MSS. This state could be a candidate for a fragment of the MSS.

- **2^+ state at 2718.5 keV**
  From the same arguments as for the 2^+ state at 2591.6 keV, if we assume that the $2^+ \rightarrow 2_1^+$ is purely magnetic, we obtain $B(M1;2^+ \rightarrow 2_1^+) \leq 0.19(5)\ \mu_N^2$. Once again, it is not possible to affirm the mixed-symmetry character of this state since we are not able to derive the absolute $B(M1;2^+ \rightarrow 2_1^+)$ transition strength. However this upper value does not neither enable us to rule out the 2^+ state as a MSS. The decay to the ground state has a strength of $B(E2;2^+ \rightarrow 0_1^+) = 1.23(51)$ W.u. as might be expected for a fragment of the $2^+_{1,\mathrm{ms}}$ state.

The solutions of the Bohr Hamiltonian for a variety of geometric potentials by Iachello and collaborators [64, 55, 122] has provided considerable new intuitive insight into shape transitions. One transition, the E(5) symmetry [64], reflects the critical point in the shape transition from spherical to γ-soft, O(6)-like nuclei. The shape transitional point and also the E(5) symmetry are characterized by large fluctuations in the quadrupole deformation parameter β and maximum fluctuations in the triaxiality parameter γ. This leads to characteristic ratios between excitation energies of various excited states and between their E2 transition rates. As xenon and barium nuclides are thought to be γ-soft, candidates for E(5) symmetry should be expected in this region as the spherical $N = 82$ shell closure is approached. Casten and Zamfir [123] suggested ^{134}Ba as a possible realization of the E(5) tipping point, based on a few simple experimental signatures such as the $\mathrm{R}_{4/2} = E(4_1^+)/E(2_1^+)$ ratio and the relative excitation energies $\mathrm{R}_{0/2} = E(0_{2,3}^+)/E(2_1^+)$ and E2 decay branching ratios of the first two excited 0^+ states.

Subsequently, Clark *et al.* [124] conducted a systematic search of the nuclear data bases for the occurence of experimental fingerprints of E(5) symmetry. $\mathrm{R}_{4/2}$ and $\mathrm{R}_{0/2}$ ratios pointed at the nucleus ^{128}Xe as another possible realization of E(5) symmetry [124]. This conclusion implies that ^{128}Xe is near the shape phase transition from spherical nuclei around the doubly-closed shell nucleus ^{132}Sn to the deformed γ-soft nuclei that the A≈130 mass region is well known for [21]. In fact, this mass region is considered the largest region of the nuclear chart with γ-soft nuclei. However, the loci of phase transitional lines between spherical and γ-softly deformed nuclei are not yet established in this mass region.

Recently, Bonatsos *et al.* formulated the γ-independent version [65] of the Confined Beta-Soft (CBS) rotor model [60]. That version of the model, called O(5)-CBS, generalizes the E(5) solution near the critical point to a parametric solution for the whole path between E(5) and the β-rigidly deformed γ-independent limit. The structure of ^{128}Xe was investigated in terms of the O(5)-CBS [65]. The decay pattern of the first two excited 0^+ states suggested that ^{128}Xe is already located well beyond the U(5)–to–O(6) shape phase transition in the deformed phase. The previous suggestion by Clark *et al.* for the critical structure of ^{128}Xe was mainly based on relative excitation energies, the absolute $B(E2)$ strengths in the ground state band as well as for the 2_2^+ state, the branching ratio of the 0_2^+ state and the one known branch from the 0_3^+ state (0_3^+ to 2_1^+). In [124], the 0_2^+, 0_3^+ states have been assigned as 0_τ^+, 0_ξ^+ respectively. Bonatsos *et al.* investigated as well the $E2$ decay branching ratio of the 0_3^+ state and found supporting evidence for these assignments. However, the arguments of Bonatsos *et al.* relied on the analysis of E2 γ-ray branching ratios of which at least one had a large experimental uncertainty of about 50%. The E2 branching ratios further suggested that the crucial excited 0^+ states were mixed in a two-state mixing scheme. That scheme lead to a satisfactory description of excitation energies and branching ratios but its consistency with data could not be tested independently without the knowledge of absolute $B(E2)$ values. Due to the importance of the $A \approx 130$ mass region for the issue of a possible U(5)–to–O(6) phase transitional point, it is highly desirable to improve on the uncertainty for the E2 decay branching ratios of excited 0^+ states of ^{128}Xe and even more to gain information on the corresponding absolute B(E2) values for a quantitative test of the arguments made by Bonatsos *et al.* [65]. It is the purpose of this section to report on the results of a measurement of absolute E2 decay strengths from both, 0_2^+ and 0_3^+, lowest-lying excited 0^+ states of ^{128}Xe in order to check quantitatively on the two-state mixing scheme and the structure assignments for the 0^+ states of ^{128}Xe. This section settles the question of whether ^{128}Xe is a strong candidate for a realization of E(5) symmetry.

The obtained comprehensive data set from Table 7.6 can be used for a robust test of the previously debated [124, 65] possible E(5) character of ^{128}Xe. We note that our results are in very good agreement with the previously known $B(E2)$[128], as well as the $B(E3)_\uparrow$ [105], which verifies our normalization procedure. In order to test the E(5) character of ^{128}Xe quantitatively, we focus on sensitive key observables that are listed in Table 7.8 along with the corresponding predictions of relevant models. For further details concerning the different models, the reader is referred to Refs. [64, 124, 65, 125]. An important signature for the E(5) critical point is the ratio $R_{4/2}$. In the case of ^{128}Xe this observable is $R_{4/2}$=2.33 intermediate between the value for E(5) ($\mathrm{R}_{4/2}$=2.20) and the deformed γ-independent limit or O(6) ($\mathrm{R}_{4/2}$=2.50). The $\mathrm{R}_{4/2}$ ratio suggests that ^{128}Xe should lie between E(5) and O(6).

Table 7.6: Measured properties of the levels and γ-ray transitions in ^{128}Xe. The absolute $E2$ strengths are compared to sd-IBM-1 calculations. $B(E2)$ values are given in W.u. (1 W.u.($E2$)=0.0038318 e^2b^2), $B(M1)$ in μ_N^2 and the $B(E3;0_1^+ \rightarrow 3_1^-)\uparrow$ value is given in e^2b^3.

E_{level} (keV)	J^π	E_γ (keV)	I_γ	J^π_{final}	δ[a]	σ	Transition strength Exp.	IBM-1	Lit.[a]
442.9	2_1^+	442.9	10^6	0_1^+		+	42.6(64)[b]	42.6	40.2(21)
969.5	2_2^+	526.5	7271(51)	2_1^+	+4.4(7)	-	50.1(97)	51.6	48(5)
		969.5[d]	1949(39)	0_1^+		+	0.65(8)	0.67	0.64(6)
1033.1	4_1^+	63.6[c]		2_2^+		-		0.04	
		590.2	7043(49)	2_1^+		+	63.5(52)	60.8	59(5)
1429.6	3_1^+	396.3[e]	1.73(27)	4_1^+	+2.8(3)	-	31.8(59)	15.9	
		460.1[f]	9.4(14)	2_2^+	+7.8(8)	+	91(16)	45.4	
		986.6[e]	8.9(14)	2_1^+	+1.7(1)	-	1.45(26)	0.87	
1583.0	0_2^+	613.5[f]	6.1(12)	2_2^+		+	52.8(76)	61.6	
		1140.0[e]	9.5(20)	2_1^+		-	3.69(58)	4.14	
1603.5	4_2^+	570.4	36.2(8)	4_1^+	$+1.9^{0.3}_{0.5}$	+	30.2(32)	25.9	
		634.0	50.4(8)	2_2^+		-	29.6(29)	33.4	
		1160.6[d]	18.2(7)	2_1^+		-	0.52(6)	0.27	
1737.3	6_1^+	704.2	40.7(14)	4_1^+		+	106(13)	65	78(7)
1877.7	0_3^+	908.2[f]	5.4(9)	2_2^+		+	22.2(46)	1.82	
		1434.4	27.8(30)	2_1^+		-	10.4(23)	17.0	
2127.1	2_4^+	1157.5[d]	5.7(18)	2_2^+		+	$\leq$ 0.74(113)[g]	0	0.25(6)
		1684.1[d]	90(32)	2_1^+	+0.08(6)	+	0.035(54)	0.0015	
				2_1^+			$B(M1) = 0.042(12)\ \mu_N^2$		
		2127.1	11.0(13)	0_1^+		+	0.21(7)	0	
2138.7	3_1^-	1105.4	267(3)	4_1^+		+			
		1695.8[d]	861(34)	2_1^+		+			
		2138.7		0_1^+		+	$B(E3)$=0.069(14)[h]		
2165.9		1132.7[d]	16.4(20)	4_1^+					
2229.2	$(5)_1^-$	1196.1[f]	8.9(11)	4_1^+					
2361.6	(3)	1392.1[f]	14.7(11)	2_2^+					
2430.7	2^+	1461.2[f]	6.3(8)	2_2^+		-	$\leq$ 2.30(85)		
				2_2^+			$B(M1) \leq 0.013(5)\ \mu_N^2$		
		1987.8[e]	5.8(5)	2_1^+		-	$\leq$ 0.48(18)		
				2_1^+			$B(M1) \leq 0.005(2)\ \mu_N^2$		
		2430.7[e]	1.3(1)	0_1^+		+	0.15(6)		
2591.6	2^+	1162.0[e]	4.9(8)	3_1^+		+	$\leq$ 22.9(68)		
				3_1^+			$B(M1) \leq 0.082(24)\ \mu_N^2$		
		2148.6[f]	24.4(21)	2_1^+		+	$\leq$ 5.3(13)		
				2_1^+			$B(M1) \leq 0.065(16)\ \mu_N^2$		
		2591.5[e]	2.9(4)	0_1^+		+	0.98(27)		
2718.5	2^+	1749.0[e]	5.2(17)	2_2^+		+	$\leq$ 11.3(47)		
				2_2^+			$B(M1) \leq 0.092(38)\ \mu_N^2$		
		2275.6[f]	23.5(20)	2_1^+		+	$\leq$ 13.8(36)		
				2_1^+			$B(M1) \leq 0.19(5)\ \mu_N^2$		
		2718.5[e]	1.3(4)	0_1^+		+	1.23(51)		

---

[a] From Ref. [128].

[b] From Ref. [105].

[c] This transition is not observed. Contrary to Ref. [89], this transition does not play a relevant role for the population of the 4_1^+ state.

[d] These transitions are doublets, the respective individual intensities have been separated through the known branching ratios from Ref. [128].

[e] These transitions are not observed by us but are included in the calculations for the Coulomb cross-sections. Their intensities are deduced from the previously known branching ratios from Ref. [128].

[f] These transitions were detectable for us only in coincidence spectra.

[g] Upper value for the $B(E2)$ since the mixing ratio was unknown, quoted value obtained by assuming a pure $E2$ transition.

[h] $B(E3)\uparrow$ value given in e^2b^3. In Ref. [105], a $B(E3)\uparrow$= 0.083(11) e^2b^3 value is reported.

Table 7.7: Lifetimes of the low-lying states in ^{128}Xe compared with the previously known values from the literature.

E_{level} (keV)	J^{π}	τ (ps)	τ^{a} (ps)
442.9	2_1^+	$29.4(22)^{b}$	30.7(16)
969.5	2_2^+	8.68(56)	8.22(72)
1033.1	4_1^+	4.70(39)	5.05(43)
1429.6	3_1^+	5.24(42)	$2.3(3)^{c}$
1583.0	0_2^+	1.82(9)	
1603.5	4_2^+	3.31(10)	$3.5(2)^{c}$
1737.3	6_1^+	1.16(7)	1.59(14)
1877.7	0_3^+	0.23(2)	
2127.1	2_4^+	0.17(7)	
2430.7	2^+	$\leq$0.64(15)	
2591.6	2^+	$\leq$0.07(1)	
2718.5	2^+	$\leq$0.02(1)	

---

[a] From Ref. [128].

[b] From Ref. [105].

[c] From Ref. [129].

Other key features of the E(5) critical point symmetry are the properties of the 0_2^+ and 0_3^+ states, that vary along the U(5)-O(6) transition. A major difference between these two limits, besides the relative energies of the multiplets, is the structure of the excited 0^+ states. One of them is a member of the three-phonon multiplet with O(5) quantum number [132, 64] $\tau = 3$ in the entire transition from U(5)-O(6) (denoted 0_τ^+). The other one (denoted 0_ξ^+) evolves from the two-phonon 0^+ state in U(5), with a strong $B(E2; 0_{2ph}^+ \rightarrow 2_1^+)$ value, into the band-head of the $\sigma = N - 2$ family in O(6), where it typically lies higher than the 0_τ^+ state and the $B(E2; 0_{N-2}^+ \rightarrow 2_1^+)$ value vanishes. In fact, these 0^+ states test the softness of the nuclear potential in the quadrupole deformation variables β and γ in a different way. The evolution of these two 0^+ states between E(5) and the rigidly deformed γ-independent rotor limit, which corresponds to the O(6) dynamical symmetry of the IBM for infinite boson number, is predicted by the O(5)-CBS rotor model [65]. In E(5) the 0_ξ^+ state lies below the 0_τ^+ state. With increasing nuclear rigidity the excitation energies relative to the 2_1^+ state, the $R_{0/2}$ values, increase monotonically for both of them. The $R_{0/2}$ value of the 0_ξ^+ state increases more strongly than that of the 0_τ^+ state. Consequently, these levels cross as a function of the rigidity of the nuclear potential in the quadrupole deformation variable β. Eventually the $R_{0/2}(0_\xi^+)$ value becomes infinite towards the rigid limit [65]. All along this evolutionary path the O(5) vibration-like symmetry is preserved and the $\Delta\tau = 2$ $E2$ transitions, $0_\tau^+ \rightarrow 2_1^+$ and $0_\xi^+ \rightarrow 2_2^+$, are forbidden in leading order due to the selection rule $\Delta\tau = \pm 1$ for the $E2$ operator [64, 65, 132]. For the same reason, the $0_\tau^+ \rightarrow 2_2^+$ and $0_\xi^+ \rightarrow 2_1^+$ $E2$ transitions are allowed up to the rigid limit. This suggests a structure assignment to these 0^+ states already from their $E2$ decay branching pattern. In this respect, the relative position of the $0_{\xi,\tau}^+$ states and their absolute $B(E2)$ values are the most sensitive key features of E(5) symmetry (Table 7.8).

Table 7.8: Comparison of key observables in ^{128}Xe: for the experimental values taken from this work and Ref. [128] (^{128}Xe), for the experimental values including a two state mixing (^{128}Xe*, see text), for the pure E(5) symmetry [64] (row denoted E(5)), for the O(5)-confined β-soft rotor model [65] with the structural parameter r_β=0.21 (row denoted O(5)-CBS), and for the IBM-1 fit (row denoted IBM-1).

	$R_{4/2}$	$R_{0_\tau^+/2}$	$R_{0_\xi^+/2}$	$\frac{B(E2;4_1^+\rightarrow 2_1^+)}{B(E2;2_1^+\rightarrow 0_1^+)}$	$\frac{B(E2;0_\tau^+\rightarrow 2_2^+)}{B(E2;2_1^+\rightarrow 0_1^+)}$	$\frac{B(E2;0_\xi^+\rightarrow 2_1^+)}{B(E2;2_1^+\rightarrow 0_1^+)}$	$\frac{B(E2;0_\xi^+\rightarrow 2_1^+)}{B(E2;0_\tau^+\rightarrow 2_2^+)}$
^{128}Xe	2.33	3.57	4.24	1.49(25)	1.24(26)	0.24(6)	0.19(6)
^{128}Xe*	2.33	3.76	4.05	1.49(25)	1.78(36)	0.33(7)	0.18(5)
E(5)	2.19	3.59	3.03	1.68	2.21	0.86	0.39
O(5)-CBS	2.32	3.88	4.27	1.57	2.00	0.52	0.26
IBM-1	2.37	2.85	4.54	1.43	1.45	0.40	0.27

In ^{128}Xe the situation is, however, more complicated, as will be clarified below, and the unambiguous assignment needs to be based on the knowledge of absolute $E2$ decay rates from our new data. The 0_2^+ state at 1582.9 keV is assigned to be the 0_τ^+ state. It decays strongly to the 2_2^+ state [$B(E2; 0_2^+ \rightarrow 2_2^+)$=52.8(76) W.u.]. This behavior confirms the three-phonon-like nature of the 0_2^+ state. Note that there is also a weak decay to the 2_1^+ state [$B(E2; 0_2^+ \rightarrow 2_1^+)$=3.69(58) W.u.]

that we discuss below. The decay pattern of the 0_3^+ state at 1877.3 keV does not reflect the behavior of the expected 0_ξ^+ state at first glance. The measured $B(E2;0_3^+ \rightarrow 2_1^+)$=10.4(23) W.u.=0.24(6)×$B(E2;2_1^+ \rightarrow 0_1^+)$ is about 2 times smaller than the $B(E2;0_3^+ \rightarrow 2_2^+)$=22.2(46) W.u.=0.52(13)×$B(E2;2_1^+ \rightarrow 0_1^+)$ and does not appear to be supressed at all. This fact is in conflict with the O(5) selection rules. It indicates breaking of O(5) symmetry in ^{128}Xe. Such symmetry breaking allows for the close-lying $0_\xi^+(\tau = 0)$ and $0_\tau^+(\tau = 3)$ configurations to mix with each other. Their mixing has been observed already in Ref. [65] and must be taken into account for a quantitative clarification of the situation in ^{128}Xe. The new data on absolute $B(E2)$ values enables us to do this in an unambiguous way. We consider the admixed wave functions of the 0_2^+ and 0_3^+ states

$$|0_2^+\rangle = \alpha_\tau|0_\tau^+\rangle + \alpha_\xi|0_\xi^+\rangle, \tag{7.6}$$

$$|0_3^+\rangle = -\alpha_\xi|0_\tau^+\rangle + \alpha_\tau|0_\xi^+\rangle. \tag{7.7}$$

The 0_τ^+ and 0_ξ^+ are orthogonal states and $\alpha_\tau^2 + \alpha_\xi^2 = 1$. Since $\langle 2_2^+|T(E2)|0_\xi^+\rangle = 0$ and $\langle 2_1^+|T(E2)|0_\tau^+\rangle = 0$ we obtain

$$B(E2;0_2^+ \rightarrow 2_1^+) = \alpha_\xi^2 B(E2;0_\xi^+ \rightarrow 2_1^+), \tag{7.8}$$

$$B(E2;0_3^+ \rightarrow 2_1^+) = \alpha_\tau^2 B(E2;0_\xi^+ \rightarrow 2_1^+), \tag{7.9}$$

$$B(E2;0_2^+ \rightarrow 2_2^+) = \alpha_\tau^2 B(E2;0_\tau^+ \rightarrow 2_2^+), \tag{7.10}$$

$$B(E2;0_3^+ \rightarrow 2_2^+) = \alpha_\xi^2 B(E2;0_\tau^+ \rightarrow 2_2^+). \tag{7.11}$$

The mixing parameters can independendly be determined from the appropriate ratios of experimental $B(E2)$ values. We obtain $\alpha_\xi^2/\alpha_\tau^2 = 0.35(10)$ from Eqs. (7.8,7.9) and $\alpha_\xi^2/\alpha_\tau^2 = 0.42(11)$ from Eqs. (7.10,7.11). The agreement of these values within uncertainties confirms the consistency of the two-state mixing scenario. We proceed in using the average value $\alpha_\xi^2/\alpha_\tau^2 = 0.39(7)$ which results in

$$\alpha_\tau^2 = 0.72(4) \quad \text{and} \quad \alpha_\xi^2 = 0.28(2)\ .$$

Using these values in Eqs. (7.8-7.11), our data from Table 7.6 yield the $E2$ transition rates $B(E2;0_\tau^+ \rightarrow 2_2^+) = 76(10)$ W.u. and $B(E2;0_\xi^+ \rightarrow 2_1^+) = 14(2)$ W.u. for the unperturbed configurations. From the mixing parameters and the energies of the perturbed levels, we have determined the unperturbed energies of the pure configurations which are $E(0_\tau^+) = 1666$ keV and $E(0_\xi^+) = 1795$ keV. The situation is illustrated in Fig. 7.15, in which the unperturbed levels 0_τ^+ and 0_ξ^+ are interacting through the interaction V.

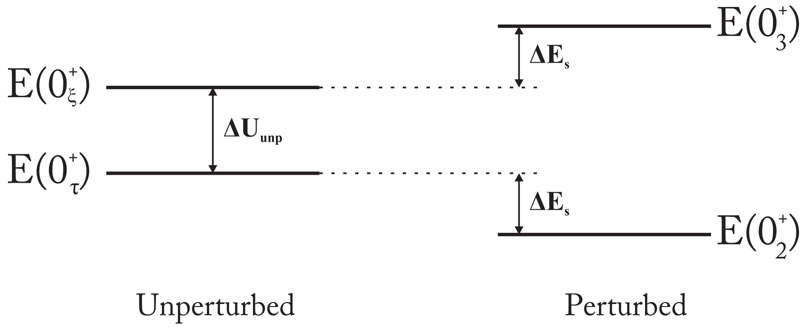

Figure 7.15: Two-state mixing between 0_τ^+ and 0_ξ^+ states separated by the energy ΔE_{unp}. The experimental states are the perturbed states (right), shifted by the energy ΔE_s.

The mixing matrix element $<0_\tau^+|\mathrm{V}|0_\xi^+>$ is simply denoted V. In the basis (0_τ^+;0_ξ^+), the Hamiltonian can be written as:

$$H = \begin{bmatrix} E(0_\tau^+) & V \\ V & E(0_\xi^+) \end{bmatrix}.$$

By diagonalyzing this 2 × 2 matrix in the (0_2^+;0_3^+) eigenvector basis, we obtain:

$$H = P \cdot D \cdot P^{-1} = P \cdot \begin{bmatrix} E(0_2^+) & 0 \\ 0 & E(0_3^+) \end{bmatrix} \cdot P^{-1},$$

where P is the transformation matrix from the basis (0^+_τ;0^+_ξ) into the basis (0^+_2;0^+_3), *i.e* the eigenvectors (0^+_2;0^+_3) expressed in the basis (0^+_τ;0^+_ξ) (7.6, 7.7).

$$P = \begin{bmatrix} \alpha_\tau & -\alpha_\xi \\ \alpha_\xi & \alpha_\tau \end{bmatrix}.$$

Since P is orthogonal:

$$P^{-1} = \begin{bmatrix} \alpha_\tau & \alpha_\xi \\ -\alpha_\xi & \alpha_\tau \end{bmatrix}.$$

Finally:

$$H = \begin{bmatrix} E(0^+_\tau) & V \\ V & E(0^+_\xi) \end{bmatrix} = \begin{bmatrix} \alpha^2_\tau E(0^+_2) + \alpha^2_\xi E(0^+_3) & \alpha_\tau \alpha_\xi [E(0^+_2) - E(0^+_3)] \\ \alpha_\tau \alpha_\xi [E(0^+_2) - E(0^+_3)] & \alpha^2_\xi E(0^+_2) + \alpha^2_\tau E(0^+_3) \end{bmatrix} = \begin{bmatrix} 1666 & 132 \\ 132 & 1795 \end{bmatrix}$$

We denote this unperturbed situation as ^{128}Xe* (Fig. 7.16). We stress that the 0^+_ξ configuration lies above the three-phonon one 0^+_τ configuration. This ordering is in qualitative contrast to the prediction made by the E(5) model [64].

As previously inferred from the $R_{4/2}$ ratio, ^{128}Xe lies in the E(5)-O(6) region, well described by the O(5)-CBS model. Therefore, we compare the unperturbed experimental situation (^{128}Xe*) to the prediction of the O(5)-CBS rotor model. The model's sole parameter r_β has been fixed before [65] to reproduce the experimental $R_{4/2}$ ratio of ^{128}Xe. The agreement between ^{128}Xe* and the model predictions on the energies and $E2$ transition rates is satisfactory as shown in Fig. 7.16. This includes the crucial ordering of the excited 0^+_τ and 0^+_ξ configurations.

Our data and our analysis have emphasized the significance of the ordering of the excited 0^+_τ and 0^+_ξ configurations for assigning the structure of a nucleus near the E(5) critical point. Therefore, it is interesting to examine the behavior of the observable $\Delta_{0^+} = [E(0^+_\xi) - E(0^+_\tau)]/E(2^+_1)$. It takes the values -1 (harmonic vibrator), -0.56 (E(5)), 0 at the crossing point of the $0^+_{\tau,\xi}$ configurations and becomes positive towards the O(6) limit. Along the chain of Xe isotopes we consider the experimental energies of the first and the second excited 0^+ states with dominant 0^+_τ or 0^+_ξ assignment. The assignments of their dominant character have been done for ^{124}Xe ([102, 89]), ^{126}Xe ([108]), ^{128}Xe ([65] and this work), ^{130}Xe ([65]) already in the literature. These data are plotted in Fig. 7.17. The $R_{4/2}$ ratios shown on top decrease monotonically as a function of neutron number from 2.48 for ^{124}Xe to 2.04 for ^{134}Xe. The value of 2.20 expected for E(5) is crossed between ^{130}Xe and ^{132}Xe. The 0^+ configurations cross between ^{128}Xe and ^{130}Xe (middle Fig. 7.17). The Δ_{0^+} value for ^{128}Xe is positive. This rules out ^{128}Xe as a candidate for a realization of E(5) symmetry. We observe, however, that $\Delta_{0^+} = -0.42$ for ^{130}Xe making that nucleus a promising candidate for a close match of E(5) predictions.

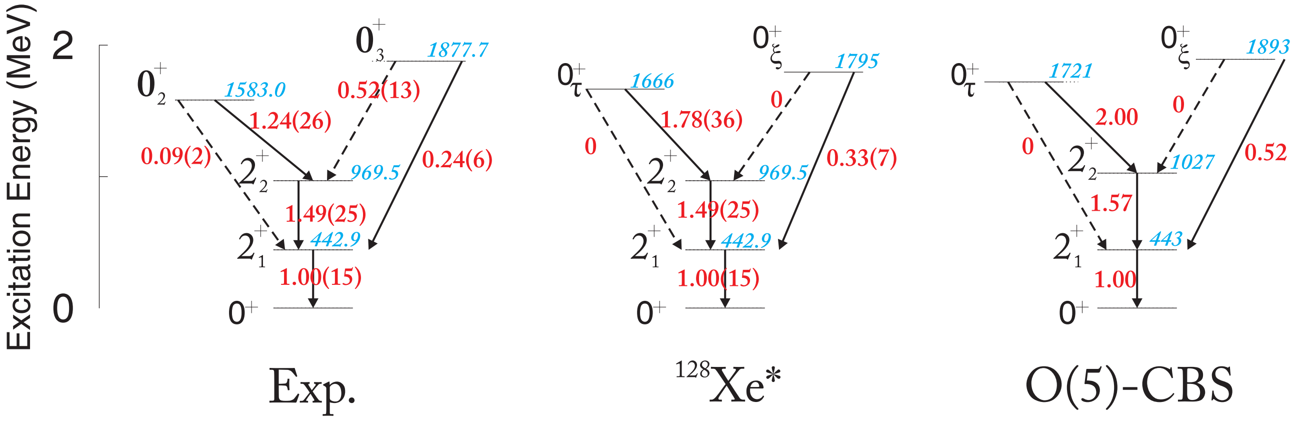

Figure 7.16: Energy level scheme and $B(E2)$ transition strengths from 0^+_2 and 0^+_3 states of ^{128}Xe (left), for the experimental unperturbed O(5)-symmetric states 0^+_τ and 0^+_ξ (^{128}Xe*, middle, see text) and for the O(5)-CBS model (right) from Ref. [65].

In summary 19 absolute $E2$ transitions strengths have been measured including the hitherto unknown $B(E2)$ values from the 0^+_2 and 0^+_3 states. This enabled us to unambiguously identify the main components of the 0^+_τ and 0^+_ξ configurations. The ordering of these 0^+ configurations in ^{128}Xe is opposite to the prediction based on E(5) symmetry. Therefore we conclude that ^{128}Xe is not a close realization of E(5) symmetry, leaving ^{130}Xe as the most likely candidate amongst the xenon isotopes. Our analysis highlights the importance of the relative energies of the first *two* excited 0^+ states and their $E2$ decay rates as a robust test of E(5) symmetry. Similar tests on ^{130}Xe and ^{134}Ba would conclusively demonstrate how well E(5) is realized in these "best cases".

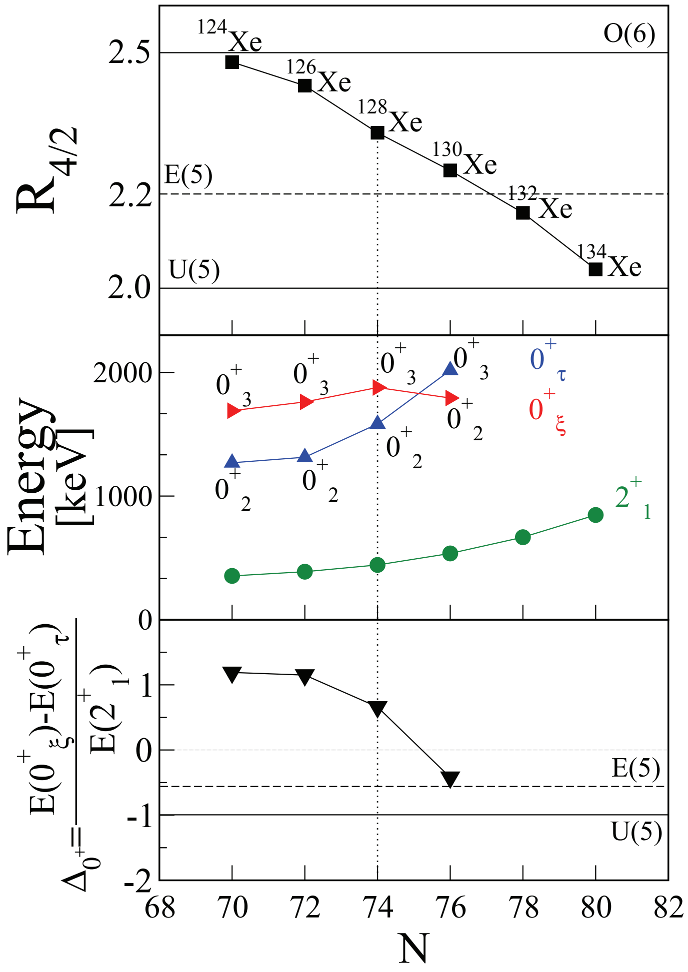

Figure 7.17: Evolution of $R_{4/2}$=E(4^+_1)/E(2^+_1) (top), energies of 0^+_τ, 0^+_ξ, and 2^+_1 states (middle), and $\Delta_{0^+} = \frac{E(0^+_\xi)-E(0^+_\tau)}{E(2^+_1)}$ (bottom) along the stable Xe chain from ^{124}Xe to ^{134}Xe.

Details about the experiment can be found in section 6.1. Doppler correction (recoiling velocity β=6.4(2)%, β=6.3(2)% for ^{130,132}Xe respectively) and time random background subtraction have been applied and the resulting singles spectra are displayed in Fig. 7.18. Unfortunately the ^{132}Xe-ion beam was slightly contaminated with ^{37}Cl impurity due to the close A/q ratio of both species in the 25$^+$ (Xe), 7$^+$ (Cl) charge states. Therefore, the γ-ray spectra contain lines (labeled with $*$ in Fig.7.18) related to reaction products, *e.g* ^{37}Cl(^{12}C,np)^{46}Ti of these beam impurities. The intensities of the Xe lines interfering with these background lines were deduced through their previously known branching ratios. The total number of events was 9.2×10^8 for a running time of $\sim$ 24 h for ^{130}Xe and 4.7×10^8 total events were recorded in $\sim$ 13 h for ^{132}Xe. Approximately 8.4×10^6 and 6.2×10^6 events of γ-ray fold higher than 1 were collected and sorted into $\gamma\gamma$-coincidence matrices for ^{130}Xe and ^{132}Xe, respectively. All γ-transitions observed have been placed in the level scheme of ^{130}Xe and ^{132}Xe. They are plotted in Fig. 7.19 and Fig. 7.20, respectively. All γ-transitions observed with their corresponding intensities were already reported in Refs. [136, 137, 105]. They are summarized in Tables 7.9 and 7.10. Population yields of each state have been deduced from γ-singles and $\gamma\gamma$-coincidence data. The contributions from the electron conversion decays to the populations of the states was small in comparison to the systematic errors (< 1.5%, [131]) and have been neglected. The contributions of known transitions that we were not able to observe (*e.g.* due to too small energy or contaminations), have been determined from previously published branching ratios from Ref. [136, 137]. The observed relative yields measure the Coulomb Excitation (CE) cross sections relative to the 2^+_1 state. The multiple code CLX, based on the Winther-De Boer theory [77] has been used to determine the set of matrix elements for reproducing the observed relative cross sections. The previously known $B(E2; 2^+_1 \rightarrow 0^+_1)$ value from Ref. [94] sets the absolute scale. The signs of the matrix elements have been chosen as the corresponding one proposed by the IBM-1 calculation of ^{128}Xe and are also given in Tables 7.9 and 7.10. A tentative of IBM-1 fit has been made for ^{130}Xe using the Hamiltonian of Eq. 7.2 as done in [102]. The energy level spectrum, especially the spacing in the ground state band, could not be well reproduced. Therefore we decided to adopt only the signs proposed by the IBM-1 calculation of ^{128}Xe for ^{130,132}Xe to assure the quantum mechanically coherence between the realtive phases of the states. For more details concerning the CLX analysis (energy loss, constraints, quadrupole moments, relative phases), see section 6.2.5. Our analysis resulted in 14 absolute $B(E2)$ values in ^{130}Xe and 6 absolute $B(E2)$ values in ^{132}Xe. The derived lifetimes (τ) are also listed in Tables 7.9 and 7.10.

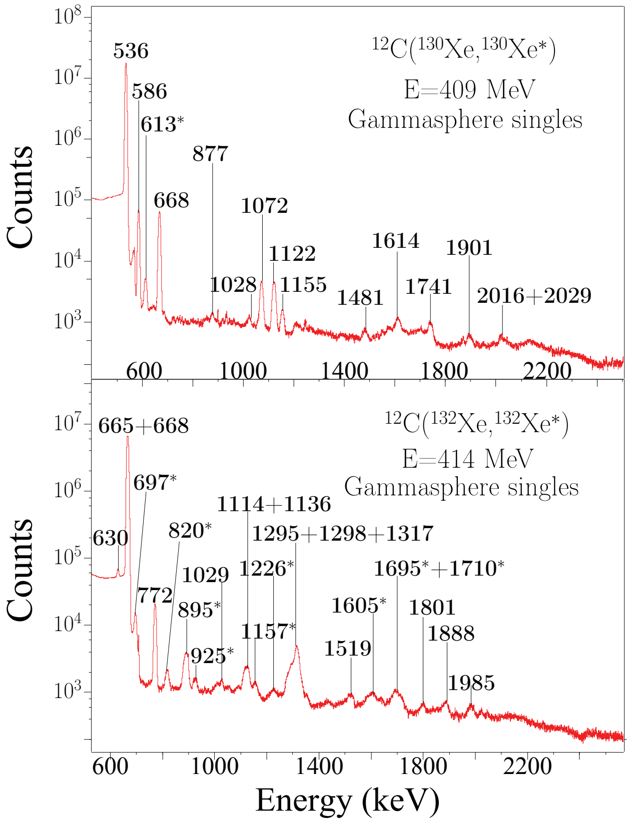

Figure 7.18: Background-subtracted and Doppler-corrected singles γ-ray spectra for the sum over all Ge detectors in Gammasphere for ^{130}Xe (up) and ^{130}Xe (bottom). The asterisks show peaks coming from impurities of the beam.

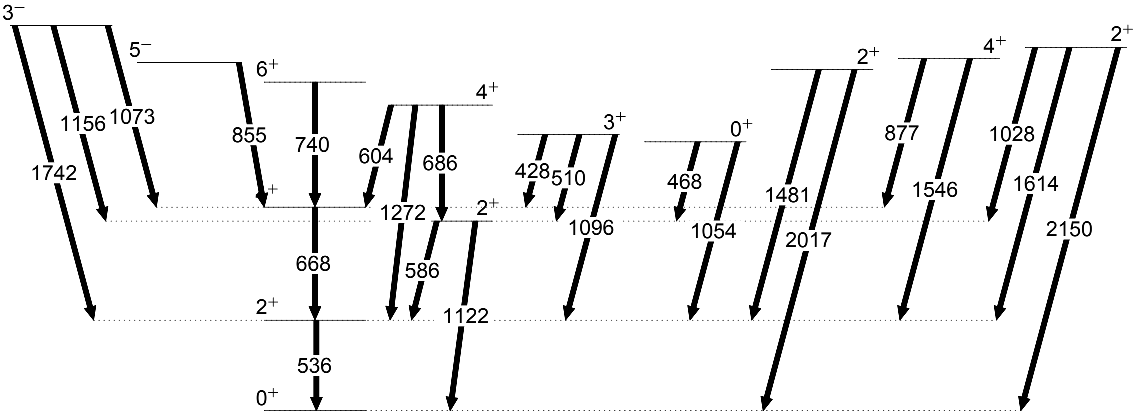

Figure 7.19: Part of the low-spin level scheme of ^{130}Xe showing all levels for which we observed γ-ray transitions in the ^{12}C(^{130}Xe,^{130}Xe*) projectile Coulomb excitation reaction.

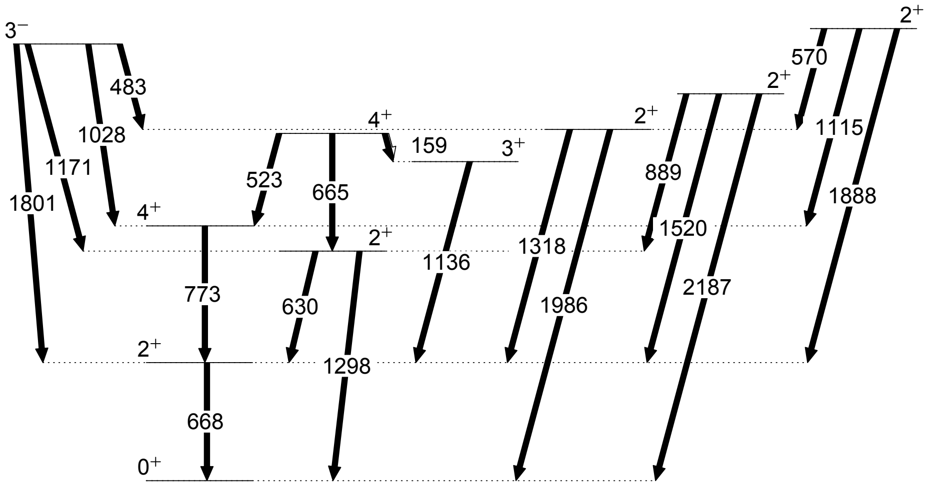

Figure 7.20: Part of the low-spin level scheme of ^{132}Xe showing all levels for which we observed γ-ray transitions in the ^{12}C(^{132}Xe,^{132}Xe*) projectile Coulomb excitation reaction.

^{130}Xe:

- **2_1^+ state at 536.1 keV**
  The spectrum of Fig. 7.18 (left) is dominated by the 536-keV line from the 2_1^+ state to the ground state with about 4.1×10^8 counts. The corresponding angular distribution with its respective coefficients $a_2 = A_2/A_0$ and $a_4 = A_4/A_0$ is given in Fig. 6.12.

- **2_2^+ state at 1122.1 keV**
  The angular distributions coming from this state with their respective coefficients $a_2 = A_2/A_0$ and $a_4 = A_4/A_0$ are given in Fig. 6.12. A value of $\delta = -0.30(5)$ has been deduced. This value is in contradiction with the previously known $\delta = +3.75(12)$ value from Ref. [136]. Due to possible contaminations in our spectrum or due to some deorientation effects, we adopted the $\delta = +3.75(12)$ value from Ref. [136] for the CLX calculations.

- **4_1^+ state at 1204.6 keV**
  The unobserved $4_1^+ \rightarrow 2_2^+$ transistion at 82.5 keV does not play a significant role for the population of the 4_1^+ state at 1204.6 keV. Similarly to the 4_1^+ state in ^{126}Xe, the CLX calculations have been done assuming no $E4$

transition from the ground state to the 4_1^+ state (see section 7.2).

- **State at 1590.4 keV**
  The spin and parity of this state are unknown. We observed only the 469-keV line to the 2_2^+ state in coincidence with the 586 keV gate. We derived the intensity of the 1053.6-keV line to the 2_1^+ state from the known branching of Ref. [136]. These two transitions have already been observed in Ref. [141]. No transition from this level to the ground state was observed and since there are 2^+ and 4^+ level candidates for the two-phonon triplet it may be that the 1590.6 keV level is 0^+.

- **2_3^+ state at 2017.1 keV**
  The state at 2017 keV is reported in Ref. [136] as a 0^+ state. This assignment has been done by Hopke *et al.* Ref. [138] where they observed the transitions to 2_1^+ (1481 keV) and to 2_2^+ (894 keV) states with a branching ratio of $I_{1481}/I_{894} = 0.06(1)$. We have observed the 2017 keV γ-transition to the ground state which rules out a 0^+ assignment. In Ref. [139], the observed branching ratio $[I_{1481}/I_{894} = 3.8(11)]$ which diverges strongly from the one measured in [138] lead them to suggest that the 1481-keV line in their data was a doublet. They also proposed spin 0,1, or 2 for the state at 2017 keV. In our experiment this state has been populated via Coulomb excitation. Consequently, it is more probable to populate it through a one step $E2$ excitation rather than $E1$ or multistep excitations. We stress that we do not observe the strong 894 keV transition known [138] to stem from the 2017-keV 0^+ state while the 1481-keV line is well visible in our data (see Fig. 7.18). Thus, we adopt here the existence of two degenerate states at 2017 keV with $J^\pi = 0^+$ and $J^\pi = 2^+$.

- **2_4^+ state at 2150.2 keV**
  This state is considered as the main fragment of the MSS since $B(M1; 2_4^+ \to 2_1^+) = 0.15(4)\ \mu_N^2$. The decay to the ground state has a strength of $B(E2; 2^+ \to 0_1^+) = 0.25(7)$ W.u. as might be expected for a fragment of the $2_{1,\mathrm{ms}}^+$ state.

<u>^{132}Xe:</u>

- **2_1^+ state at 667.7 keV**
  The spectrum of Fig. 7.18 (right) is dominated by the 536-keV line from the 2_1^+ state to the ground state with about 4.1×10^8 counts. The corresponding angular distribution with its respective coefficients $a_2 = A_2/A_0$ and $a_4 = A_4/A_0$ is given in Fig. 6.13.

- **2_2^+ state at 1297.9 keV**
  The 1297.9-keV transition to the ground state was mixed with the $4_2^+ \to 2_1^+$ transition ($E_\gamma = 1295.1$ keV) and with the strong decay from the 2_3^+ state at 1985.6 keV to the 2_1^+ state ($E_\gamma = 1317.1$ keV). This triplet line can be seen in the right panel of Fig. 7.18. The individual intensities of the 1297.9-keV and 1295.1-keV lines have been derived from the known branching ratios from Ref. [137]. The intensity of the 1317.9-keV line has been measured through a coincidence gate with the 536-keV line.

- **4_1^+ state at 1440.3 keV**
  The unobserved $4_1^+ \to 2_2^+$ transistion at 142.4 keV does not play a significant role for the population of the 4_1^+ state at 1440.3 keV. Another issue with the population of the 4_1^+ is the contribution of the one-step $E4$ COULEX. Similarly to the 4_1^+ state in ^{126}Xe, the CLX calculations have been done assuming no $E4$ transition from the ground state to the 4_1^+ state (see section 7.2).

- **3_1^+ state at 1803.7 keV**
  Eventhough the intensities of all γ-ray transitions from this state have been measured, no $B(E2)$ could have been calculated. This is because the population yields of the 3_1^+ state was not known. Indeed we were not able to quantify the strong feeding from the 4_2^+ state at 1963 keV through the 159-keV line.

- **4_2^+ state at 1963.0 keV**
  As already mentioned the intensity of the $4_2^+ \to 3_1^+$ γ-ray line at 159 keV could not have been measured for two reasons. First because the relative efficiency at this energy is not well known (see Fig. 6.5) and then because the region 0-500 keV is dominated by the strong background Compton scattering. Moreover the usually strong decay $4_2^+ \to 2_2^+$ within the β-band, here at 665.1 keV was a doublet with the strong $2_1^+ \to 0_1^+$ transition (667.7 keV). The branching ratio is also unknown and it was therefore impossible to measure or derive the individual intensity of the 665.1-keV line. This did not enable us to establish the population yields

of the 4_2^+ state at 1963.0 keV. Thus no $B(E2)$ transition strengths have been measured.

- **2_3^+ state at 1985.6 keV**
  This 2^+ state is the main fragment of the MSS since $B(M1; 2_3^+ \rightarrow 2_1^+) = 0.22(6)\ \mu_N^2$. The decay to the ground state has a strength of $B(E2; 2^+ \rightarrow 0_1^+) = 0.67(18)$ W.u. as might be expected for the $2_{1,\mathrm{ms}}^+$ state.

- **2_4^+ state at 2187.4 keV**
  In contrast to the 2_3^+ state, the mixing ratio δ for the mixed $E2, M1$ transition to the 2_1^+ state is unknown. Therefore we could only deduce an upper value for the pure magnetic transition strength [$B(M1; 2_4^+ \rightarrow 2_1^+) \leq 0.020(6)\ \mu_N^2$]. This upper value is about one order of magnitude smaller than the $B(M1; 2_3^+ \rightarrow 2_1^+)$ which leaves the 2_3^+ state at 1985.6 keV as the main fragment of the MSS.

- **2_5^+ state at 2555.6 keV**
  The spin of this state is not well known: $J = 2^+$ or $J = 3$. The $B(E2)$ values were not measured because the branching ratio to the ground state is unknown.

We note that our results are in very good agreement with the previously known $B(E3)_\uparrow$ values [105] (Tables 7.9 and 7.10) and $B(M1)$ values [42, 141] (Table 7.11).

Collective excitations are an important and ubiquitous excitation mode found in many nuclei. It is known that evolution of collectivity across the nuclear chart is governed by the proton-neutron interaction in the valence shell, see e.g Ref. [1]. It is, therefore, important to find and study such nuclear states that are particularly sensitive to the proton-neutron interaction in the valence shell. A special class of collective states is represented by the so-called mixed symmetry states (MSSs). The 1^+ MSSs have been discovered by Richter *et al.* [133] in well-deformed nuclei where the phenomenon is known as the "scissors mode". Its existence was predicted in the framework of the geometrical Two Rotor Model [134]. In the framework of the Interacting Boson Model-2 (IBM-2), MSSs are defined in terms of the F-spin quantum number [29, 38] with $F = F_{max} - 1$. In vibrational nuclei, all hitherto discovered MSS have been reviewed in [9]. It has been shown that the lowest lying MSS is the one quadrupole phonon MSS labeled as $2_{1,\mathrm{ms}}^+$ and characterized by a weakly-collective $E2$ transition probability to the ground state and a large $M1$ transition to the 2_1^+ state [38]. The three dynamical symmetries of the IBM [15, 29], U(5) for vibrating nuclei [13], SU(3) for axially deformed nuclei [53] and O(6) for γ-softness or γ-instability [15] provide structural benchmarks for the description of nuclear quadrupole collectivity. The properties of MSSs are analytically known at all these symmetries, but their evolution from one symmetry to another is still unknown. The low-lying collective quadrupole states of the Xe-Ba-Ce mass region have been numerically investigated by Puddu *et al.* [20] within the IBM-2. It turned out that the even $_{54}$Xe isotopes exhibit a structural change from a U(5)-like behavior towards O(6)-like pattern as the number of neutron hole pairs increases from the closed shell $N = 82$. This was later supported by Casten and von Brentano [21] who presented evidence for an extensive region of nuclei near $A = 130$ including $^{124-132}$Xe resembling a situation close to the O(6) symmetry. In this way, stable Xe isotopes offer a possibility to study the evolution of the MSS on the transitional path from a vibrational structure towards an O(6)-like behavior. In this work, we report the identification of the $2_{1,\mathrm{ms}}^+$ states in ^{130}Xe and ^{132}Xe by measuring absolute $M1$ transition strengths using Coulomb excitation. The $2_{1,\mathrm{ms}}^+$ states is already known in ^{134}Xe [90]. By combining the results of the present work with the results from [90], it is possible for the first time to follow the evolution of the $2_{1,\mathrm{ms}}^+$ state along the U(5) to O(6)-like transitional region through an isotopic chain, namely $^{124-134}$Xe. It is the purpose of this section to show how the $2_{1,\mathrm{ms}}^+$ state and hence the fundamental collective isovector excitation in the valence shell of $_{54}$Xe evolves in going from a vibrator-like structure ($N \sim 80$) to a more deformed, γ-soft-like structure ($N \sim 70$).

In both isotopes, ^{130,132}Xe, we identify a single 2^+ state that entirely dominates the $2_i^+ \rightarrow 2_1^+$ $M1$ strength distribution up to our sensitivity limit at about 2.2 MeV. These states are the 2_4^+ state of ^{130}Xe at 2150 keV [$B(M1; 2_{1,\mathrm{ms}}^+ \rightarrow 2_1^+) = 0.15(4)\ \mu_N^2$] and the 2_3^+ level of ^{132}Xe at 1985 keV [$B(M1; 2_{1,\mathrm{ms}}^+ \rightarrow 2_1^+) = 0.22(6)\ \mu_N^2$]. Other $B(M1; 2_{1,\mathrm{ms}}^+ \rightarrow 2_1^+)$ values are negligible in comparison. We, therefore, assign predominant mixed-symmetry character to them. The MSSs of ^{130,132}Xe combined with the results for ^{134}Xe [90] reveal first information on the evolution of the fundamental isovector valence-shell excitation along the Xe isotopic chain, as shown in Fig. 7.21 and Table 7.11.

Also in ^{128,134}Xe the detected $B(M1; 2_{1,\mathrm{ms}}^+ \rightarrow 2_1^+)$ strength is concentrated in a single state as well. Note that no MSSs have been observed in ^{124}Xe and ^{126}Xe below about 2.2 MeV. Fig. 7.21 indicates that the detected $2_{1,\mathrm{ms}}^+ \rightarrow 2_1^+$ $M1$ strength

Table 7.9: Measured properties of the levels and γ-ray transitions in ^{130}Xe.

E_{level} (keV)	J^{π}	E_{γ} (keV)	I_{γ}	J^{π}_{final}	δ^{a}	σ	$B(E2)^{b}$ (W.u.)	τ (ps)
536.1	2^+_1	536	10^6	0^+_1		+	$33.2(26)^{c}$	$14.2(11)^{c}$
1122.1	2^+_2	586.0	3973(28)	2^+_1	+3.75(12)	-	44.3(81)	5.5(1)
		1122.1	681(6)	0^+_1		+	0.28(5)	
1204.6	4^+_1	82.5^{d}		2^+_2		-		3.4(3)
		668.5	4835(34)	2^+_1		+	46.4(46)	
1590.4	0^{+e}	469.2^{f}	18.6(24)	2^+_2		-	256(118)	2.0(5)
		1053.6^{g}	15(15)	2^+_1		+	3.6(38)	
1632.6	3^+_1	427.9^{g}	1.04(23)	4^+_1		-	$\leq 53(21)^{h}$	2.0(8)
		510.5^{f}	10.6(20)	2^+_2		+	$\leq 226(40)^{h}$	
		1096.5^{g}	6.9(14)	2^+_1	$+1.3^{+3.8}_{-0.8}$	-	1.2(26)	
1808.2	4^+_2	603.5^{f}	18.8(16)	4^+_1		+	$\leq 25.6(45)^{h}$	2.6(3)
		686.1^{f}	23.8(19)	2^+_2		-	23.2(44)	
		1272.1^{f}	20.1(25)	2^+_1		-	0.74(14)	
1944.1	6^+_1	739.5^{f}	16.4(18)	4^+_1		+	69(9)	1.7(2)
2017.1	2^{+i}_3	1481.8	70.6(33)	2^+_1		-	$\leq 0.86(21)^{h}$	≤2.1(4)
							$B(M1) \leq 0.005(2)\ \mu_N^2$	
		2017.1	42.1(21)	0^+_1		-	0.11(2)	
2059.6	$5^{(-)}$	855.0^{f}	17.9(20)	4^+_1				
2081.9	4^+_3	877.3	46.6(10)	4^+_1		-	$\leq 247(43)^{h}$	0.14(2)
		1545.8^{g}	5.6(10)	2^+_1		+	1.74(43)	
2150.2	2^+_4	1028.1^{f}	14.1(24)	2^+_2	$+0.18(35)^{j}$	+	0.55(16)	0.08(2)
							$B(M1)=0.05(2)\ \mu_N^2$	
		1614.1	154(5)	2^+_1	$-0.08(14)^{j}$	-	0.13(47)	
							$B(M1)=0.15(4)\ \mu_N^2$	
		2150.1^{g}	7.2(5)	0^+_1		-	0.24(7)	
2278	3^-_1	1072	461(20)	4^+_1				
		1155	130(7)	2^+_2				
		1741	124(5)	2^+_1				
						+	$B(E3)=0.023(9)^{k}$	
2437		1901^{f}	64.7(33)	2^+_1				
2565		2029^{f}	54.6(33)	2^+_1				

---

[a] Mixing ratios are taken from Ref. [136].

[b] $B(E2)$ values are given in W.u. (1 W.u.$(E2) = 0.003912\ e^2b^2$) and the $B(M1)$ values are given in μ_N^2.

[c] From Ref. [94].

[d] This transition is not observed. Contrary to the situation in Ref. [89], this transition is not relevant for the population of the 4^+_1 state.

[e] Spin and parity of this state are unknown. It was supposed to be a 0^+ state. For more details, see text.

[f] These transitions were detectable for us only in coincidence spectra.

[g] These transitions are not observed by us but are included in the calculations for the Coulomb cross-sections. Their intensities are deduced from the previously known branching ratios from Ref. [136].

[h] Upper value for the $B(E2)$ since the multipole mixing ratio δ was unknown, quoted value obtained by assuming a pure $E2$ transition.

[i] This state has been supposed to be a 2^+ state. For more details, see text.

[j] From Ref. [140].

[k] $B(E3)\uparrow$ value given in e^2b^3. In Ref. [105], a $B(E3)\uparrow = 0.033(9)\ e^2b^3$ value is reported.

Table 7.10: Measured properties of the levels and γ-ray transitions in ^{132}Xe.

E_{level} (keV)	J^{π}	E_{γ} (keV)	I_{γ}	J^{π}_{final}	δ^{a}	σ	$B(E2)^{b}$ (W.u.)	τ (ps)	$\tau^{a}_{Lit.}$ (ps)
667.7	2^+_1	667.7	10^6	0^+_1		+	$23.1(15)^{c}$	$6.68(44)^{c}$	6.68(44)
1297.9	2^+_2	630.2	2026(19)	2^+_1	+4.07(16)	-	26.8(42)	6.78(88)	4.4(4)
		1297.9^{d}	136(12)	0^+_1		+	0.051(7)		
1440.3	4^+_1	142.4^{e}		2^+_2		-		2.53(34)	2.6(2)
		772.6	3427(26)	2^+_1		+	29.5(45)		
1803.7	3^+_1	363.3^{f}	10.6(40)	4^+_1	1.10(20)	-			
		505.8^{f}	114(42)	2^+_2	7.5(6)	+			
		1136.0^{i}	72(26)	2^+_1	+0.34(2)	-	^{g}		
1963.0	4^+_2	159.3^{h}		3^+_1		+			
		522.6^{i}	115(15)	4^+_1	-0.09(1)	-			
		665.1^{j}		2^+_2		-			
		1295.1^{d}	13.5(19)	2^+_1		-			
1985.6	2^+_3	1317.9	1695(31)	2^+_1	-0.16(5)	-	1.14(73)	0.10(2)	
							$B(M1) = 0.22(6)\ \mu_N^2$		
		1985.6	192(5)	0^+_1		-	0.67(18)		
2187.4	2^+_4	889.6^{d}	81(23)	2^+_2		+	$\leq 32(13)^{k}$	0.26(14)	
		889.6		2^+_2			$B(M1) \leq 0.07(3)\ \mu_N^2$		
		1519.6	132(7)	2^+_1		-	$\leq 3.1(9)^{k}$		
		1519.6		2^+_1			$B(M1) \leq 0.020(6)\ \mu_N^2$		
		2187.5^{f}	45(12)	0^+_1		-	0.20(3)		
2468.8	3^-_1	483.0^{f}	142(8)	2^+_3					
		1028.8	104(3)	4^+_1	-0.071(11)				
		1171.2^{f}	56(4)	2^+_2					
		1801.1	109(4)	2^+_1					
						+	$B(E3)=0.022(7)^{l}$		
2555.6	2^{+m}_5	570.1	119(17)	2^+_3	$+0.7^{4}_{3}$	+			
		1114.5^{d}	95(16)	4^+_1		+			
		1887.6	151(10)	2^+_1		+			

---

[a] Taken from Ref. [137].

[b] $B(E2)$ values are given in W.u. (1 W.u.$(E2)=0.003992\ e^2b^2$), and the $B(M1)$ values are given in μ_N^2.

[c] From Ref. [94].

[d] These transitions are doublets, the respective individual intensities have been separated through the known branching ratios from Ref. [137].

[e] This transition is not observed. Contrary to the situation in Ref. [89], this transition is not relevant for the population of the 4^+_1 state.

[f] These transitions are not observed by us but are included in the calculations for the Coulomb cross-sections. Their intensities are deduced from the previously known branching ratios from Ref. [137].

[g] The population of the 3^+_1 state is unknown since we could not quantify the feeding from the 4^+_2 state through the 159-keV line.

[h] This transition is seen but its intensity could not have been measured.

[i] These transitions were detectable for us only in coincidence spectra.

[j] This transition is a doublet with the $2^+_1 \rightarrow 0^+_1$ transition. Since its branching ratio is unknown, it was not possible to establish the yield of the 4^+_2 state.

[k] Upper value for the $B(E2)$ since the multipole mixing ratio δ was unknown, quoted value obtained by assuming a pure $E2$ transition.

[l] $B(E3)\uparrow$ value given in e^2b^3. In Ref. [105], a $B(E3)\uparrow = 0.016(6)\ e^2b^3$ value is reported.

[m] The spin of this state is not well known: $J = 2^+$ or 3. The $B(E2)$ values were not measured because the branching ratio to the ground state transition is unknown.

Table 7.11: Absolute strengths $B(M1;2^+_{1,\mathrm{ms}} \rightarrow 2^+_1)$ of the MSS found in the even-even Xe isotopes.

Isotope	N_ν	MSS	Energy [keV]	$B(M1;2^+_{i,\mathrm{ms}} \rightarrow 2^+_1)$ μ_N^2	Literature μ_N^2	Ref.
^{124}Xe	6			no MSS below 2.3 MeV		
^{126}Xe	5			no MSS below 2.1 MeV		
^{128}Xe	4	2^+_4	2127	0.04(1)	0.07(2)	[42]
^{130}Xe	3	2^+_4	2150	0.15(4)		
^{132}Xe	2	2^+_3	1986	0.22(6)	0.29[a]	[141]
^{134}Xe	1	2^+_3	1947	0.30(2)		[90]

---

[a] no uncertainty is given in [141].

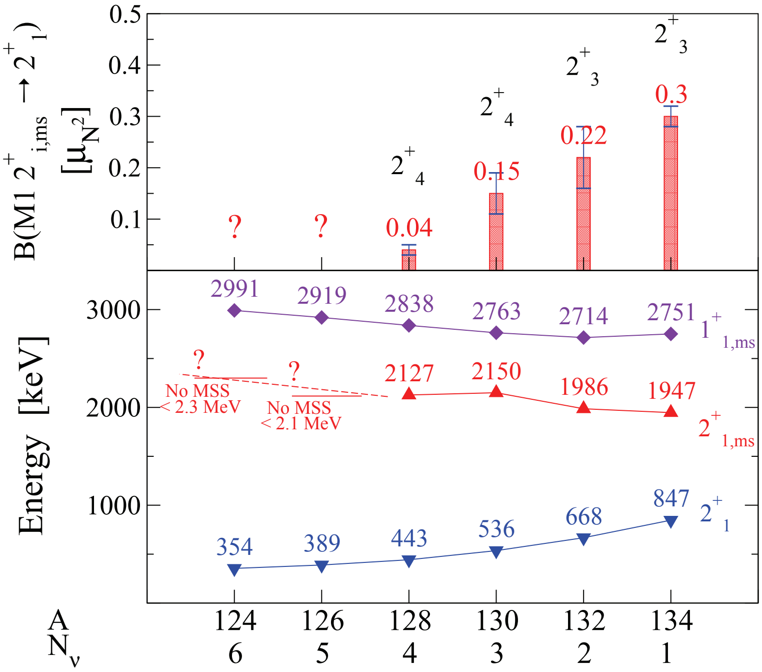

Figure 7.21: The evolution of the $B(M1;2^+_{1,\mathrm{ms}} \rightarrow 2^+_1)$ strength in μ_N^2 is presented at the top for the six even-even stable Xe isotopes. At the bottom are plotted the corresponding energy of the first one-quadrupole phonon $2^+_{1,\mathrm{ms}}$ state as well as the evolution of the excitation energy of the two quadrupole phonon $1^+_{1,ms}$ state investigated by H. von Garrel *et al.* [142].

decreases as the number of valence neutron pairs (N_ν) increases; *i.e*, with increasing collectivity. Simultaneously, the excitation energy of the state to which we have assigned the dominant mixed-symmetry character increases with increasing collectivity (N_ν). The same effect was observed for the two quadrupole phonon $1^+_{1,\mathrm{ms}}$ state [142]. The separation energy between the $2^+_{1,\mathrm{ms}}$ and the 2^+_1 states becomes larger as a function of $N_\pi N_\nu$ where N_π is the number of valence proton pairs.

At this point, the following issue arises: Does the fundamental isovector quadrupole collective mode ($2^+_{1,\mathrm{ms}}$) fragment along the path from vibrational nuclei towards γ-unstable rotors in such a way that associated strength gradually escapes detection or does it slowly dissolve and finally completely disappear in ^{124,126}Xe? Both hypotheses could explain the observed experimental behavior. In the first case, it is possible we only observe the lowest fragment of the MSS, which does not necessarily carry the largest part of the total $M1$ strength, because the experimental technique we used was limited to a certain excitation energy. In the second case, the states with mixed-symmetry character at the U(5) limit gradually lose their isovector character toward mid-shell and the $M1$ strength finally disappears. This scenario would require an yet as unknown mechanism. The former case can be discussed in the framework of a simple two-state mixing model.

According to the two-state mixing scheme outlined in Refs. [143, 90], the observed 2^+_1 and $2^+_{1,\mathrm{ms}}$ states arise through the mixing of the unperturbed proton and neutron 2^+ configurations (their energies are labeled here as ϵ_π and ϵ_ν,

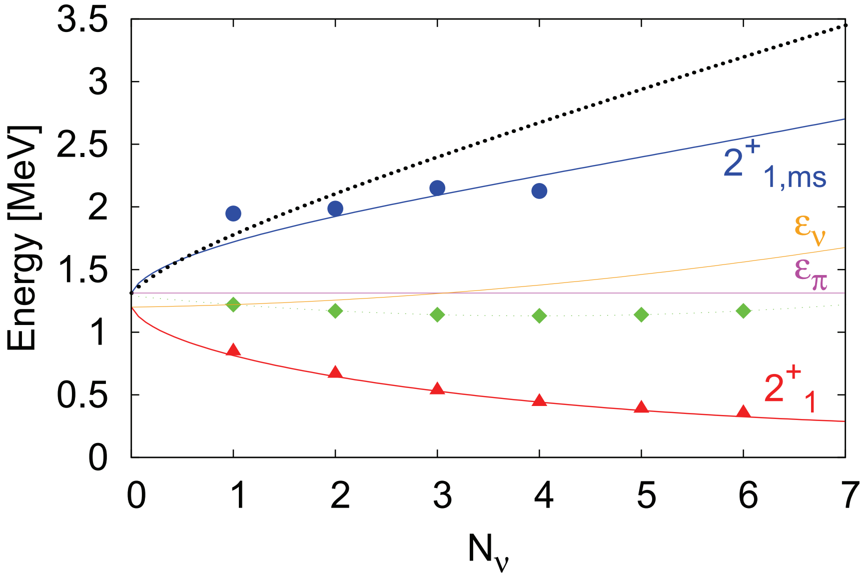

Figure 7.22: Fit of the experimental energies of the $2^+_{1,\mathrm{ms}}$ states (solid blue curve) and 2^+_1 states (solid red curve) in the $_{54}$Xe isotopes. The lines labeled ϵ_π and ϵ_ν represent the unperturbed energy of the proton and neutron state, respectively. The energies of the 2^+_1 states in the corresponding $Z = 50$ Sn isotopes are given as green diamonds. The black dashed line corresponds to the fit of the $2^+_{1,\mathrm{ms}}$ using the parameters (β=0.35(1) MeV, b=0.23(4) MeV) calculated via a two-state mixing in the $N = 80$ isotones (Ref. [90]).

respectively) in which the proton-neutron coupling matrix element increases as a function of the product $N_\pi N_\nu$. This mixing interaction originates from the proton-neutron quadrupole interaction and was parametrized [143] as $V_{\pi\nu}(N_\pi, N_\nu) = \beta\sqrt{N_\pi N_\nu}$ ($N_\pi = 2$ in our case). For studying the two-state model over the Xe isotopic chain, the energies of the elementary proton (ϵ_π) and neutron (ϵ_ν) quadrupole excitations need to be known over this sequence of nuclei. The unperturbed proton energy ϵ_π for the Xe isotopic chain has been chosen as the energy of the 2^+_1 state of the $N = 82$ semi-magic nucleus ^{136}Xe, *i.e* $\epsilon_\pi = E_{2^+_1}(^{136}\mathrm{Xe})$=1313 keV. On the other hand, we have to take into account the dependence of ϵ_ν on neutron number over the Xe isotopic sequence. It is natural to assume that this variation follows the valence-proton-free 2^+_1 energies in the nearby magic Sn isotopes. The local evolution of the 2^+_1 state in the Sn chain for the same neutron numbers is parabolic (diamonds in Fig. 7.22). Therefore, the unperturbed neutron energy (ϵ_ν) has been parametrized as ϵ_ν=a+b(N_ν-1)+c(N_ν-1)^2. The value of the parameter a is: a=$\epsilon_\nu(N_\nu=1)$=$E_{2^+_1}(^{130}\mathrm{Sn})$=1221 keV. From the two-state mixing scheme, the resulting energies of the one-phonon 2^+ states ($2^+_{1,\mathrm{ms}}$, 2^+_1) can be expressed as:

$$E(2^+_{1,\mathrm{ms}}, 2^+_1) = \frac{\epsilon_\pi + \epsilon_\nu}{2} \pm \sqrt{\frac{(\epsilon_\pi - \epsilon_\nu)^2}{4} + \beta^2 N_\pi N_\nu}, \tag{7.12}$$

where + [-] corresponds to E($2^+_{1,\mathrm{ms}}$) [E(2^+_1)], respectively. The values of the parameters b, c and β were derived simultaneously from a least-squares fit to the experimentally observed evolution of the energy of the one-phonon fully symmetric (the 2^+_1) state and of the identified one-phonon MSS in the Xe isotopic chain (see Fig. 7.22). The fit yields the values β=0.319(1) MeV, b=0.028(4) MeV, c=0.008(2) MeV.

In Ref. [90], a similar fit has been carried out for the $N = 80$ isotones including the ^{134}Xe nucleus. The resulting proton-neutron interaction parameter was β=0.35(1) MeV. Since ^{134}Xe belongs to both chains ($N = 80$ and $Z = 54$), we expect the same proton-neutron interaction parameter β in both fits if the two-state mixing scheme holds true along these nuclear chains. Indeed, the values from our data, $\beta = 0.319(1)$, and from the $N = 80$ isotonic chain, $\beta = 0.35(1)$ [90], coincide within 15%. The fact that they are not equal in size may result either from the oversimplification of the problem in the simple two-state mixing scheme or from unsufficient sensitivity of our experiment to high-lying fragments of the $2^+_{1,\mathrm{ms}}$ excitation, located at energies above ~ 2.2 MeV. We plot the E($2^+_{1,\mathrm{ms}}$) values from Eq.(7.12) by using the parameters proposed in [90] which corresponds to the dashed curve in Fig. 7.22. The difference between the two fitted curves for the E($2^+_{1,\mathrm{ms}}$) (dashed black and solid blue curves on Fig. 7.22) may suggest, that in lighter Xe isotopes, we have observed and included in our fit only the lowest fragment of the total $M1$ strength. There may be other missing fragments lying at higher energies (> ~2.2 MeV). This suggestion is supported by the larger β value found in Ref.

[143] (β=0.388 MeV), where they fitted only the energies of the 2_1^+ states in Xe. This larger β value, found by Heyde and Sau, supports the suggestion that the center of gravity of the total $2_{1,\mathrm{ms}}^+ \rightarrow 2_1^+$ $M1$ strength would lies higher than the detected $2_{1,\mathrm{ms}}^+ \rightarrow 2_1^+$ $M1$ strength seen in our experiments. This statement is reinforced by the upper limit of the $B(M1)$ value found in ^{128}Xe for the 2275.6 keV γ-transition from the 2^+ state at 2718.5 keV to the 2_1^+ state at 442.9 keV [$B(M1; 2^+ \rightarrow 2_1^+) \leq 0.19(5)\ \mu_N^2$]. The measurement of the mixing ratio of this mixed transition could give us the corresponding absolute $B(M1; 2^+ \rightarrow 2_1^+)$ value. This, of course, could resolve our janus problem: fragmentation or disappearance of the $M1$ strength with increasing collectivity.

In summary, low lying excited states of ^{130,132}Xe have been investigated with projectile Coulomb excitation. The $2_{1,\mathrm{ms}}^+$ levels have been identified. This allowed us to trace its evolution along the Xe isotopic chain from close to the $N = 82$ neutron shell closure out towards midshell. We observe the energy of the $2_{1,\mathrm{ms}}^+$ state increases and the $2_{1,\mathrm{ms}}^+ \rightarrow 2_1^+$ $M1$ strength decreases as the number of valence neutron hole pairs (N_ν) increases. The decrease and disappearance of the $M1$ strength can be explained by two different mechanisms: either the $2_{1,\mathrm{ms}}^+$ state fragments on the path from vibrators to γ-unstable rotors or the $2_{1,\mathrm{ms}}^+$ state loses slowly its isovector character and finally completely disappears towards mid-shell. It remains to be determined by future measurements searching for higher-lying $M1$ transitions in these Xe isotopes which of the two mechanisms is responsible for our observations. We have discussed the former case by using a two-state mixing scheme, which suggests fragments of the $2_{1,\mathrm{ms}}^+$ state may exist at energies higher than 2.2 MeV in ^{124,126,128,130,132}Xe. This fragmentation is also supported by the upper limit of the 2^+ state at 2718.5 keV in ^{128}Xe [$B(M1; 2^+ \rightarrow 2_1^+) \leq 0.19(5)\ \mu_N^2$]. Thus we also call for the measurement of the multipole mixing ratio of the 2275.6 keV γ-transition in the nucleus ^{128}Xe.

8 Summary and outlook

Low lying excited states of ^{124,126,128,130,132,134}Xe have been investigated by using the Coulomb excitation method in inverse kinematics at Argonne National Laboratory.

The new data on ^{124,126}Xe allow the symmetry breaking to be investigated by relating the fluctuations in the quantum numbers directly to the experimental observables. Using this approach, we have quantitatively shown that, in ^{124,126}Xe, the O(6) symmetry is completely dissolved while the O(5) symmetry is only slightly perturbed. It is therefore important the issue be investigated further which requires more $E2$ transition rates for high-lying off-yrast states of nuclei that are currently being viewed as close to the O(6) symmetry be measured and analysed with the method we have proposed here. Clearly, the so far best occurence of the O(6) symmetry in nature, ^{196}Pt, becomes a very interesting case.

We have also shown that ^{128}Xe is not a close realization of E(5) symmetry, leaving ^{130}Xe as the most likely candidate amongst the xenon isotopes. Our analysis on ^{128}Xe highlights the importance of the relative energies of the first *two* excited 0^+ states and their $E2$ decay rates as a robust test of E(5) symmetry. Unfortunately these states have not been observed in our experiment on ^{130}Xe. Similar tests on ^{130}Xe and ^{134}Ba would conclusively demonstrate how well E(5) is realized in these “best cases”. Another way to explore the nature of these two keys 0^+ states would be the measurement through electron scattering of their $B(E0)$ strengths from the ground state.

The evolution of the $2^+_{1,\mathrm{ms}}$ state within the Xe stable even-even isotopic chain has been studied. We observe that the $2^+_{1,\mathrm{ms}} \to 2^+_1$ $M1$ strength decreases as the number of valence neutron pairs increases and the $2^+_{1,\mathrm{ms}}$ state increases in energy as one goes to larger values of N_ν. This observation can be explained by two different mechanisms: either the $2^+_{1,\mathrm{ms}}$ state fragments on the path from vibrators to γ-unstable rotors or the $2^+_{1,\mathrm{ms}}$ state loses slowly its isovector character and finally completely disappears towards mid-shell. Our analysis could not decide this issue finally. We discussed the former case by using a two-state level scheme, which may suggest fragments of the $2^+_{1,\mathrm{ms}}$ state lying at energies higher than 2.2 MeV in ^{124,126,128,130,132}Xe. The upper limit of the 2^+ state at 2718.5 keV in ^{128}Xe [$B(M1; 2^+ \to 2^+_1) \leq 0.19(5)$ μ_N^2] supports this statement. Clearly the multipole mixing ratio of the 2275.6 keV γ-transition from the 2^+ state at 2718.5 keV to the 2^+_1 state at 442.9 keV becomes an appealing object which could resolve our dilemna. This could be done by using the fusion evaporation reaction followed by β^+-decay in ^{125}Te($^7_3$Li,4n)^{128}Cs [$J^\pi_{GS}(^{128}Cs) = 1^+$]. Another way to investigate this issue is the use of the Projectile Coulomb excitation method with heavier targets therefore favoring multistep COULEX and thus populating higher-lying 2^+ states. The inverse kinematics induced by the use of heavier targets implies the need of a particle detection device to assure a good and necessary Doppler correction. The feasibility of a multistep COULEX combined with our data analysis has not been proven yet but our group has been working on it since the last two years.

Finally, the fundamental $2^+_{1,\mathrm{ms}}$ state (or at least a fragment) is known in all even-even stable nuclei in the ($Z > 50$, $N < 82$) region of the nuclide chart except in three nuclei: ^{132,130}Ba and ^{138}La. It would be interesting to investigate the two nuclei ^{132,130}Ba with the same method in order to, first complete the region and second establish the evolution of the $2^+_{1,\mathrm{ms}}$ state in the stable even-even Ba isotopic chain to compare it with our observations in Xe. Thus, one could see the influence of the proton degree of freedom on the evolution of the $2^+_{1,\mathrm{ms}}$ state. This would also offer us the possibility to study new isotonic chains ($N = 78$, $N = 76$, $N = 74$).

Up to now, no MSS have been discovered in radioactive nuclei. The same Coulomb excitation method can be performed using radioactive beams. With the plans of high intensity radioactive beam facilities such as FAIR (Darmstadt, Germany), SPIRAL2 (Caen, France), RIA (USA), RIBF (Wako, Japan) to be available available in the near future, such experiments may soon be feasible, thus extending the exploration regions of the $2^+_{1,\mathrm{ms}}$ state and finally improve our understanding of the valence proton-neutron interaction.

A CLX input file: ^{130}Xe as an example

Below is given an example of an input file for CLX. The reader is referred to the README file of the clx package for more details. The input file can be executed with the commando line: clx < 130Xe.inputfile.clx or for a nicer output by: clx < 130Xe.inputfile.clx | clx_mk_table.awk.

```
130Xe -> 12C @409 MeV  ! Title
11101111               ! Output control print parameters (see README file of CLX code)
12        0.      12.  ! Max states involved-0(nothing)- Max value of magnetic number.
0.        0.      0.   ! Accuracy parameters (see README file of CLX code)
6      130             ! Ztarget Aprojectile
54      12             ! Zprojectile  Atarget
369.                   ! (Average) Energy beam (in LAB system)
0.  180.  10           ! Starting angle (°), stopping angle (°), step angle (°) (in CM system)
1   0  0.000    1 0    ! Levels labels-Spin-Energy(MeV)-Parity-K
2   2  0.536    1 0
3   2  1.1221   1 0
4   4  1.2046   1 0
5   0  1.590    1 0
6   3  1.632    1 0
7   4  1.808    1 0
8   6  1.9441   1 0
9   2  2.0171   1 0
10   4  2.081   1 0
11   2  2.1502  1 0
12   3  2.278  -1 0

1   2  0.806    2   ! Initial state-Final state-Matrix element in eb (for E2)-Multipolarity
1   3  0.0745   2   ! E2 transition
1   4  0.0      4   ! E4 transition
1   7  0.0      4
1   9  -0.046   2
1   10 0.       4
1   11 -0.070   2
1   12 0.15     3   ! E3 transition

2   2   0       2   ! Quadrupole moment
2   3   -0.931  2
2   3   0.001  -1   ! M1 transition. In our case negligible
2   4   1.278   2
2   5   0.118   2
2   6   -0.181  2
2   7   -0.161  2
2   9   -0.13   2
2   10  0.248   2
2   11  -0.106  2
2   12   0.34   1   ! E1 transition

3   3   0       2
3   4   0.07    2
3   5   -1.     2
3   6   2.487   2
3   7   -0.904  2
3   9   0.0     2
3   10  0.0     2
3   11  0.215   2
3   12  0.44    1

4   4   0       2
4   6   -1.2    2
4   7   0.95    2
4   8   1.87    2
4   9   0.0     2
4   10  -2.95   2
4   12  0.0     1

6   6   0   2
7   7   0   2
8   8   0   2
9   9   0   2
10 10   0   2
11 11   0   2
12 12   0   2
```

B Error propagation

Consider the general function f(x,a,b,c,d,e,f,g) depending on the correlated parameters (a,b,c,d,e,f,g). The variance will be noted σ_a for the variable a, which is equal to the absolute error Δa.
The covariance, between the parameters a and b, will be noted $\sigma_{ab} = \sigma_a \cdot \sigma_b \cdot \rho_{ab}$ where ρ_{ab} is the correlation coefficient between the variables a and b (Note that $\rho_{aa} = 1$).

$$\Delta f^2 = \sigma_f^2 = \sum_{i=a}^{g} (\frac{\partial f}{\partial i})^2 \cdot \sigma_i^2 + 2 \sum_{i=a}^{g} \sum_{j>i}^{g} (\frac{\partial f}{\partial i}) \cdot (\frac{\partial f}{\partial j}) \cdot \sigma_{ij} \tag{B.1}$$

$$\Delta f^2 = \sum_{i=a}^{g} (\frac{\partial f}{\partial i})^2 \cdot \Delta_i^2 + 2 \sum_{i=a}^{g} \sum_{j>i}^{g} (\frac{\partial f}{\partial i}) \cdot (\frac{\partial f}{\partial j}) \cdot \Delta_i \cdot \Delta_j \cdot \rho_{ij} \tag{B.2}$$

In the particular case where the variables are not correlated, $\sigma_{ij} = 0$ for $i \neq j$ and:

$$\Delta f^2 = \sigma_f^2 = \sum_{i=a}^{g} (\frac{\partial f}{\partial i})^2 \cdot \sigma_i^2 \tag{B.3}$$

$$\Delta f^2 = \sum_{i=a}^{g} (\frac{\partial f}{\partial i})^2 \cdot \Delta_i^2 \tag{B.4}$$

These formulas have been taken from [86].

C Angles Germanium Detectors of Gammasphere

Ring	θ	ϕ				
1	17.27465	1	3	2	4	6
		72.00	144.00	216.00	288.00	360.00
2	31.71747	5	7	9	8	10
		36.00	108.00	180.00	252.00	324.00
3	37.37737	11	13	12	14	16
		72.00	144.00	216.00	288.00	360.00
4	50.06504	15	17	19	21	23
		22.84	49.16	94.84	121.16	166.84
		18	20	22	24	26
		193.16	238.84	265.16	310.84	337.16
5	58.28253	25	27	28	30	32
		72.00	144.00	216.00	288.00	360.00
6	69.82033	29	31	33	35	37
		18.49	53.51	90.49	125.51	162.49
		34	36	38	40	42
		197.51	234.49	269.51	306.49	341.51
7	79.18768	39	41	44	46	48
		72.00	144.00	216.00	288.00	360.00
8	80.70960	43	45	47	50	52
		36.00	108.00	180.00	252.00	324.00
9	90.00000	49	51	53	55	57
		18.00	54.00	90.00	126.00	162.00
		54	56	58	60	62
		198.00	234.00	270.00	306.00	342.00
10	99.29040	59	61	64	66	68
		72.00	144.00	216.00	288.00	360.00
11	100.81232	63	65	67	70	72
		36.00	108.00	180.00	252.00	324.00
12	110.17967	69	71	73	75	77
		17.51	54.49	89.51	126.49	161.51
		74	76	78	80	82
		198.49	233.51	270.49	305.51	342.49
13	121.71747	79	81	83	84	86
		36.00	108.00	180.00	252.00	324.00
14	129.93496	85	87	89	91	93
		13.16	58.84	85.16	130.84	157.16
		88	90	92	94	96
		202.84	229.16	274.84	301.16	346.84
15	142.62263	95	97	99	98	100
		36.00	108.00	180.00	252.00	324.00
16	148.28253	101	103	102	104	106
		72.00	144.00	216.00	288.00	360.00
17	162.72535	105	107	109	108	110
		36.00	108.00	180.00	252.00	324.00

Table C.1: Position (θ,ϕ) of the 110 Germanium detectors of the Gammasphere array arranged in 17 rings.

Bibliography

[1] R. F. Casten, Nucl. Phys. **A443**, 1 (1985).

[2] F. Iachello, Phys. Rev. Lett. **53**, 1247 (1984).

[3] N. Pietralla, C. Fransen, D. Belic, P. von Brentano, C. Friessner, U. Kneissl, A. Linnemann, A. Nord, H. H. Pitz, T. Otsuka, I. Schneider, V. Werner, I. Wiedenhöver, Phys. Rev. Lett. **83**, 1303 (1999).

[4] N. Pietralla, C. Fransen, P. von Brentano, A. Dewald, A. Fitzler, C. Friessner, J. Gableske, Phys. Rev. Lett. **84**, 3775 (2000).

[5] N. Pietralla, C. J. Barton III, R. Krücken, C. W. Beausang, M. A. Caprio, R. F. Casten, J. R. Cooper, A. A. Hecht, H. Newman, J. R. Novak, N. V. Zamfir, Phys. Rev. C **64**, 031301(R) (2001).

[6] N. Pietralla and K. Starosta, Nucl. Phys. News **Vol.** 13 No. 2, 15 (2003).

[7] N. Pietralla, C. Fransen, A. Gade, N. A. Smirnova, P. von Brentano, V. Werner, S. W. Yates, Phys. Rev. C **68**, 031305(R) (2003).

[8] G. Rainovski, N. Pietralla, T. Ahn, C. J. Lister, R. V. F. Janssens, M. P. Carpenter, S. Zhu, C. J. Barton III, Phys. Rev. Lett. **96**, 122501 (2006).

[9] N. Pietralla, P. von Brentano, A. F. Lisetskiy, Prog. Part. Nucl. Phys. **60**, 225 (2008). and references therein.

[10] A. Richter, Prog. Part. Nucl. Phys. **34**, 261 (1995).

[11] U. Kneissl, H. H. Pitz, A. Zilges, Prog. Part. Nucl. Phys. **37**, 349 (1996).

[12] D. Zawischa, J. Phys. G: Nucl. Part. Phys. **24**, 683 (1998).

[13] A. Arima, F. Iachello, Ann. Phys. **99**, 253 (1976).

[14] A. Arima, F. Iachello, Ann. Phys. **111**, 201 (1978).

[15] A. Arima, F. Iachello, Phys. Rev. Lett. **35**, 1069 (1975).

[16] A. Faessler, W. Greiner, and R. K. Sheline, Nucl. Phys. **417** (1965).

[17] A. S. Davydov and G. F. Filipov, Nucl. Phys. **8**, 237 (1958).

[18] A. S. Davydov and A. A. Chaban, Nucl. Phys. **20**, 499 (1960).

[19] S. G. Rohozinski, J. Dobaczewski, B. Nerlo-Pomorska, K. Pomorski, J. Srebrny, Nucl. Phys. **A292**, 66 (1977).

[20] G. Puddu, O. Scholten, T. Otsuka, Nucl. Phys. **A348**, 109 (1980).

[21] R. F. Casten, P. von Brentano, Phys. Lett. **152B**, 22 (1985).

[22] D. L. Hill and J. A. Wheeler, Phys. Rev. **89**, 1102, 1953.

[23] A. Bohr and B. Mottelson, *Nuclear Structure* **I**, (Benjamin, Reading, 1969).

[24] A. Bohr and B. Mottelson, *Nuclear Structure* **II**, (Benjamin, Reading, 1975).

[25] J. P. Elliot, Proc. Roy. Soc. **A 245**, 128 (1958).

[26] H. Feshbach and F. Iachello, Phys. Lett. **B45**, 7 (1973).

[27] H. Feshbach and F. Iachello, Ann. Phys. (NY) **84**, 211 (1974).

[28] D. Janssen, R. V. Jolos and F. Dönau, Nucl. Phys. **A224**, 93 (1974).

[29] F. Iachello and A. Arima, *The Interacting Boson Model* (Cambridge University Press, Cambridge, 1987).

[30] D. Bonatsos, *Interacting Boson Models of Nuclear Structure,* (Clarendon Press, Oxford, 1988).

[31] J. Wilets and M. Jean, Phys. Rev. **102**, 788 (1956).

[32] D. D. Warner and R. F. Casten, Phys. Rev. Lett. **48**, 1385 (1982).

[33] P. O. Lipas, P. Toivonen, and D. D. Warner, Phys. Lett. **B155**, 295 (1985).

[34] V. Werner, N. Pietralla, P. von Brentano, R. F. Casten, and R. V. Jolos, Phys. Rev. C **61**, 021301(R) (2000).

[35] V. Werner, Dissertation, Universität zu Köln, (2004).

[36] A. Arima, T. Otsuka, F. Iachello, and I. Talmi, Phys. Lett. B **66**, 205 (1977).

[37] T. Otsuka, A. Arima, F. Iachello, and I. Talmi, Phys. Lett. B **76**, 139 (1978).

[38] P. Van Isacker, K. Heyde, J. Jolie, and A. Sevrin, Ann. Phys. (NY) **171**, 253 (1986).

[39] T. Otsuka, K. H. Kim, Phys. Rev. C **50**, R1768 (1994).

[40] G. Siems, U. Neumeyer, I. Wiedenhöver, S. Albers, M. Eschenauer, R. Wirowski, A. Geldberg, P. von Brentano, T. Otsuka, Phys. Rev. Lett. **B320**, 1 (1994).

[41] N. Pietralla, P. von Brentano, R. F. Casten, T. Otsuka, and N. V. Zamfir, Phys. Rev. Lett. **73**, 2962 (1994).

[42] I. Wiedenhöver, A. Gelberg, T. Otsuka, N. Pietralla, J. Gableske, A. Dewald, P. von Brentano, Phys. Rev. C **56**, R2354 (1997).

[43] N. Yoshida, A. Gelberg, T. Otsuka, I. Wiedenhöver, H. Sagawa, P. von Brentano, Nucl. Phys. **A619**, 65 (1997).

[44] N. Pietralla, P. von Brentano, A. Gelberg, T. Otsuka, A. Richter, N. Smirnova, I. Wiedenhöver, Phys. Rev. C **58**, 191 (1998).

[45] D. Bohle, A. Richter, W. Steffen, A. E. L. Dieperink, N. Lo Iudice, F. Palumbo, and O. Scholten, Phys. Rev. Lett. **B137**, 27 (1984).

[46] W. D. Hamilton, A. Irbäck, J. P. Elliot, Phys. Rev. Lett. **53**, 2469 (1984).

[47] P. Park, A. R. H. Subber, W. D. Hamilton, J. P. Elliot, K. Kumar, J. Phys. G: Nucl. Phys. **11**, L251 (1985).

[48] G. Molnar, R. A. Gatenby, S. W. Yates, Phys. Rev. C **37**, 898 (1988).

[49] S. T. Ahmad, W. D. Hamilton, P. Van Isacker, S. A. Hamada, S. J. Robinson, J. Phys. G **15**, 93 (1989).

[50] A. Giannatiempo, A. Nanini, A. Perego, P. Sona, G. Maino, Phys. Rev. C **44**, 1508 (1991).

[51] A. Giannatiempo, A. Nanini, A. Perego, P. Sona, D. Cutoiu, Phys. Rev. C **53**, 2770 (1996).

[52] A. Arima and F. Iachello, Ann. Phys. (N.Y.) **111**, 201 (1976).

[53] A. Arima and F. Iachello, Phys. Rev. Lett. **40**, 385 (1978).

[54] A. Bohr, Mat. Fys. Medd. K. Dan. Vidensk Selsk. **26**, No. 14 (1952).

[55] F. Iachello, Phys. Rev. Lett. **87**, 052502 (2001).

[56] R. Krücken, B. Albanna, C. Bialik, R. F. Casten, J. R. Cooper, A. Dewald, N. V. Zamfir, C. J. Barton, C. W. Beausang, M. A. Caprio, A. A. Hecht, T. Klug, J. R. Novak, N. Pietralla, P. von Brentano, Phys. Rev. Lett. **88** 23250 (2002).

[57] R. F. Casten and N. V. Zamfir, Phys. Rev. Lett. **87** 052503 (2001).

[58] D. Tonev, A. Dewald, T. Klug, P. Petkov, J. Jolie, A. Fitzler, O. Möller, S. Heinze, P. von Brentano, R. F. Casten, Phys. Rev. C **69** 034334 (2004).

[59] A. Dewald, O. Möller, B. Saha, K. Jessen, A. Fitzler, B. Melon, T. Pissulla, S. Heinze, J. Jolie, K. O. Zell, P. von Brentano, P. Petkov, S. Harissopulos, G. De Angelis, T. Martinez, D. R. Napoli, N. Marginean, M. Axiotis, C. Rusu, D. Tonev, A. Gadea, Y. H. Zhang, D. Bazzacco, S. Lunardi, C. A. Ur, R. Menegazzo, E. Farnea, J. Phys. G: Nucl. Part. Phys. **31**, 1427 (2005).

[60] N. Pietralla and O. M. Gorbachenko, Phys. Rev. C **70**, 011304(R) (2004).

[61] K. Dusling and N. Pietralla, Phys. Rev. C **72**, 011303(R) (2005).

[62] K. Dusling, N. Pietralla, G. Rainovski, T. Ahn, B. Bochev, A. Costin, T. Koike, T. C. Li, A. Linnemann, S. Pontillo, and C. Waman, Phys. Rev. C **73**, 014317 (2006).

[63] A. Costin, M. Reese, H. Ai, R. F. Casten, K. Dusling, C. R. Fitzpatrick, G. Gürdal, A. Heinz, E. A. McCutchan, D. A. Meyer, O. Möller, P. Petkov, N. Pietralla, J. Qian, G. Rainovski, and V. Werner, Phys. Rev. C **79**, 024307 (2009).

[64] F. Iachello, Phys. Rev. Lett. **85**, 3580 (2000).

[65] D. Bonatsos, D. Lenis, N. Pietralla, P. A. Terziev, Phys. Rev. C **74**, 044306 (2006).

[66] E. Chacón and M. Moshinsky, J. Math. Phys. **18**, 870 (1977).

[67] K. Alder, A. Bohr, T. Huus, B. R. Mottelson, A. Winther, Rev. Modern Phys. **28**, 432 (1956).

[68] K. Alder, A. Winther, *Coulomb Excitation*, (Academic Press, New York, 1966).

[69] K. Alder, A. Winther, Electromagnetic Excitation, *Theory of Coulomb excitation with Heavy Ions*, (North Holland, Amsterdam, 1975).

[70] D. Cline, Ann. Rev. Nucl. Part. Sci. **36**, 683 (1986).

[71] D. Cline, Bull. Am. Phys. Soc **14**, 726 (1969).

[72] H. Ower, Phd thesis, Johan-Wolfgang-Goethe-Universität zu Frankfurt am Main (1980).

[73] A. Lell, Master's thesis, Universität München (1978).

[74] H. Ower, J. Gerl, H. Scheit, computer code clx.

[75] T. Czosnyka, D. Cline, and C. Y. Wu, *Coulomb Excitation Data Analysis Code; Gosia*, Dept. of Physics and Astronomy, University of Rochester, (2007).

[76] K. Alder, A. Bohr, T. Huus, B. R. Mottelson, A. Winther, Rev. Modern Phys. **30**, 353 (1958).

[77] A. Winther and J. de Boer. A computer program for multiple Coulomb excitation. In K. Alder and A. Winther, *Coulomb Excitation*, (Academic Press, New York, 1966).

[78] http://www.phy.anl.gov/atlas/facility/floorplan.html.

[79] I. Lee, Nucl. Phys. **A520**, 641 (1990).

[80] P. Nolan, F. Beck, and D. Fossan, Annu. Rev. Nucl. Part. Sci. **45**, 561 (1994).

[81] I. Lee, Prog. Part. Nucl. Phys., Vol. **38**, 65 (1997).

[82] Agata collaboration, Agata, Technical Design Report, (2008).

[83] M. A. Riley, Gammasphere, the beginning...1993-1997. Dept of Physics, Florida State University, URL http://nucalf.physics.fsu.edu/ riley/gamma.

[84] R. D. Evans, *The Atomic Nucleus*, (McGRAW-HILL, New York, 1955).

[85] K. S. Krane, *Introductory Nuclear Physics*, (John Wiley and Sons, 1988).

[86] E. Weisstein, *Error Propagation*, http://mathworld.wolfram.com/ErrorPropagation.html.

[87] R. F. Casten, *Nuclear Structure from a simple perspective* (Oxford University Press, Oxford, 1990).

[88] W. F. Mueller, J. A. Church, T. Glasmacher, D. Gutknecht, G. Hackman, P. G. Hansen, Z. Hu, K. L. Miller, and P. Quirin, Nucl. Instrum. Methods **A466**, 492 (2001).

[89] G. Rainosvki, N. Pietralla, T. Ahn, L. Coquard, C. J. Lister, R. V. F. Janssens, M. P. Carpenter, S. Zhu, L. Bettermann, J. Jolie, W. Rother, R. V. Jolos, V. Werner, Phys. Lett. **B683**, 11 (2010).

[90] T. Ahn, L. Coquard, N. Pietralla, G. Rainovski, A. Costin, R. V. F.Janssens, C. J. Lister, M. Carpenter, S. Zhu, K. Heyde, Phys. Lett. **B679**, 19 (2009)

[91] http://npg.dl.ac.uk/MIDAS/download/midassort/midassort.html.

[92] http://ns.ph.liv.ac.uk/MTsort-manual/MTsort.html.

[93] D. Pelte, D. Schwalm, *Heavy Ion Collisions*, Vol. **3**, (North-Holland, Amsterdam, 1982).

[94] S. Raman, C. W. Nestor, and P. Tikkanen, Atomic Data and Nuclear Data Tables **78**, Number 1, (2001).

[95] C. Y. Wu, D. Cline, T. Czosnyka, A. Backlin, C. Baktash, R. M. Diamond, G. D. Dracoulis, L. Hasselgren, H. Kluge, B. Kotlinski, J. R. Leigh, J. O. Newton, W. R. Phillips, S. H. Sie, J. Srebrny, F. S. Stephens, Nucl. Phys. **A607**, 178 (1996).

[96] T. Yamazaki, Nuclear Data **3**, 1 (1967).

[97] A. Messiah, *Quantum Mechanics* **II**, (North Holland Publishing, New York 1981).

[98] K. S. Krane and R. M. Steffen, Phys. Rev. C **2**, 724 (1970).

[99] K. S. Krane, R. M. Steffen, and R. M. Wheeler, Nucl. Data. Tables **11**, 351 (1973).

[100] W. P. Alford, R. E. Anderson, P. A. Batay-Csorba, R. A. Emigh, D. A. Lind, P. A. Smith, C. D. Zafiratos, Nucl. Phys. **A323**, 339 (1979).

[101] W. B. Walters, J. Rikovska, N. J. Stone, T. L. Shaw, P. Walker, I. S. Grant, Hyper. Inter. **43**, 343 (1988).

[102] V. Werner, H. Meise, I. Wiedenhöver, A. Gade, P. von Brentano, Nucl. Phys. **A692**, 451 (2001).

[103] B. Saha, A. Dewald, O. Möller, R. Peusquens, K. Jessen, A. Fitzler, T. Klug, D. Tonev, P. von Brentano, J. Jolie, B. J. P. Gall, P. Petkov, Phys. Rev. C **70**, 034213 (2004).

[104] K. F. W. Gast, Thesis Shape-Koexistenz in Leichten Xe-Isotopen, Universität zu Köln (1982).

[105] W. F. Mueller, M. P. Carpenter, J. A. Church, D. C. Dinca, A. Gade, T. Glasmacher, D. T. Henderson, Z. Hu, R. V. F. Janssens, A. F. Lisetskiy, C. J. Lister, E. F. Moore, T. O. Pennington, B. C. Perry, I. Wiedenhöver, K. L. Yurkewicz, V. G. Zelevinsky, H. Zwahlen, Phys. Rev. C **73**, 014316 (2006).

[106] W. Lieberz, A. Dewald, W. Frank, A. Gelberg, W. Krips, D. Lieberz, R. Wirowski, P. von Brentano, Phys. Lett. **B240**, 38 (1990).

[107] F. Seiffert, W. Lieberz, A. Dewald, S. Freund, A. Gelberg, A. Granderath, D. Lieberz, R. Wirowski, P. von Brentano, Nucl. Phys. **A554**, 287 (1993).

[108] A. Gade, I.Wiedenhöver, J. Gableske, A. Gelberg, H. Meise, N. Pietralla, P.von Brentano, Nucl. Phys. **A665**, 268 (2000).

[109] J. Katakura and K. Kitao, Nuclear Data Sheets **97**, 765 (2002).

[110] R. F. Casten and D. D. Warner, Rev. Mod. Phys. **60**, 389 (1988) and the references therein.

[111] D. D. Warner and R. F. Casten, Phys. Rev. Lett. **48**, 1385 (1982); Phys. Rev. C **28**, 1798 (1983) .

[112] P. Van Isacker, Nucl. Phys. **A465**, 497 (1987).

[113] J. A. Cizewski, R. F. Casten, G. J. Smith, M. L. Stelts, W. R. Kane, H. G. Börner, W. F. Davidson, Phys. Rev. Lett. **40**, 168 (1978).

[114] H. G. Börner, J. Jolie, S. Robinson, R. F. Casten, J. A. Cizewski, Phys.Rev. C **42**, R2271 (1990).

[115] U. Neuneyer, A. Mertens, R. Kuhn, I. Wiedenhöver, O. Vogel, M. Wilhelm, M. Luig, K. O. Zell, A. Gelberg, P. von Brentano, T. Otsuka, Nucl. Phys. **A607**, 299 (1996).

[116] X. W. Pan, T. Otsuka, J. Q. Chen, A. Arima, Phys. Lett. **B287**, 1 (1992).

[117] O. Scholten, Computer codes PHINT and FBEM, KVI internal report No. **63**, (1979).

[118] N. Pietralla, Dissertation, Universität zu Köln, (1996).

[119] J. Srebny, T. Czosnyka, W. Karczmarczyk, P. Napiorkowski, Ch. Droste, H-J. Wollersheim, H. Emling, H. Grein, R. Kulessa, D. Cline, C. Fahlander, Nucl. Phys. **A557**, 663c (1993).

[120] A. Leviatan, A. Novoselsky, I. Talmi, Phys. Lett. **B172**, 144 (1986).

[121] P. von Brentano, A. Gelberg, S. Harissopulos, R. F. Casten, Phys. Rev. C **38**, 2386 (1988).

[122] F. Iachello, Phys. Rev. Lett. **91**, 132502 (2003).

[123] R. F. Casten and N. V. Zamfir, Phys. Rev. Lett. **85**, 3584 (2000).

[124] R. M. Clark, M. Cromaz, M. A. Deleplanque, M. Descovich, R. M. Diamond, P. Fallon, I. Y. Lee, A. O. Macchiavelli, H. Mahmud, E. Rodriguez-Vieitez, F. S. Stephens, D. Ward, Phys. Rev. C **69**, 064322 (2004).

[125] J. M. Arias, C. E. Alonso, A. Vitturi, J. E. Garcia-Ramos, J. Dukelsky, A. Frank, Phys. Rev. C **68**, 041302(R) (2003).

[126] E. W. Schneider, M. D. Glascock, W. B. Walters, R. A. Meyer, Phys. Rev. C **19**, 1025 (1979).

[127] L. Goettig, Ch. Droste, A. Dygo, T. Morek, J. Srebrny, R. Broda, J. Styczen, J. Hattula, H. Helppi, M. Jaaskelainen, Nucl. Phys. **A357**, 109 (1981).

[128] M. Kanbe, K. Kitao, Nuclear Data Sheets **94**, 227 (2001).

[129] private communication W. Rother.

[130] R. Reinhardt, Phd Thesis, University of Cologne, (1986).

[131] P. F. Mantica Jr., B. E. Zimmerman, W. B. Walters, J. Rikovska, N. J. Stone, Phys. Rev. C **45**, 1586 (1992).

[132] D. R. Bès, Nucl. Phys. **10**, 373 (1959).

[133] A. Richter, Nucl. Phys. **A522**, 139c (1991).

[134] N. Lo Iudice and F. Palumbo, Phys. Rev. Lett. **41**, 1532 (1978).

[135] L. Coquard, N. Pietralla, T. Ahn, G. Rainovski, L. Bettermann, M. P. Carpenter, R. V. F. Janssens, J. Leske, C. J. Lister, O. Möller, W. Rother, V. Werner, S. Zhu, Phys. Rev. C **80**, 061304(R) (2009).

[136] Balraj Singh, Nuclear Data Sheets **93**, 33 (2001).

[137] Y. Khazov, A. A. Rodionov and S. Sakharov, Balraj Singh, Nuclear Data Sheets **104**, 497 (2005).

[138] P. G. Hopke, A. G. Jones, W. B. Walters, A. Prindle, and R. A. Meyer, Phys. Rev. C **8**, 745 (1973).

[139] W. Gelletly, W. R. Kane, and D. R. MacKenzie, Phys. Rev. C **9**, 2363 (1974).

[140] L. Bettermann, C. Fransen, S. Heinze, J. Jolie, A. Linnemann, D. Mücher, W. Rother, T. Ahn, A. Costin, N. Pietralla, Y. Luo, Phys. Rev. C **79**, 034315 (2009).

[141] S. A. Hamada, W. D. Hamilton, and B. Moore, J. Phys. G: Nucl. Phys **14**, 1237 (1988).

[142] H. von Garrel, P. von Brentano, C. Fransen, G. Friessner, N. Hollmann, J. Jolie, F. Käppeler, L. Kaubler, U. Kneissl, C. Kohstall, L. Kostov, A. Linnemann, D. Mücher, N. Pietralla, H. H. Pitz, G. Rusev, M. Scheck, K. D. Schilling, C. Scholl, R. Schwengner, F. Stedile, S. Walter, V. Werner, K. Wisshak, Phys. Rev. C **73**, 054315 (2006).

[143] K. Heyde and J. Sau, Phys.Rev. C **33**, 1050 (1986).

List of publications

Regular publications

- L. Coquard, N. Pietralla, T. Ahn, G. Rainovski, L. Bettermann, M. P. Carpenter, R. V. F. Janssens, J. Leske, C. J. Lister, O. Möller, W. Rother, V. Werner, S. Zhu, *O(6)-symmetry breaking in the γ-soft nucleus ^{126}Xe*, in preparation.

- L. Coquard, N. Pietralla, T. Ahn, G. Rainovski, L. Bettermann, M. P. Carpenter, R. V. F. Janssens, J. Leske, C. J. Lister, O. Möller, W. Rother, V. Werner, S. Zhu, *Mixed-symmetry states in ^{130,132}Xe*, in preparation.

- G. Rainovski, N. Pietralla, T. Ahn, L. Coquard, C. J. Lister, R. V. F. Janssens, M. P. Carpenter, S. Zhu, L. Bettermann, J. Jolie, W. Rother, R. V. Jolos, V. Werner, *How close to the O(6) symmetry is the nucleus ^{124}Xe*, Phys. Lett. B **683**, 11 (2010).

- T. Ahn, L. Coquard, N. Pietralla, G. Rainovski, A. Costin, R. V. F. Janssens, C. J. Lister, M. Carpenter, S. Zhu, K. Heyde,*Evolution of the one-phonon 21, ms mixed-symmetry state in $N = 80$ isotones as a local measure for the proton-neutron quadrupole interaction*, Phys. Lett. B **679**, 19 (2009).

- L. Coquard, N. Pietralla, T. Ahn, G. Rainovski, L. Bettermann, M. P. Carpenter, R. V. F. Janssens, J. Leske, C. J. Lister, O. Möller, W. Rother, V. Werner, S. Zhu, *Robust test of E(5) symmetry in ^{128}Xe*, Phys. Rev. C **80**, 061304 (2009).

- K. Sieja, G. Martinez-Pinedo, L. Coquard, N. Pietralla, *Description of proton-neutron mixed-symmetry states near ^{132}Sn within a realistic large scale shell model*, Phys. Rev. C **80**, 054311 (2009).

Conference proceedings

- N. Pietralla, L. Coquard, G. Rainovski, T. Ahn, C. Bauer, J. Leske, O. Möller, and T. Möller, *Symmetries of Quadrupole-Collective Vibrational Motion in Transitional Even-Even $^{124-134}$Xe Nuclei*, 12th International Conference on Nuclear Reaction Mechanisms, Varenna (Italy), CERN-Proceedings, (2010).

- L. Coquard, N. Pietralla, T. Ahn, M. Carpenter, R. V. F. Janssens, C. J. Lister, J. Leske, O. Möller, T. Möller, G. Rainovski, W. Rother and S. Zhu, *O(6)-symmetry breaking in the ^{126}Xe nucleus*, International Scientific Meeting on Nuclear Physics, La Rábida (Spain), (2009).

- N. Pietralla, T. Ahn, M. Carpenter, L. Coquard, R. V. F. Janssens, K. Heyde, K. Lister, J. Leske, G. Rainovski and S. Zhu, *Isovector Quadrupole Excitations in the Valence Shell of Vibrational Nuclei*, Nuclear Structure and Dynamics 09, AIP Conf. Proc. 1165, 225 (2009).

- L. Coquard, T. Ahn, G. Rainovski, N. Pietralla, J. Leske, O. Möller, T. Möller, M. Carpenter, R. V. F. Janssens, C. J. Lister, S. Zhu, L. Bettermann, W. Rother, *Evolution of the one-phonon mixed-symmetry $2^+_{1,\mathrm{ms}}$ state in even-even Xe isotopes from inverse-kinematics Coulomb excitation*, Proceedings of the 13th International Symposium on Capture Gamma-Ray Spectroscopy and Related Topics, Cologne (Germany), AIP Conf. Proc. 1090, 140 (2009).

- G. Rainovski, N. Pietralla, T. Ahn, L. Coquard, C. J. Lister, R. V. F. Janssens, M. P. Carpenter, S. Zhu, L. Bettermann, W. Rother, J. Jolie, *Off-yrast collectivity of the O(6) like nucleus* ^{124}Xe, Proceedings of the 13th International Symposium on Capture Gamma-Ray Spectroscopy and Related Topics, Cologne (Germany), AIP Conf. Proc. 1090, 263 (2009).

- T. Kröll, T. Behrens, R. Krücken, V. Bildstein, T. Faestermann, R. Gernhäuser, M. Mahgoub, P. Maierbeck, M. Münch, W. Weinzierl, F. Ames, D. Habs, O. Kester, R. Lutter, T. Morgan, M. Pasini, K. Rudolph, P. Thirolf, J. Diriken, M. Huyse, O. Ivanov, P. Mayet, N. Patronis, I. Stefanescu, J. Van de Walle, P. Van Duppen, O. Niedermaier, H. Scheit, D. Schwalm, J. Eberth, F. Finke, D. Martin, P. Reiter, A. Scherillo, M. Seidlitz, N. Warr, D. Weisshaar, J. Iwanicki, P. Butler, J. Cederkäll, E Clément, P. Delahaye, L. M. Fraile, G. Georgiev, U. Köster, T. Sieber, D. Voulot, F. Wenander, S. Franchoo, A. Hurst, A. Ekström, P. E. Kent, K.-H Speidel, J. Leske, S. Schielke, A. Jungclaus, V. Modamio, J. Walker, L. Coquard, M. Pantea, N. Pietralla, T. Davinson, S. Nardelli, *Quadrupole collectivity of neutron-rich nuclei around* ^{132}Sn, 2nd International Conference on Frontiers in Nuclear Structure, Astrophysics, and Reactions - FINUSTAR 2, Kos (Greece), AIP Conf. Proc. 1012, 84 (2008).

Acknowlegments

First, I would like to thank Prof. Dr. Norbert Pietralla to have given me the opportunity to join the experimental nuclear structure group at the Technical University Darmstadt. I would also like to thank him for his continuous support during these three years. Indeed he always took time (even if he did not have) for answering my questions, for giving me explanations and real scientific motivations, for guiding me, for proposing me to participate to international schools and conferences, and of course for helping me to lock off some crossroads along my Phd road.

I want to give a special thank to Dr. Georgi Rainovski who indeed followed and supervised my work since the beginning. Thanks to the collaboration between the TU Darmstadt and the Faculty of Physics of the University of Sofia, I also had the chance to go there and work nearby a real expert of the experimental technique used in this work.

After my arrival in Darmstadt, T. Ahn teached me the long data analysis of this work, from the sorting of the raw datas to the CLX calculations and I am grateful to him for that. He was also very patient by answering all my novice questions.

Thank you to O. Möller and J. Leske for teaching, helping and advising me during the analysis as well as their technical experience during the different experiences performed at Argonne National Laboratory. In this sense I also wish to thank the staff there for their technical support even during late in the night.

Even if I did not write up in this work the results from the COULEX analysis using the code GOSIA, I thank E. Clément and P. J. Napiorkowski to have initiated me to the use of this code, as well as their help and support during my first Gosia runs calculations.

I would also thank all people that participated directly or indirectly to the achievement of this work: M. Reese for his useful tricks in informatics, A. Scheik Obeid and A. Costin for the animated discussions in our office at the beginning of my Phd, C. Bauer for having driven me to the place I wanted to visit in Chicago, T. Möller by helping in the measurement of the mixing ratios and by cross-checking all of my experimental tables, T. Bloch for having gently lent me the unexploited corner of his desk to put some books during the writing of this dissertation...

For the financial support I will thank the German Research Foundation (Deutsche Forschungsgemeinschaft) under grant Nos. Pi 393/2-1 and SFB 634. This work was partially supported by the U.S. Department of Energy, Office of Nuclear Physics, under Contract No. DE-AC02-06CH11357 and by the German-Bulgarian exchange programme under grant Nos. D/08/02055, and by the Helmholtz International Center (HIC) for FAIR.

Finally I am also very grateful to my family for the moral support. The last thank goes to the woman I met here in Darmstadt. Karina, thank you to have tolerated my absence during the last two years. I know it was not always easy to support my mood during these last two years of work but we finally managed!

Lebenslauf

Name:	Laurent Coquard
Geburtsdatum:	06. August 1982
Geburtsort:	Saint-Germain en Laye (Frankreich)
Staatsangehörigkeit:	französisch
Eltern:	Gilles Coquard
	Anita Béatrice Coquard, geb. Cliquet
Familienstand:	ledig

Schulausbildung:

1988-1993	Grundschule Carteret
1993-1997	Katolisches Collège Sainte-Marie Valognes (Gymnasium, Sekundarstufe I)
1997-2000	Lycée Henri Cornat Valognes (Gymnasium, Sekundarstufe II)
Juni 2000	Abitur

Hochschulstudium:

2000-2002	Classes préparatoires (Mathematik, Physik), Lycée Victor Grignard Cherbourg
2002-2006	Ecole Nationale Supérieure de Physique de Grenoble (Ingenieur Elitehochschule)
2004-2006	Doppeldiplom mit der Universität Karlsruhe
2005-2006	Diplom im Fach Physik mit dem Thema: “Messung der stellaren (n,γ)-Querschnitte von ^{54}Fe, ^{9}Be und ^{13}C im keV-Bereich” (Forschungszentrum Karlsruhe)
	Diplom-Ingenieur der Ecole Nationale Supérieure de Physique de Grenoble.
seit März 2007	Promotionsstudium an der Technische Universität Darmstadt
	Wissenschaftlicher Mitarbeiter